Energetics in metallic-island and quantum-dot based single-electron devices

Bivas Dutta

▶ To cite this version:

Bivas Dutta. Energetics in metallic-island and quantum-dot based single-electron devices. Condensed Matter [cond-mat]. Université Grenoble Alpes, 2018. English. NNT : 2018GREAY055 . tel-02024282v2

HAL Id: tel-02024282
https://theses.hal.science/tel-02024282v2

Submitted on 1 Mar 2019

Communauté UNIVERSITÉ Grenoble Alpes

THÈSE

Pour obtenir le grade de

**DOCTEUR DE LA
COMMUNAUTÉ UNIVERSITÉ GRENOBLE ALPES**

Spécialité : NANOPHYSIQUE

Arrêté ministériel : 25 mai 2016

Présentée par

Bivas DUTTA

Thèse dirigée par **Hervé COURTOIS**, UGA
et codirigée par **Jukka PEKOLA**

préparée au sein du **Laboratoire Institut Néel**
dans **l'École Doctorale Physique**

Énergétique dans les dispositifs à un seul électron basés sur des îlots métalliques et des points quantiques

Energetics in Metallic-Island and Quantum-Dot Based Single-Electron Devices

Thèse soutenue publiquement le **19 novembre 2018**,
devant le jury composé de :

OLIVIER BOURGEOIS
DIRECTEUR DE RECHERCHE, CNRS DELEGATION ALPES, Président
Benjamin Huard
PROFESSEUR, ECOLE NORMALE SUPERIEURE DE LYON,
Examinateur
Hartmut Buhmann
PROFESSEUR, UNIVERSITE DE WURTZBOURG - ALLEMAGNE,
Rapporteur
Fabio Taddei
PROFESSEUR, ECOLE NORMALE SUPERIEURE DE PISE ITALIE,
Rapporteur
Hervé Courtois
Professeur, Université Grenoble-Alpes/Institut Néel-CNRS, Directeur de
thèse
Jukka Pekola
Professeur, Aalto University School of Science, Co-directeur de thèse
Clemens Winkelmann
Associate Professor, Grenoble INP/Institut Néel-CNRS, Co-directeur de
thèse

Abstract

At this age of technologically advanced world, the electronic devices are getting more and more densely packed with micro-electronic elements of nano-scale dimension. As a result the heat dissipation produced in these microelectronic-circuits is also increasing immensely, causing a huge amount of energy loss without any use. The *thermoelectric effects* come into play here as one can use this wasted heat to produce some useful work with the help of thermoelectric conversion. In order to achieve such a *heat engine* with a reasonably high efficiency, one needs to understand its thermal behavior at the basic level. Therefore, the study of thermal transport and thermoelectric effect in nano-structures has significant importance both from scientific and application point of view.

In this thesis we present the experimental studies of thermal and thermoelectric transport in different kinds of single-electron devices, where the electronic flow can be controlled at the single electron level.

First, we demonstrate the measurement of gate-controlled heat transport in a Single-Electron Transistor (*SET*), acting as a heat switch between two heat reservoirs. The measurement of temperature of the leads of the *SET* allows us to determine its thermal conductance with the help of a steady state heat-balance among all possible paths of heat flow. The comparison of thermal conductance of the *SET* with its electrical conductance indicates a strong violation of the Wiedemann-Franz (WF) law away from the charge degeneracy.

Second, we extend the study of thermal transport in single-electron devices to the quantum limit, where in addition to the Coulomb interactions the quantum effects are also need to be taken into account, and therefore the individual discrete electronic levels take part in the transport process. We discuss the heat-balance between two heat reservoirs, coupled through a single Quantum-Dot (*QD*) level, and the dissipation of the tunneling electrons on the leads. This produces Coulomb-diamond shapes in the electronic-temperature map of the 'source' lead, as a function of bias and gate voltage.

Third, we present the measurement of thermoelectric transport in a single *QD* junction, starting from the weak coupling regime to the strong coupling-Kondo regime. The experiments introduces a new way of measuring thermovoltage realizing a close to perfect open-circuit condition. The thermopower in a weakly coupled *QD* shows an expected '*e*'

periodic behavior with the gate-induced charge, while it shows a distinct '$2e$' periodic feature in the presence of Kondo spin-correlation. The temperature dependence study of the Kondo-correlated thermopower reveals the fact that the Kondo-resonance is not always pinned to the Fermi level of the leads but it can be slightly off, in agreement with the theoretical predictions.

This study opens the door for accessing a single *QD* junction to operate it as a *QD*-heat engine, where the thermodynamic properties of the device are governed by the laws of *quantum thermodynamics*.

Résumé

Aujourd'hui, nos appareils électroniques sont de plus en plus densément composés de composants nanoélectroniques. En conséquence, la dissipation de chaleur produite dans ces circuits augmente également énormément, provoquant une déperdition d'énergie considérable, en pure perte. Les effets thermoélectriques entrent en jeu ici car ils permettent d'utiliser cette chaleur perdue pour produire un travail utile. Par conséquent, l'étude du transport thermique et de l'effet thermoélectrique dans les nanostructures revêt une importance significative du point de vue scientifique et technologique.

Dans cette thèse, nous présentons nos études expérimentales du transport thermique et thermoélectrique dans différents types de dispositifs à un seul électron, où le flux électronique peut être contrôlé au niveau de l'électron unique.

Tout d'abord, nous montrons la mesure du transport de chaleur contrôlé par la grille dans un transistor à un seul électron (SET), agissant comme un commutateur thermique entre deux réservoirs. Nous déterminons la conductance thermique à l'aide d'un bilan thermique en régime permanent prenant en compte les différents chemins du flux de chaleur. La comparaison de la conductance thermique du SET avec sa conductance électrique indique une forte violation de la loi de Wiedemann-Franz.

Deuxièmement, nous étendons l'étude du transport thermique dans les dispositifs à un seul électron dans le régime de boîte quantique, où, outre les interactions de Coulomb, il faut également prendre en compte les différents niveaux électroniques discrets. Nous discutons du bilan thermique entre deux réservoirs de chaleur couplés par un seul niveau de point quantique, et de la dissipation des électrons tunnel dans les contacts. Cela produit des formes de diamant de Coulomb dans la carte de température électronique de la source, en fonction de la polarisation et de la tension de grille.

Enfin, nous présentons la mesure du transport thermoélectrique dans une jonction à boîte quantique unique, du régime de couplage faible au régime de couplage fort Kondo. Nos expériences introduisent une nouvelle façon de mesurer le pouvoir thermoélectrique en réalisant une condition de circuit ouvert quasi-parfaite. Le pouvoir thermoélectrique dans une boîte faiblement couplée montre le comportement e-périodique avec la charge induite

par la grille, alors qu'il montre une période distincte de 2e en présence de corrélation Kondo. L'étude de la dépendance thermique révèle que la résonance de Kondo n'est pas toujours au niveau de Fermi, mais qu'elle peut être légèrement décalée, en accord avec les prédictions théoriques.

Cette étude ouvre la porte à l'étude de transistors à une boîte quantique unique dont les propriétés thermodynamiques sont régies par les lois de thermodynamique quantique.

Table of contents

List of figures

List of tables

Introduction

*E*nergy harvesting and its conservation is a very important issue now a days, since the natural resources of energies are limited and going towards the end of its limit. One possible way to overcome this crisis of energy could be by converting the wasted heat into some useful form by the means of thermoelectric effects, so that it can be further used in some other purpose.

When two heat reservoirs at different temperatures are coupled to each other, a potential difference is generated between them. This is well known as the *Seebeck effect*. As a result, a flow of current is generated from the cold reservoir to the hot one, while at the same time there is flow of heat from the hot reservoir to the cold one. A *heat engine* that operates between the two reservoirs can reverse the direction of current thereby converting the heat into some useful work. The *figure of merit*, a measure for the efficiency of an engine can be defined by the ratio of the two quantities, 1) the power generated by the electrons against the thermally originated bias, which depends on the electrical conductance, the Seebeck coefficient or the thermopower and the temperature difference, 2) the direct heat conduction between the reservoirs, which depends on the thermal conductance of the system and the temperature difference. In order to improve the efficiency of an engine one therefore needs to increase the electrical conductance and thermopower, while at the same time reduce the thermal conductance of the system.

In bulk materials, the electric and thermal conductances are related to each other by the Wiedemann-Franz (WF) law. This essentially states that the transport electrons carry a charge 'e' and heat of the order of $k_B T$, where k_B is the Boltzmann constant, making the ratio of the two conductances per unit temperature, a constant L_0, the universal Lorenz number. Therefore, in bulk materials one can not increase the electrical conductance independent of the thermal conductance. The thermopower results from the asymmetry in the spectral density of the system near Fermi-energy. In bulk materials, having a constant density of states near the Fermi energy, one can not expect to get a large thermopower. Therefore, an engine with bulk thermoelectric materials shows very low efficiency.

However, if one can modify the system between the two reservoirs, such that it possesses an energy dependent spectral density, it is possible to manipulate both the conductance ratio

and the thermopower and hence the efficiency of an engine. Thermoelectric materials at the nano-dimensions can meet these requirements [1–5].

A single-Electron Transistor (*SET*) is consists of a small metallic island connected to the leads through tunnel barriers and kept under the influence of a gate electric field [6]. With the reduction of the dimensions of the island, electron interactions gain capital importance, leading to Coulomb blockade in the transport processes. This results in a charging energy that requires to charge the island with an extra electron. It defines the temperature and bias thresholds below which single-electron physics appears. In the regime where charge transport is governed by unscreened Coulomb interactions, the question of the associated heat flow has been addressed by several theoretical studies [7–14]. The Wiedemann-Franz law is expected to hold in an SET only at the charge degeneracy points in the limit of small transparency, where the effective transport channel is free from interactions, and is violated otherwise. Therefore, in such systems one can vary the ratio of the two conductances beyond the *WF law* predicted value. Since an *SET* can be used as an element of the microelectronic circuits, the study of heat flow through it and its management is very important [15].

A Quantum-Dot (*QD*) junction is a kind of *SET* where the 'island' dimensions are reduced down to the size of only few atoms, therefore in addition to the Coulomb interactions the quantum effects are also become important in the transport processes. As a result of the quantum confinement the energy spectrum of the 'island' splits into several discrete electronic levels. The spectral function of the *QD* consists of several resonant peaks corresponding to the discrete energy levels, with a width (determined by the tunneling rate of electrons) much smaller than $k_\mathrm{B}T$ and hence it can feature a strong asymmetry around the Fermi energy. Therefore, a *QD* could be a perfect candidate to be deployed as an engine between the two reservoirs. Due to the strong asymmetry in the spectral density near Fermi energy one can get a large thermopower signal. The resonant levels of the *QD* can also act as an energy filters for the low-energy transfer process in order to reduce the unfiltered direct heat flow [16]. By manipulating its resonant energy levels one can achieve a very high efficiency close to the thermodynamic limits. However, experimentally such an efficient *QD* heat engine is not fully realized yet, due to the experimental difficulties in combining the charge and heat transport measurements [17].

In this thesis we have considered the study of the thermal and thermoelectric transport in an *SET* and a *QD* junctions. The prediction of the violation of WF law in an *SET* is tested by measuring the heat flow through it. A strong signal of the thermopower, measured in *QD* junctions hints the crucial information about the spectral density of the device, including the exact position of the Kondo resonance in the case of a Kondo correlated *QD*.

The thesis is organized in the following way:

Chapter 1: introduces a brief theoretical description of the charge and heat transport in an *SET* and a *QD* junction. Here we consider both first order sequential tunneling and the second order co-tunneling processes. The effect of Quantum correlation on the electrical and thermoelectric transport properties of a *QD* junction are also considered.

Chapter 2: gives the experimental techniques for the fabrication of *SET* and the *QD* junctions studied in this thesis, including the crucial steps like electromigration, gold nanoparticle depostion etc.

Chapter 3: gives a general discussion on local thermometry and refrigeration integrated to mesoscopic devices. Here we describe two types of mesoscopic-local thermometers based on, Superconductor-Normal metal tunnel junctions, the *NIS* tunnel junction thermometer, and Superconductor-Normal metal-Superconductor transparent junctions, the proximity Josephson junction *SNS* thermometer.

Chapter 4: describes the experimental results on the measurement of thermal conductance of an *SET*. It includes the heat-flow measurements through the *SET* and its operation as a heat-switch. A strong violation of the WF law away from the charge degeneracy is observed.

Chapter 5: describes the experimental results on the measurements of thermal balance and thermoelectric effects in *QD* devices in different coupling regimes. It includes, first, a general charge conductance characterization of a *QD* made of evaporated *Au* nanoparticles, then an experiment of heat-balance between two heat reservoirs through a single *QD* level. After that we describe the thermopower measurements in a weakly coupled *QD* junction and at the last but not the least the thermopower measurements in a Kondo spin-correlated *QD* junction and its temperature dependence.

Chapter 1

Quantum Transport: Charge and Heat

The transport of heat is associated with the transport of charge carriers. In a bulk metallic structure, in the absence of interactions, carriers, the electrons, carry a charge e and heat of the order of $k_{\mathrm{B}}T$, where k_{B} is the Boltzmann constant and T is the equilibrium temperature of the electronic distribution. In mesoscopic quantum devices the presence of interactions (between the electrons) however can modify the picture a lot. Interactions can introduce an energy filtering in the process of transport. As a result, although the carriers carry the same amount of charge e, they can carry more (or less) heat than what one would naively expect.

We frame the chapter in a way to consider the charge and heat transport, for a Single-Electron transistor (*SET*) and a Quantum-Dot (*QD*) junction in parallel. In the first section (Sec.1.1) we consider the charge transport through such devices while thermal and thermo-electric transport are discussed in the second section (Sec.1.2).

1.1 Charge Transport in Quantum Devices

In this section we consider the transport of charges though devices where electrons are subject to strong electronic interactions. We start with the basic discussion of tunneling of electrons through a single tunnel barrier (Sec. 1.1.1). We then consider the charge transport though a small metallic island, connected to the rest of the world by only tunnel barriers, and the effect of Coulomb-interaction (Sec. 1.1.2). In addition to Coulomb interaction, we will consider the quantum effects as we reduce the size of the island, in a *QD* junction (Sec. 1.1.3). Second order processes of charge transport, like co-tunneling, will then be considered for both semi-classical metallic island and quantum-Dot (Sec. 1.1.4). The effect of *spin-correlation* in the charge transport will be discussed in the last part of this section (Sec. 1.1.5).

1.1.1   Tunneling of Electrons through a single barrier

Let us first consider the simple case of a tunnel junction, where two electronic reservoirs are connected through a tunnel barrier. The electrons in the reservoir are non-interacting and can be considered as *free electrons*. The free electrons in the metallic reservoir obey Fermi-Dirac statistics. The distribution of electrons with energy E (w.r.t the Fermi energy E_F) and at a well defined temperature T is given by

$$f(E) = \frac{1}{1 + e^{E/k_B T}}. \tag{1.1}$$

Here the Fermi energy E_F is taken as a reference for all energy measurements, i.e. $E_F = 0$. The Hamiltonian of the system can be written as follows,

$$\hat{H} = \hat{H}_1 + \hat{H}_2 + \hat{H}_{12} \tag{1.2}$$

where $\hat{H}_1$ and $\hat{H}_2$ are the free electron Hamiltonian of the two reservoirs 1 and 2, respectively and are given by $\hat{H}_1 = \sum_k \varepsilon_k a_k^\dagger a_k$ and $\hat{H}_2 = \sum_q \varepsilon_q c_q^\dagger c_q$. The tunneling between them is presented by the interacting Hamiltonian $\hat{H}_{12} = \sum_{k,q} \left(\tau_{k,q} a_k^\dagger c_q + \tau_{k,q}^* a_k c_q^\dagger \right)$, where ε_k and ε_q are the energy of the conduction electrons of the two reservoirs. The Fermi-Dirac distribution in the two reservoirs give $\langle a_k^\dagger a_k \rangle = f_1(\varepsilon_k)$ and $\langle c_q^\dagger c_q \rangle = f_2(\varepsilon_q)$.

Using Fermi's golden rule, the tunneling rate of electrons from the reservoir 1 to 2 with an energy cost ΔE for each tunneling can be written as

$$\Gamma_{1 \to 2}(\Delta E) = \frac{2\pi}{\hbar} \sum_{k,q} |\tau_{k,q}|^2 \langle a_k^\dagger a_k c_q^\dagger c_q \rangle \delta(\varepsilon_q - \varepsilon_k + \Delta E), \tag{1.3}$$

where $\delta(x)$ is the Dirac delta function, $\int_{-\infty}^{\infty} \delta(x) dx = 1$. The summations can be converted into integrals using the general formalism, $\sum_k = \int D_1(\varepsilon_k) d\varepsilon_k$ and $\sum_q = \int D_2(\varepsilon_q) d\varepsilon_q$, where $D_1(\varepsilon_k)$ and $D_2(\varepsilon_q)$ are the density of states of the two reservoirs respectively. With the approximation $|\tau_{k,q}|^2 = |\tau|^2 = $ constant, the tunneling rate can be written as

$$\Gamma_{1 \to 2}(\Delta E) \approx \frac{1}{e^2 R_T} \int d\varepsilon n_1(\varepsilon) f_1(\varepsilon) n_2(\varepsilon - \Delta E)[1 - f_2(\varepsilon - \Delta E)], \tag{1.4}$$

where $n_i(\varepsilon) = D_i(\varepsilon)/D_i(0)$ is the normalized density of states (*DOS*) of the two reservoirs, where $i = \{1, 2\}$. The tunnel resistance is defined as, $R_T = \hbar/(2\pi e^2 |\tau|^2 D_1(0) D_2(0))$.

For the case of a *NIN* tunnel junction, both of the reservoirs are normal metallic. The *DOS* of the normal metal near the Fermi level can be considered as constant, therefore we can use $n_1 = n_2 = 1$. With an equal temperatures for the two normal metals, $T_1 = T_2$, the

tunnel rate can be simplified as,

$$\Gamma_{1\to 2}(\Delta E) = -\frac{1}{e^2 R_T}\frac{\Delta E}{1 - e^{\Delta E/k_B T}}, \tag{1.5}$$

using the identity for the Fermi-Dirac integral, $\int_{-\infty}^{\infty} dy f(y)\left[1 - f(y+x)\right] = x(1 - e^{-x/k_B T})^{-1}$. Since each electron carries a charge $-e$, the tunnel current from reservoir 1 to 2 is

$$I_{1\to 2} = -I_{2\to 1} = \frac{1}{e R_T}\frac{\Delta E}{1 - e^{\Delta E/k_B T}}. \tag{1.6}$$

If one of the normal metal reservoirs is replaced by a superconducting reservoir, forming a *NIS* junction, the tunnel rates include an extra contribution from the energy dependent density of states of the superconductor near the Fermi level. The tunnel rates of charge transport in a *NIS* tunnel junction is considered in Chapter 3 (Sec. 3.1).

1.1.2 Charge transport in an SET

We now consider the transport of charges in a Single-Electron transistor (SET), where a small metallic *island* is kept isolated from the rest of the world. The island is coupled to two electronic reservoirs via tunnel barriers, called the *source* and *drain* of the transistor. Apart from this two tunnel coupled reservoirs, the island is capacitively coupled to another electrode, called the *gate*. The gate induces electrostatic charges on the island and as a result can control its electrostatic energy. One can consider this system as a set of two single tunnel junctions, except from the fact that the energy cost for tunneling (ΔE) of electrons includes an extra contribution arising from the strong Coulomb interaction. The circuit diagram of an *SET* is shown in Fig. 1.1, where the island has n excess electrons i.e. the SET is in the nth charge state. The tunnel rates of electrons to (from) the island are indicated by the superscript $+(-)$. The subscript indicates the involved tunnel junction and the island respectively. The electronic distribution in the leads and the island are considered to be of Fermi-Dirac form $f_i(\varepsilon) = 1/(e^{(\varepsilon/k_B T_i)} + 1)$ and $f_I(\varepsilon) = 1/(e^{(\varepsilon/k_B T_I)} + 1)$, respectively, where $T_i \equiv T_1, T_2$ and T_I are the equilibrium electronic temperature of the leads and the island.

Using the formalism of tunnel rates in a single tunnel junction (Eq. 1.4) we can write the tunnel rates in the *SET* as follows [18, 6],

$$\Gamma_{i,n}^+ = \frac{1}{e^2 R_{T,i}}\int d\varepsilon\, n_i(\varepsilon) f_i(\varepsilon)[1 - f_I(\varepsilon - \Delta E_{i,n}^+)] \tag{1.7}$$
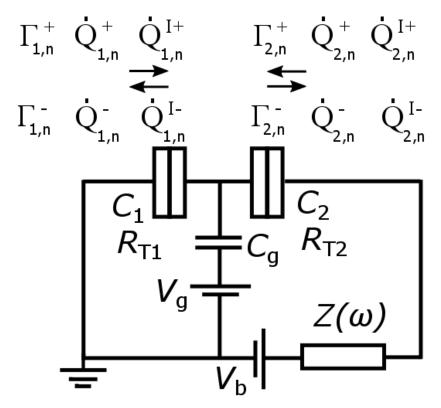
Fig. 1.1: Circuit diagram of an SET   Circuit diagram of an SET in the nth charge state, indicating the tunnel rates and heat current. Heat current will be discussed in Sec. 1.2.3. Subscripts in the tunnel rates and heat currents, i and n indicates the corresponding leads and the island respectively, where i can take two values, $i = \{1,2\}$. The superscripts $+$ or $-$ indicate the tunneling to the island and from the island respectively.

and

$$\Gamma_{i,n}^{-} = \frac{1}{e^2 R_{T,i}} \int d\varepsilon\, n_i(\varepsilon - \Delta E_{i,n}^{-}) f_I(\varepsilon)[1 - f_i(\varepsilon - \Delta E_{i,n}^{-})], \tag{1.8}$$

where the energy cost of tunneling to (from) the island is given by,

$$\Delta E_{i,n}^{\pm} = \pm 2E_c(n - n_g \pm 1/2) \pm eV_{b,i}, \tag{1.9}$$

with the gate induced charge $n_g = C_g V_g/e$ and the charging energy $E_c = e^2/2C$, where $C = C_1 + C_2 + C_g$ is the sum of the capacitances of the island to the three leads, the source, drain and gate respectively. $V_{b,i} = k_i V_b$ is the fraction of the total applied voltage V_b across the junction i and $k_i = \tilde{C}/C_i < 1$, where $\tilde{C} = C_1 C_2/(C_1 + C_2)$ is the equivalent series capacitance of the two junctions. For a symmetric *SET*, $k_1 = k_2 = 1/2$. For the sake of generality, the density of states of the *SET* leads $n_i(\varepsilon)$ are taken to be energy dependent, while the DOS of the island is taken as constant and hence $n_I = 1$.

The four tunneling processes for electrons from (to) the leads to (from) the island are possible only when the related energy cost given by Eq. 1.9, $\Delta E_{i,n}^{\pm} \lesssim 0$. These four conditions of tunneling define an area in the $n_g - V_b$ plane, where the transport of charge is blocked. Such diamond shaped blockade regions are well known as the Coulomb-diamonds, as shown in Fig. 1.2 (a). Within each diamond, the *SET* island remains in a stable charge state, n. Intersection of the two diamonds corresponding to two charge states is known as the charge degeneracy point, where the island can be in both of the charge states. The extent of such diamonds along the V_g axis and the corresponding half-extent of the diamonds along the V_b axis can be found to be $2E_c/e$.
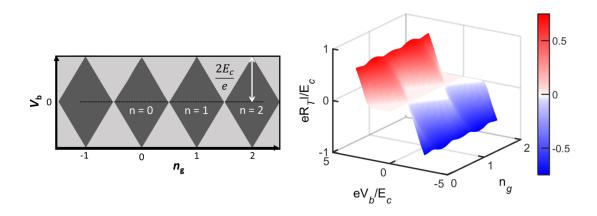
Fig. 1.2:   Stability diagram of an SET   (left) The sketch of the charge stability diagram for an *SET*. Diamond shaped regions have a stable charge and are known as the Coulomb diamonds. Charge transport is blocked in this region. The meeting points of the two stable charge diamonds are called the charge degeneracy points, where the charging energy is zero. Outside the Coulomb blockade region, the charge transport is not blocked by Coulomb interactions. The extents of the diamonds give an estimate of the charging energy. (right) Calculated current through an *SET* [Eq. (1.12)] as a function of bias V_b and gate-induced charge n_g.

The rate of change of the occupation probability $p(n)$ is given by the master equation for the *SET* tunnel rates,

$$\dot{p}(n) = p(n+1)\left(\Gamma_{1,n+1}^{-} + \Gamma_{2,n+1}^{-}\right) + p(n-1)\left(\Gamma_{1,n-1}^{+} + \Gamma_{2,n-1}^{+}\right)$$
$$- p(n)\left(\Gamma_{1,n}^{+} + \Gamma_{2,n}^{+} + \Gamma_{1,n}^{-} + \Gamma_{2,n}^{-}\right). \tag{1.10}$$

At the steady state, $\dot{p}(n) = 0$. The probability $p(n)$ can be obtained from the detailed balance equation as

$$p(n) = \frac{p(n+1)\left(\Gamma_{1,n+1}^- + \Gamma_{2,n+1}^-\right)}{\left(\Gamma_{1,n}^+ + \Gamma_{2,n}^+\right)}, \tag{1.11}$$

with the condition that $\sum_{n=-\infty}^{\infty} p(n) = 1$. The tunnel current can be obtained from the occupation probability $p(n)$ and the tunnel rates as follows,

$$I \equiv I_1 = -I_2 = -e \sum_{n=-\infty}^{\infty} p(n)\left(\Gamma_{i,n}^+ - \Gamma_{i,n}^-\right); \quad i = \{1, 2\}. \tag{1.12}$$

The calculated average tunnel current through the *SET* is plotted in Fig. 1.2 (right), as function of the applied bias voltage V_b and the gate induced charge n_g. The *white* colored regions of zero current, form the Coulomb-diamonds, where the transport is blocked.

1.1.3 Charge transport in a QD

We now consider the effects of quantum confinement in addition to the Coulomb interaction for the charge transport in a Quantum-Dot (*QD*) junction. According to the De Broglie's wave-particle duality theory, every particle has a wave nature with a wavelength determined by the linear momentum of the particle, called the De Broglie wavelength, $\lambda_d = h/P$, where h is the Plank's constant and P is the linear momentum of the particle. In a bulk metal the electrons are free to move around throughout the metal. They are free from the interaction with the atoms, as well as from the interaction with the other electrons. The motion of the electrons can be satisfactorily described by the linear combination of the plane waves, having a wavelength of the order of few nano-meters, which is much smaller than the size of the metallic structure itself and hence a classical theory can explain the motion of the electrons in such a system. If the dimensions of the system are comparable to the wavelength of electrons, the free electrons in the structure behave like particles trapped in a box, whose motion is described by the theory of quantum mechanics. The solutions of Schrödinger equation for the motion of a particle are standing waves confined in the potential well. The energy associated with each wave function is discontinuous and unequally spaced. Therefore, the continuous energy spectrum of the free electrons splits into few discrete energy levels, i.e. the electrons are not allowed to have an arbitrary value of energy, but only certain discrete ones.

The electrostatic behavior of the electrons in the *QD* can be explained by the constant-interaction model [19, 20]. It considers that the *QD*-island can only be occupied by an integer number of electrons, implying that the total charge of the island is $Q = -Ne$, N being an

integer. Therefore at equilibrium an effective potential difference arises between the *QD* and the external reservoirs. The total charge in the island is then governed by the external potentials as

$$Q = \sum_i C_i(\phi(Q) - V_{ext,i}),$$ (1.13)

where C_i and $V_{ext,i}$ are the corresponding capacitance and the external voltage applied to the reservoirs. The total capacitance of the *QD* to the reservoir is $C = \sum_i C_i$. The effective electrostatic potential of the *QD* at equilibrium can thus be written as

$$\phi(Q) = \frac{Q}{C} + \phi_{ext},$$ (1.14)

where the potential due to the external reservoirs is $\phi_{ext} = \sum_i \frac{C_i}{C} V_{ext,i}$. Therefore, the electrostatic energy of the *QD* with N electrons is,

$$E_{el}(N) \equiv \int_0^{-Ne} \phi(Q)dQ = \frac{(Ne)^2}{2C} - Ne\phi_{ext}.$$ (1.15)

Due to the discretization of the energy levels, apart from the electrostatic energy, the total energy of the N electron *QD* also includes the sum of the distribution of the electrons in the single particle levels, therefore the total energy of the *QD* is,

$$E_{total}(N) = \sum_p \varepsilon^p + E_{el}(N).$$ (1.16)

The chemical potential of the *QD* w.r.t the Fermi-energy of the reservoir is defined as the energy required to add an extra electron to the $(N+1)$th energy level ε_{N+1},

$$\mu(N) = E_{total}(N+1) - E_{total}(N) = \varepsilon_{N+1} - e\phi_{ext} + (N+1/2)\frac{e^2}{C}.$$ (1.17)

This is the total energy cost for tunneling of an electron. Note that, with some simplification of the above equation, one can find that the energy cost for tunneling in a *QD* has an extra term, compared to the case of 'metallic island' *SET* (Eq. 1.9), which comes from the energy of the particular level ε_{N+1}. This arises due to the finite level spacing $\delta E > k_B T$.

The energy diagram of a $N - QD - N$ junction is shown in Fig. 1.3. The electrons in the normal metal reservoir are considered to be free described by the Fermi-Dirac distribution. The *QD* is presented by a set of discrete energy levels with a finite level spacing δE. In the sequential tunneling regime, tunnel coupling of the left and right reservoirs to the *QD*, Γ^l and Γ^r, respectively are considered to be very small compared to both temperature and the electronic level spacing δE, i.e. $h(\Gamma^l + \Gamma^r) << k_B T, \delta E$.
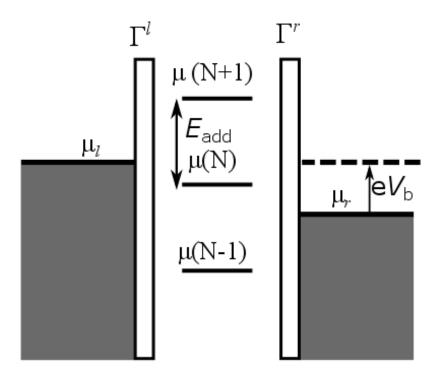
Fig. 1.3:   Energy diagram of a QD junction   The energy diagram of a $N - QD - N$ junction, where a QD is coupled to two metallic reservoirs via tunnel barriers with the tunneling rates Γ^l and Γ^r for the left and right barrier respectively. A relative bias V_b is applied between the two reservoirs. The QD is represented by the discrete energy levels. The chemical potential of the QD is shown here. The energy difference between the two levels is $E_{add} = 2E_c + \delta E$. In the particular situation shown here, the conduction is maximum since the QD level is situated at the middle of the bias-window eV_b.

Transport of charges in a QD junction with the application of a voltage bias V_b between the two reservoirs, at a given gate voltage is possible when the applied bias can provide the required energy-cost for tunneling. In the sequential tunneling regime, the tunneling of the electrons can be considered as elastic. The conservation of energy for the tunneling of an electron from the left reservoir with energy $E^{i,l}$ to the pth level of the QD requires that,

$$\varepsilon^{i,l} = \varepsilon^p - e\phi_{ext} + (N + \frac{1}{2})\frac{e^2}{C} + \eta eV_b, \tag{1.18}$$

where ηV_b is the voltage drop over the left tunnel barrier. The reverse elastic tunneling from the pth state of the QD to the left reservoir with energy $E^{f,l}$ sets the following condition,

$$\varepsilon^{f,l} = \varepsilon^p - e\phi_{ext} + (N - \frac{1}{2})\frac{e^2}{C} + \eta eV_b. \tag{1.19}$$

For the tunneling through the right tunnel barrier with a voltage drop $(1 - \eta)V_b$, two other similar conditions need to be met.

The tunnel current through the left tunnel barrier can be written as

$$I = -e \sum_p \sum_{n_i} \Gamma_p^l P(\{n_i\}) \left\{ \delta_{n_p,0} f(E^{i,l}) - \delta_{n_p,1} [1 - f(E^{f,l})] \right\} \tag{1.20}$$

where $P(\{n_i\})$ is the occupation probability of the QD to be found in the state n_i, for a non-degenerate state $n_i = 0, 1$. The steady state condition of rate equation for the occupation probability gives a set of detailed balance equations. One needs to solve them to calculate the tunnel current exactly. A linear-response theory to solve the detailed balance equation has been given by Beenakker [21], an extension of a classical theory by Kulik et al. [22], by considering that the equilibrium distribution of the electrons in the QD levels is governed by the Gibbs distribution. Following the review [21], the tunnel current and the conductance $G_{QD} = (I/V_b)|_{V_b \to 0}$ can be calculated analytically. For $\hbar\Gamma << k_B T << \delta E$, the conductance of the $N - QD - N$ junction at a finite temperature can be written as,

$$G_{QD} = \frac{e^2}{4k_B T} \frac{\Gamma^l \Gamma^r}{\Gamma^l + \Gamma^r} \cosh^{-2} \left(\frac{\Delta_{min}}{2k_B T} \right), \tag{1.21}$$

where $\Delta_{min} = \mu(N_{min})$ (Eq. 1.17) is the minimum energy gap to add an electron to the QD, N_{min} is defined such that the probability $P(N)$ is negligible for all other non-integer states, i.e., $N \neq N_{min}$ and $N \neq (N_{min} - 1)$.

The charge transport though the QD junction is possible with the application of a voltage bias V_g on the gate, with a constant bias on the reservoirs. The electrostatic potential by the gate induced charges $Q_{ext} = C_g V_g = en_g$ can reduce the total energy gap for tunneling (Eq. 1.17) and hence transport becomes possible. A peak in conductance is observed when the total energy cost of tunneling becomes zero, i.e. $\mu(N) = 0$ for some integer $N = N_{min}$. Therefore, we can write from Eq. (1.17) with $\mu = 0$

$$e\phi_{ext} = \varepsilon_{N+1} + \left(N + \frac{1}{2} \right) \frac{e^2}{C}. \tag{1.22}$$

Substituting $\phi_{ext} \equiv Q_{ext}/C = C_g V_g/C = \alpha V_g$, where $\alpha = C_g/C$ is the gate coupling factor, we can rewrite the above equation as

$$e\alpha V_g = \varepsilon_{N+1} + \left(N + \frac{1}{2} \right) \frac{e^2}{C}. \tag{1.23}$$

Therefore, the conductance of the QD junction oscillates with the gate voltage V_g and obtains its maximum whenever the above condition (Eq. (1.23)) is satisfied. In each period the number of electrons in the QD is changing by one. The periodicity of the oscillations can be
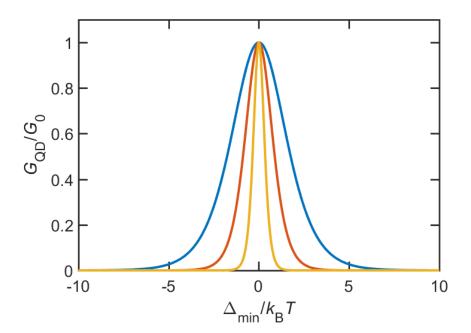
Fig. 1.4: Conductance of a QD junction Line-shape for the conductance of a *QD* junction at different temperatures based on Eq. 1.21. G_0 is the maximum conductance given by the prefactor in the same formula, depending on the tunnel rates.

obtained from Eq. (1.23) as,

$$E_{add} = e\alpha\Delta V_g = \delta E + 2E_c, \tag{1.24}$$

where δE is the level-spacing. The calculated conductance for a *QD* junction based on Eq. (1.21) is shown in Fig. 1.4. A schematic of the stability diagram of the *QD* junction conductance in the $V_g - V_b$ plane is shown in Fig. 1.5.

Coulomb-diamond analysis

Analysis of the stability diagram of the conductance is very useful for characterizing the *QD* junction, in order to extract different relevant parameters, including the charging energy of the dot E_c, the capacitances of the dot to the leads C_s, C_d and the asymmetry between them, the gate coupling factor α, the level spacing of the quantized energy levels δE etc. [23, 24].

   If we first consider the *ground state* of the quantized electronic levels in the dot, the current-voltage characteristics of the *QD* junction consist of sharp steps whenever the chemical potential of the dot aligns with the chemical potential of the leads and constant current plateaus when the dot's chemical potential lies in between. The sharp steps give rise to peaks in conductance at a constant gate voltage. The positive and negative slopes of the
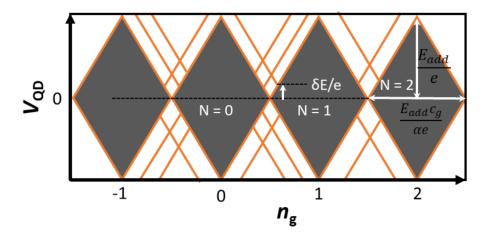
Fig. 1.5: Stability diagram of a QD junction Schematic of charge stability diagram for a *QD* junction. The diamond shaped regions have a stable charge and are well known as Coulomb diamonds. Charge transport is blocked in this region. The meeting point of the two charge diamonds is called the charge degeneracy point with vanishing charging energy. The line structures outside the Coulomb-blockade region are corresponding to different levels of the *QD*.

Coulomb diamonds edges correspond to a particular combination of bias voltage (V_b) and gate voltage (V_g) on the $V_b - V_g$ plane (Fig. 1.5), for which dot's chemical potential aligns to that of the source and drain respectively. These situations are determined by the energy conservation relations (one such equation is given by Eq. (1.18)) for the tunneling in or out of the dot through the tunnel barriers. Solving the energy conservation relations, we find that the positive and negative edges of the Coulomb diamonds (Fig. 1.5) are characterized by the following two linear equations respectively,

$$
\begin{aligned}
V_b &= \beta V_g + k, \\
V_b &= -\beta' V_g + k.
\end{aligned}
\tag{1.25}
$$

The positive slope of the diamond is $\beta = C_g/(C_d + C_g)$, while negative slope is $\beta' = C_g/C_s$, where C_s, C_d, C_g being the capacitance between the dot and source, drain and the gate respectively. The total capacitance of the dot with the environment is $C = C_s + C_d + C_g$. The constant k in Eq. (1.25) represents the potential of the dot in the absence of any external voltage. The slopes of a diamond therefore characterize a specific *QD*. As we will see in the experiment (Sec. 2.2.4) that the deposition of nano-particles is a stochastic process and there can be more than one particle coupled to the leads at different gate voltages, the slopes of the diamond can help us to easily identify a particular nano-particle, with periodic diamonds corresponding to the same nano-particles.

The slopes of the diamond edges provide information about the asymmetry in the capacitive coupling of the dot to source and drain. This is given by,

$$\frac{C_\text{d}}{C_\text{s}} = \beta'(\frac{1}{\beta} - 1). \tag{1.26}$$

The gate coupling factor α, also known as the *lever-arm*, is defined as the effective change in the chemical potential of the dot per unit voltage applied on the gate, $\alpha = \frac{\Delta\mu}{\Delta V_\text{g}}$. It can be directly obtained from the two slopes of the diamond edges as,

$$\alpha = \frac{C_\text{g}}{C} = \frac{1}{(\frac{1}{\beta} + \frac{1}{\beta'})} \tag{1.27}$$

The charging energy of the dot is determined by the extents of the Coulomb diamonds along the both axis. We have seen that the conductance peaks are observed when the applied gate voltage satisfies the condition of Eq. (1.23), which leads to a period of oscillation $E_{add} = (2E_\text{c} + \delta E)$. If we consider the zero bias line along the n_g axis, the addition of an extra electron into the next closest ground state of the dot is only possible when the applied voltage on the gate can provide the required additional energy E_add. Therefore, the horizontal extent of the diamond in Fig. 1.5 is given by $\Delta V_\text{g} = E_\text{add}/\alpha e$. In a similar manner, if we consider a constant gate voltage at the middle of the Coulomb diamond, the Coulomb blockade is lifted when the applied bias voltage can provide the required energy E_add and the extent of the diamond along the bias axis (Fig. 1.5) is $\Delta V_\text{b} = E_\text{add}/e$. Therefore the extents of the Coulomb diamonds can easily give an estimate of the addition energy E_add.

The conductance map of the *QD* can also be used as a spectroscopic tool to observe the quantization of the energy and to get a direct estimate of the spacing between two electronic levels. The *ground-state* of a particular level of the *QD* gives rise to the highly conductive Coulomb edge when it aligns with the chemical potential of the leads. If we further increase the bias voltage (w.r.t drain), at some value of the bias voltage, the chemical potential of the source become equal to the chemical potential of the first excited state of the dot. In this situation, the *bias-window* (eV_b in Fig. 1.3) holds both the ground state and the first excited state of the *QD* level and therefore two channels are available for the transport through the same charge state. A sharp step in current and a peak in the conductance is thus expected. This is shown as highly conductive line-structures running parallel to the Coulomb edges in Fig. 1.5. Every highly conductive line for the excited state intersects with the Coulomb-edge of its own ground state. Therefore the level spacing can be obtained from the value of V_b at which the line intersects with the Coulomb edge, measured from the zero bias line given by,

$\delta E = (e\delta V_{\mathrm{b}}/2)$, where δV_{b} is the bias voltage at which the line intersects with the Coulomb edge.

Another important parameter of the *QD* is the tunneling rate of electrons from the leads to the *QD*. This can be directly obtained from the steps in the current across the *QD* as a function of V_{b}. The height of the steps for negative and positive bias voltage give the asymmetry in the tunnel coupling of the dot to the leads. The tunneling rates from source Γ^l and from drain Γ^r to the dot are given by [25],

$$
\begin{aligned}
I_+ &= 2|e|\frac{\Gamma^l\Gamma^r}{(2\Gamma^r + \Gamma^l)} \\
I_- &= -2|e|\frac{\Gamma^l\Gamma^r}{(\Gamma^r + 2\Gamma^l)}
\end{aligned}
\tag{1.28}
$$

where I_+ and I_- are the steps in the $I_{\mathrm{QD}} - V_{\mathrm{b}}$ characteristics for positive and negative bias respectively.

1.1.4 Higher order transport: co-tunneling

Till now we have considered the charge transport only by first-order tunneling events through the *metallic-island SET* or the *QD*. The latter is suppressed exponentially with temperature, inside the Coulomb blockaded region (can be seen from Eq. (1.21) for *QD*). At low enough temperature, higher order tunneling events can become the dominant process of charge transport inside the Coulomb-diamonds. This is commonly known as co-tunneling processes since they involve the simultaneous tunneling of multiple electrons [26]. Although the total energy in the process is conserved, these tunneling events may leave the electronic distribution of the island in an excited state, depending on which the co-tunneling events are classified as *elastic* and *in-elastic*. The co-tunneling process is called *in-elastic* when at the end of the tunneling process the electronic distribution in the island remains in an excited state. Otherwise if the virtual process occurs through the ground-state and the electronic distribution of the island remain in its ground-state, it is called *elastic* co-tunneling.

In a *metallic-island SET*, co-tunneling occurs through many levels [28–30]. The process is present for a strong coupling between the island and the leads. Off-resonance and at low temperature the onset of co-tunneling is determined by the condition, $\Delta_N >> k_{\mathrm{B}}T$, where Δ_N is the charging energy gap given by Eq. (1.9).

In a *QD* junction, when tunnel the couplings of the *QD* with the leads are very strong, so that the tunneling conductance is comparable to the quantum of conductance $2e^2/h$,
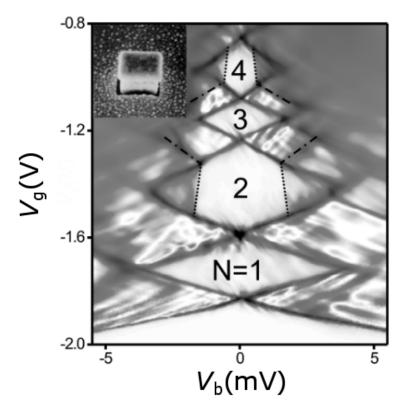
Fig. 1.6: Conductance map of a QD in the presence of co-tunneling for four charge states
(Adapted from De Franceschi et al. [27]) Co-tunneling is present inside the Coulomb diamonds. For
the odd diamonds (N = 1, 3), co-tunneling processes are fully elastic, while for the even diamonds (N
= 2, 4), co-tunneling is elastic only for a bias $eV_b \lesssim \pm\delta E$, shown by the dotted line. The inelastic
co-tunneling sets in for a bias $|eV_b| \gtrsim \delta E$.

the second-order tunneling of electrons becomes non-negligible. As a result a non-zero
conductance is observed inside the Coulomb diamonds.

The *elastic* co-tunneling occurs near zero bias, where the virtual tunneling of one electron
from the ground state $E(N)$ of the *QD* to the low-energy reservoir, leads to the tunneling of
another electron from the high energy reservoir to the ground state of the *QD*, leaving the
QD in its ground state. This virtual two-electron process transfers an electron from the left to
the right reservoir.

In the case of *inelastic* co-tunneling, an electron tunnels to the excited state $E^*(N)$ of the
QD from the high-energy reservoir, followed by the virtual tunneling of an electron from
the ground state $E(N)$ to the low-energy reservoir. As a result, the electronic distribution of
the *QD* is left in the excited state, with an extra energy of $|E(N) - E^*(N)| = \delta E$. This extra
energy is supplied by the external bias eV_b. Therefore, the onset of the *inelastic* co-tunneling
inside the Coulomb diamond is set by the external bias $|eV_b| \gtrsim \delta E$.

The co-tunneling transport in a vertical *QD* embedded in an InGaAs layer has been measured by De Franceschi et al. [27]. Fig. 1.6 shows the conductance map of the *QD* junction for four charge states. The strong tunnel coupling of the island with the leads allows the co-tunneling to set-in inside the Coulomb diamonds, producing a non-vanishing conductance. For the odd Coulomb-diamonds, the transport processes are solely governed by elastic co-tunneling, since the addition energy, $E_{add} \equiv E_c < \delta E$. But for the even diamonds $E_{add} \equiv E_c + \Delta(N) > \delta E$ and hence a co-existence of both elastic and inelastic co-tunneling is found. For low bias, transport is dominated by elastic co-tunneling, while inelastic co-tunneling sets in for $|eV_b| \gtrsim \delta E$.

1.1.5 Spin correlation: Kondo effect

In a metal, the resistivity at high temperature is related to the interaction of electrons with both electrons and phonons, but as one goes to the low temperature limit, the phonon contribution reduces as T^5 and below the Debye temperature the resistivity is only due to electron-electron interaction and it is expected to saturate. But instead of saturation, for an impure-*Au* an increase of the resistivity at low temperature was observed, exhibiting a minimum in the resistance versus temperature curve [31]. The same effect was also evidenced in the low temperature resistivity measurement of alloys with specific amount of magnetic impurity [32]. This was first explained by J. Kondo [33], taking into account an anti-ferromagnetic coupling between the spin of the impurity in the metal and the conduction electrons. He predicted a logarithmic increase of the resistivity at low temperature, which eventually diverges with temperature. But this logarithmic divergence of the resistivity is unphysical. This problem was solved by Wilson by introducing the renormalization group (*RG*) theory [34]. According to this theory, below a characteristic temperature, known as the Kondo temperature T_K, the anti-ferromagnetic impurity forms a singlet with the conduction electrons. For $T > T_K$ the impurity spin interacts with only few electrons, but for $T < T_K$ due to the presence of Kondo-correlation it is fully screened by the delocalized electrons forming Kondo *spin-cloud*. The full screening of the impurity spin increases the scattering cross-section and hence the resistivity increases. The situation is illustrated in Fig. 1.7(a). Later the numerical renormalization group (*NRG*) was introduced by Costi et al. to obtain the full temperature dependence of the transport coefficients [35, 36].

In the previous section, we have discussed the higher order co-tunneling transport through the *QD* junction, but till now we have not considered the spin of electrons. However, co-tunneling with the spin-conserved transport of electrons can give rise to very interesting features in the transport properties, known as *Kondo effect*. This effect arises in a metallic-island-*SET* or in a *QD* when the doubly degenerate state of the island is occupied by a single
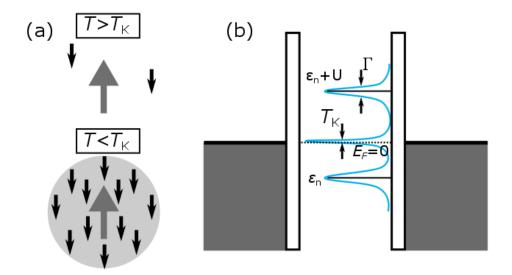
Fig. 1.7: **Kondo spin-cloud and the emerging density of states** (a) Schematic representation of the unpaired spin of the impurity in the metal surrounded by the delocalized spin of the conduction electrons. Above a characteristic temperature T_K, the impurity spin is surrounded by only few spins, but below T_K, the impurity spin is fully screened by the delocalized spin, forming a cloud of spin known as Kondo cloud. (b) Energy diagram of the *QD* in the presence of Kondo correlation at a temperature $T < T_K$. The formation of Kondo cloud opens up a new channel of transport through the tunnel barrier, as a result a new density of states for the electrons emerges near Fermi level.

electron, restricted by the finite charging energy, exhibiting a non-zero spin and hence acting as a magnetic impurity in the system. The Kondo effect in an *SET* tunnel junction structure has been studied for around two decades after the first observation in a lithographically defined *SET* on 2*DEG* system [37].

In the case of a metallic-island-*SET* or a *QD*, the Kondo effect however enhances the conductance rather than the resistance [38, 39], because, the transport process here is the tunneling of electrons and the tunnel current is proportional to the available density of states. The formation of the *Kondo-cloud* below T_K (Fig. 1.7(a)) emerges a peak in the density of states near Fermi energy, which opens up a new channel of transport within the energy range of $k_B T_K$ around the Fermi energy. This is know as the Kondo-resonance, as shown in Fig. 1.7(b).

The transport in the Kondo regime can be described by the Anderson model for magnetic impurities in metal [40]. The Hamiltonian of the *QD* system is then given by,

$$H = \sum_{k,\sigma} \varepsilon_k c_{k\sigma}^\dagger c_{k\sigma} + \sum_{\sigma} \varepsilon_n d_{\sigma}^\dagger d_{\sigma} + U d_{\uparrow}^\dagger d_{\uparrow} d_{\downarrow}^\dagger d_{\downarrow} + \sum_{k,\sigma} \left(v_k d_{\sigma}^\dagger c_{k\sigma} + v_k^* c_{k\sigma}^\dagger d_{\sigma} \right), \qquad (1.29)$$

where the first term describes the kinetic energy of the free electrons in the reservoirs, the second term represents the energy of the localized electron ε_n in the spin-degenerate level,

the third term includes the interactions for the localized electrons in terms of the charging energy U to add the second electron in the same level, while the last term represents the spin conserving tunneling events between the reservoir and the QD levels with strength v_k.

The final term in the Hamiltonian for the interaction between the conduction electrons and the QD can be written in terms of the Kondo-Hamiltonian with a antiferromagnetic coupling J as [33, 41, 42]

$$H_{int} = J s_{cond} . S_{QD}, \tag{1.30}$$

where S_{QD} is the net spin of the QD and s_{cond} is the spin operator for the conduction electrons.

The *binding energy* of the Kondo spin-singlet is expressed by the Kondo temperature, which can be written in terms of the experimental parameters of a QD device as,

$$T_K = \frac{\sqrt{\Gamma U}}{2} \exp\left(\frac{\pi \varepsilon_n(\varepsilon_n + U)}{\Gamma U}\right), \tag{1.31}$$

where ε_n is the energy of the QD state measured from the Fermi energy and Γ is the tunneling rate of electrons. This dependence of T_K is valid for $\varepsilon_n < 0$ and $\varepsilon_n + U > 0$, but as one tunes the QD level towards the degeneracy such that $\varepsilon_n \to 0$ and $\varepsilon_n + U \to 0$, the above dependence of T_K breaks down. This is the mixed valence regime, where the charge fluctuation on the resonant level becomes important.

The temperature dependence of the conductance at the Kondo-resonance is expressed by the empirical formula [43]

$$G(T) = G_0 \left(\frac{T_K'^2}{T^2 + T_K'^2}\right)^s, \tag{1.32}$$

where $T_K' = T_K/\sqrt{2^{1/s} - 1}$, G_0 is the zero temperature limit of the Kondo-conductance, $s = 0.22$ for spin-$1/2$ Kondo-effect. The Kondo temperature T_K is defined from the above formula as the characteristic temperature at which the conductance dropped to the half of its zero temperature limit G_0, i.e. $G(T_K) = G_0/2$ [35, 43].

Spectral density of a Kondo-correlated QD

The spectral densities of the QD junction were obtained by Costi et al. [35] from the numerical solution of the Anderson model. The spectral density of the QD depends mainly on three parameters, the charging energy gap U, the tunnel coupling Γ and the level position ε_n. Depending on the position of the QD levels, the spectral density of the QD for a strong coupling regime $U/\pi\Gamma >> 1$ is categorized into *symmetric* and *asymmetric* cases.
For an example lets consider $U/\pi\Gamma = 4$, then in the *symmetric case*, $\varepsilon_n/\Gamma \equiv -U/2\Gamma = -2\pi$, i.e. for a gate voltage corresponding to the middle of the Coulomb valley. The QD levels
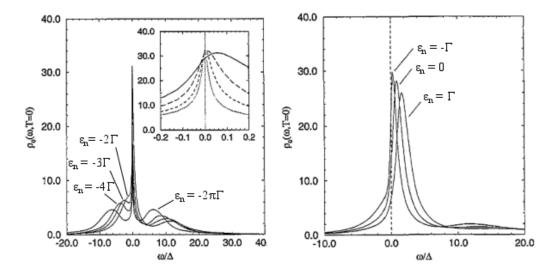
Fig. 1.8:   Spectral function of a Kondo-correlated QD   (Adapted from Costi et al. [35]) (a) spectral function of a Kondo-correlated *QD* at $T = 0$, for symmetric level position, $\varepsilon_n/\Gamma = -2\pi$ and for three asymmetric level positions $\varepsilon_n/\Gamma = -4, -3, -2$, where Kondo resonance still persists. Inset shows that Kondo resonance is pinned to the Fermi level ($\omega = 0$) for the symmetric case, while for asymmetric case Kondo-resonance is shifted slightly above Fermi energy with increasing asymmetry. (b) Spectral function at $T = 0$, for a more asymmetric case where *QD* is in the mixed valence and empty orbital regime. Here the Kondo resonance is overcome by the Coulomb-peak.

are situated symmetrically on both sides of Fermi-energy $E_F = 0$ at $\pm U/2$. In the low temperature limit, $T << T_K$, the spectral density in this case shows a Kondo-resonance of width $k_B T_K$, situated exactly at the Fermi-energy, along with the two resonance peaks at $\pm U/2$ having a width Γ, as shown in Fig. 1.9(a). The calculated spectral function is shown in Fig. 1.8 (a) with $\varepsilon_n/\Gamma = -2\pi$ [35].

For a gate voltage slightly off from the middle of the Coulomb-valley, the *QD* levels are asymmetrically placed around the Fermi energy at $\varepsilon_n > -U/2$ and $(\varepsilon_n + U)$, this is the *asymmetric case*. In this case, if the energy of the *QD* level, measured from the Fermi energy, is greater than Γ, i.e. $-\varepsilon_n/\Gamma > 1$ (for the *QD* level below the Fermi-energy, $\varepsilon_n < 0$), the Kondo-resonance is shifted slightly above the Fermi-energy, due to the influence of the closest quantum level. The spectral density for the asymmetric case is shown in Fig. 1.9(b). The calculated curves in this regime for $\varepsilon_n/\Gamma = -2, -3, -4$ are shown in Fig. 1.8 (a) [35]. On further change of the gate voltage from the mid-valley position, the *QD* level is brought closer to the Fermi-energy. For $-\varepsilon_n/\Gamma < 1$ (for the *QD* level below the Fermi-energy, $\varepsilon_n < 0$), i.e. when the *QD* level is within Γ from the Fermi energy, the charge fluctuations start to appear and the Kondo resonance vanishes with the appearance of the Coulomb peak; this is considered as the mixed valence regime. For $\varepsilon_n/\Gamma > 0$, the *QD* is considered to be in the
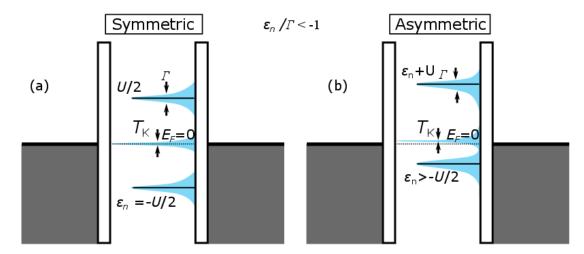
Fig. 1.9:   Spectral density of a Kondo-correlated QD junction   Spectral density of a Kondo-correlated QD at $T = 0$, in the strong coupling regime with $U/\pi\Gamma = 4$ for two cases, (a) Symmetric case, with $\varepsilon_n/\Gamma = -U/2\Gamma = -2\pi$, where the QD levels are situated symmetrically at $\pm U/2$ w.r.t the Fermi energy $E_F = 0$ and the Kondo resonance is situated exactly at $E_F = 0$. (b) for the asymmetric case, with an asymmetry in the QD level position $\varepsilon_n > -U/2$ and $\varepsilon_n < -\Gamma$, the Kondo resonance is shifted slightly above the Fermi-level within the energy window of $k_B T_K$.

empty orbital regime in this model [35]. In the mixed valence and empty orbital regime, the spectral density has two peaks, one at ε_n with a width Γ and another much broader peak at $\varepsilon_n + U$. The spectral density for a QD in this regime is shown in Fig. 1.8(b) [35].

1.2   Thermal and Thermoelectric Transport in Quantum Devices

In this section we discuss the thermal and thermoelectric transport in *SET* and *QD* junctions. The interaction between charge and heat transport is discussed by introducing the thermoelectric coefficients (Sec. 1.2.1). A pure thermal transport is considered for an SET in sequential and co-tunneling regimes (Sec. 1.2.3). Then we consider the thermal and thermoelectric transport in a *QD* junction and the effect of co-tunneling on thermoelectric transport (Sec. 1.2.4). The thermoelectric behavior of a Kondo spin-correlated *QD* junction is considered in the last part of this section (Sec. 1.2.5). In the end a qualitative comparison for the thermopower of a *QD* junction in different regimes is presented (Sec. 1.2.6).

1.2.1   Combined charge and heat transport: thermoelectricity

The transport of electrons in a conductor simultaneously carries both charge and heat currents. Therefore, the latter can not be considered as independent processes. The transport equations for these two irreversible processes near-equilibrium are in general described by the Onsager transport equations of generalized *fluxes J_i* and their conjugate *forces X_j* as [44, 45]

$$J_i = \sum_j L_{ij}X_j \tag{1.33}$$

where L_{ij} are the transport coefficients. The diagonal elements of the transport coefficient matrix, i.e. $i = j$, link the fluxes to their fundamental forces, while the off-diagonal terms with $i \neq j$ represent the generation of the fluxes due to the indirect forces. The *Onsager reciprocal relation* relates the off-diagonal terms, indicating that, in linear response regime,

$$L_{ij} = L_{ji}. \tag{1.34}$$

To use the above transport equations in thermoelectric transport, one needs to identify the proper fluxes and the corresponding forces. In thermoelectric transport, the particle current induces the fluxes of electric current **J** and heat **Q**, the corresponding forces can be identified from the equivalent transport equations of particle and energy currents [45, 46] as $\frac{1}{eT}\nabla\mu$ and $\nabla(\frac{1}{T})$, where μ is the chemical potential. Considering a parallel flow of electric current I_e and heat current I_q along the x-axis with a voltage difference $\Delta V = \Delta\mu/e$ and a temperature difference ΔT, the transport equations can be written in the matrix form as,

$$\begin{pmatrix} I_e \\ I_q \end{pmatrix} = \begin{pmatrix} L_{11} & L_{12} \\ L_{21} & L_{22} \end{pmatrix} \begin{pmatrix} \Delta V/T \\ \Delta T/T^2 \end{pmatrix}, \tag{1.35}$$

where the matrix on the left hand side of the equation indicates the scalar form of the thermodynamic fluxes and the right hand column matrix represents the thermodynamic forces involved in the thermoelectric transport. The elements of the square matrix on the right side gives the transport coefficients, which can be expressed in terms of the experimentally measurable variables.

The electrical conductance G is defined as the charge current per unit voltage difference for an isothermal system,

$$G = \left(\frac{I_e}{\Delta V}\right)_{\Delta T=0} = \frac{L_{11}}{T}. \tag{1.36}$$

The thermal conductance κ is defined as the heat current per unit temperature gradient for zero charge current,

$$\kappa = \left(\frac{I_q}{\Delta T} \right)_{I_e = 0} = \frac{1}{T^2} \left(L_{22} - \frac{L_{12} L_{21}}{L_{11}} \right). \tag{1.37}$$

The first off-diagonal element, L_{12} comes from the *Seebeck effect*, the generation of an electrical potential difference due to a temperature gradient between the two ends of a conductor. The thermopower or the Seebeck coefficient S is defined as the opposite of the generated potential difference per unit temperature gradient,

$$S = -\frac{\Delta V}{\Delta T} = \frac{1}{T} \frac{L_{12}}{L_{11}}. \tag{1.38}$$

In equilibrium, the electrical energy required to transfer an electron from the hot side to the cold side compensates the thermal energy. Therefore, the thermopower S is essentially the measure of entropy flux per transported charge.

The other off-diagonal term L_{21} is related to the generation of a temperature gradient between two ends of a conductor due to the applied potential difference, known as *Peltier effect*. The Peltier coefficient is defined as,

$$\Pi = \frac{L_{21}}{L_{11}} = -\frac{\langle \varepsilon \rangle}{e}. \tag{1.39}$$

The Onsager reciprocal relation then gives the relation between Π and S as, $\Pi = ST$.

The Wiedemann-Franz law relates the electrical conductance to the thermal conductance. It dictates that for any metal the thermal conductance κ is proportional to its electrical conductance G and the absolute temperature T [47, 48],

$$\kappa = L_0 G T, \tag{1.40}$$

where $L_0 = \pi^2 k_B^2 / 3 e^2$ is the Lorenz number. This law is valid for most of the systems where one can safely assume that both charge and heat transport undergo the same scattering mechanism. However, a strong deviation from this law is expected for a system where the scattering mechanisms for charge and heat are affected by interactions, for example in a VO_2 nano-wires near a metal-insulator transition [49].

The Mott's law relates the thermopower S to the energy dependent electrical conductivity G as [50, 47],

$$S = -e L_0 T \left[\frac{\partial ln(G(E))}{\partial E} \right]_{E = E_F}, \tag{1.41}$$

which is valid for classical systems with $E_F >> k_B T$. The sign and magnitude of thermopower then depends on the density of states of the system near Fermi energy. Bulk materials with strongly varying density of states near Fermi energy exhibit large thermopower and they are considered as good thermoelectric materials.

1.2.2 A heat engine

We introduce here the general ideas of a heat engine and the relevant quantities. A thermoelectric system operates as an engine converting heat into electrical work (the opposite one is a refrigerator), which can be used for extracting some useful work. The efficiency of the engine for converting heat into work is defined by the ratio of the power generated by the engine P_{out} to the heat input H_{in} from the hot reservoir,

$$\eta = \frac{P_{out}}{H_{in}}. \tag{1.42}$$

Since one cannot generate work directly from a heat reservoir, an engine works between two reservoirs kept at two different temperatures.

According to the second law of thermodynamics, all natural processes are irreversible and hence the maximum achievable efficiency η of a realistic engine is always less than the efficiency η_c of a *reversible* Carnot engine operating between a hot reservoir at temperature T_h and a cold reservoir at a temperature T_c [46],

$$\eta_c = \left(1 - \frac{T_c}{T_h}\right). \tag{1.43}$$

Therefore the maximum efficiency $\eta_c < 1$.

Since a reversible process is always carried out quasi-statically, the Carnot engine in principle takes an infinite time to complete a cycle, with no change in entropy. The output power of the Carnot engine therefore is zero and it is not very useful for practical purpose. Instead, a common practice is to optimize the efficiency of the engine at maximum power. Therefore a more realistic limit for the efficiency of a heat engine is given by Curzon-Ahlborn efficiency η_{CA} [51],

$$\eta_{CA} = \left(1 - \sqrt{\frac{T_c}{T_h}}\right). \tag{1.44}$$

The efficiency of an engine can also be expressed in terms of a dimensionless quantity, called the *figure of merit*, ZT, defined as

$$ZT = \frac{L_{12}L_{21}}{L_{11}L_{22} - L_{12}L_{21}} = \frac{GS^2T}{\kappa}, \tag{1.45}$$

using the relations between the transport coefficients and the experimentally measurable variables, Eq. (1.36)-(1.38). The thermal conductance $\kappa = \kappa_e + \kappa_{ph}$ contains the contribution from both electrons and phonons. The coefficient ZT can be interpreted as the ratio of the rate of work done by the engine ($G\Delta V^2$) and the direct heat flow through the system ($\kappa\Delta T$). The efficiency η can be written in the form of the ZT factor and the maximum efficiency η_c in the following way [1],

$$\eta = \eta_c \frac{\sqrt{ZT+1}-1}{\sqrt{ZT+1}+1}. \tag{1.46}$$

So that for a high efficiency one needs to achieve a high ZT factor. The goal for any heat engine is to improve the ZT factor. This can be done by improving the power factor $Q = GS^2$, while at the same time reducing κ. But in reality these two are interrelated (Eq. (1.40)), hence the main challenge for an efficient thermoelectric engine is to separate the heat and charge transport channels and to reduce the phonon contribution of thermal conductance. There is no theoretical limit on ZT factor, it is infinite for a Carnot engine. An engine with $ZT \sim 1$ is considered to be highly efficient. To the date, $ZT = 2.5$ is the record maximum value of the ZT factor, obtained in *SnSe* crystals [52].

1.2.3 Thermal transport in SET

Before going to the heat transport in an *SET*, let us first consider the heat flow in a single tunnel junction. Extending the theory in Sec. 1.1.1 for charge tunneling in a single tunnel junction between two electronic reservoirs labeled by 1 and 2, the average heat current by tunneling can be determined from the tunnel rates. The average rate of heat generated in the reservoir 1 for the tunneling from 1 to 2 is given by the average energy carried by each electron with tunnel rate $\Gamma_{1\to2}$ as,

$$\dot{Q}^1_{1\to2}(\Delta E) \approx \frac{1}{e^2 R_T} \int d\varepsilon\, \varepsilon n_1(\varepsilon) n_2(\varepsilon - \Delta E) f_1(\varepsilon)[1 - f_2(\varepsilon - \Delta E)], \tag{1.47}$$

and similarly for the backward tunneling from 2 to 1 with tunnel rate $\Gamma_{2\to1}$, the average rate of heat generated in reservoir 1 is,

$$\dot{Q}^1_{2\to1}(\Delta E) \approx \frac{1}{e^2 R_T} \int d\varepsilon\, \varepsilon n_1(\varepsilon) n_2(\varepsilon - \Delta E) f_2(\varepsilon - \Delta E)[1 - f_1(\varepsilon)]. \tag{1.48}$$

Note that there is an extra *energy* term in the Eq. (1.47) and (1.48) compared to the tunnel rate equations in Eq. (1.4), coming from the energy of the electron tunneling in or out from the reservoir. The total heat generated in the reservoir 1 is

$$\dot{Q}^1 = \left(\dot{Q}^1_{1\to2} - \dot{Q}^1_{2\to1}\right). \tag{1.49}$$

For an *SET*, the rates of heat flow in and out, $\dot{Q}^{\pm}_{i,n}$ for the leads 1, 2 and $\dot{Q}^{I\pm}_{i,n}$ for the island *I*, in the forward (+) and backward (-) tunneling processes are indicated in Fig. 1.1. Following the similar formalism as in a single tunnel junction, these heat fluxes in the *SET* leads and the island can be determined from the corresponding tunnel rates $\Gamma^{\pm}_{i,n}$, described in Sec. 1.1.2. The heat fluxes in and out of the *SET* island are respectively given by,

$$\dot{Q}^{I+}_{i,n} = \frac{1}{e^2 R_{T,i}} \int d\varepsilon \left(\varepsilon - \Delta E^+_{i,n}\right) n_i(\varepsilon) f_i(\varepsilon)[1 - f_I(\varepsilon - \Delta E^+_{i,n})], \tag{1.50}$$

and

$$\dot{Q}^{I-}_{i,n} = \frac{1}{e^2 R_{T,i}} \int d\varepsilon \, \varepsilon \, n_i(\varepsilon - \Delta E^-_{i,n}) f_I(\varepsilon)[1 - f_i(\varepsilon - \Delta E^-_{i,n})], \tag{1.51}$$

where $\Delta E^{\pm}_{i,n}$ is the energy cost of tunneling given by Eq. (1.9). These two heat flow equations represent the average heat produced and evacuated from the island by the tunneling of electrons from the *i*th lead respectively. In the same manner, the heat power produced or evacuated in the *SET* leads are given by,

$$\dot{Q}^+_{i,n} = \frac{1}{e^2 R_{T,i}} \int d\varepsilon \, \varepsilon \, n_i(\varepsilon) f_i(\varepsilon)[1 - f_I(\varepsilon - \delta E^+_{i,n})], \tag{1.52}$$

and

$$\dot{Q}^-_{i,n} = \frac{1}{e^2 R_{T,i}} \int d\varepsilon \left(\varepsilon - \delta E^+_{i,n}\right) n_i(\varepsilon - \delta E^-_{i,n}) f_I(\varepsilon)[1 - f_i(\varepsilon - \delta E^-_{i,n})]. \tag{1.53}$$

The net power extracted from the island due to all single charge tunneling processes in the junction *i* is given by,

$$\dot{Q}^I_i = \sum_{n=-\infty}^{\infty} p(n) \left(\dot{Q}^{I-}_{i,n} - \dot{Q}^{I+}_{i,n}\right), \tag{1.54}$$

and similarly, the heating power injected into the lead *i* is,

$$\dot{Q}_i = \sum_{n=-\infty}^{\infty} p(n) \left(\dot{Q}^-_{i,n} - \dot{Q}^+_{i,n}\right). \tag{1.55}$$

In the absence of net electric current though the *SET*, $\dot{Q}_i = \dot{Q}^I_i$.

Thermoelectric coefficients for SET

Similar to the electrical conductance of an *SET*, the thermal conductances is also gate voltage dependent. The ratio between the two conductances gives the Lorentz ratio, L/L_0, where L_0 is the Lorenz number. According to Wiedemann-Franz law, the Lorenz ratio is 1. For the transport in an *SET*, scattering of the electrons is energy dependent due to the strong Coulomb interaction and as a result the Lorenz ratio becomes gate voltage dependent. The thermoelectric coefficients for an *SET* have been calculated by Kubala et al. [13] using a perturbation expansion of the spectral density in the tunnel conductance of the system.
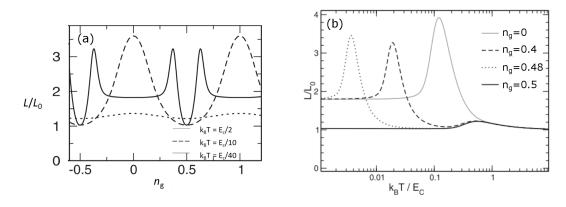
Fig. 1.10: gate voltage and temperature dependence of Lorentz ratio for an SET (Adapted from Kubala et al. [13]) (a) Calculated Lorentz ratio for an SET as function of gate voltage at different fixed temperature (b) Temperature dependence of the Lorentz ratio for different gate positions. The tunnel coupling is taken as $\alpha_0 = R_q/R_T = 0.01$, where $R_q = h/4\pi^2 e^2$, R_T is the tunnel resistance.

In the sequential tunneling regime, i.e. for the charging energy, $E_c > k_BT$ and $k_BT >> \Delta_N$, the Lorentz ratio is given by,

$$\frac{L}{L_0} = 1 + \frac{\Delta_N^2}{4\pi^2 k_B^2 T^2}, \qquad (1.56)$$

where $\Delta_N = E_c[1 + 2(N - n_g)]$ is the charging energy gap for the *N*th charge state, which can be controlled by an external gate voltage. From Eq. (1.56) we can see that, for half integer values of the gate induced charge $n_g = C_g V_g$, the charging energy gap Δ_N vanishes and $L = L_0$. Therefore for the charge degeneracy points (half integer value of n_g), where the transport involves only two charge states, the electron scattering mechanism remains unaffected and as a result the Wiedemann-Franz law is satisfied. But as we move away from the charge degeneracy point, the Lorenz ratio increases quadratically with Δ_N and becomes maximum at the charge off-degeneracy point (integer value of n_g). This is because, away from the degeneracy point, the presence of a finite charging energy gap Δ_N allows only those electrons which have enough energy to cross the charging energy barrier and therefore a

successfully tunneled electron carries an extra energy compared to what it is expected to carry in the absence of charging energy. This increases the Lorentz ratio away from charge degeneracy point, causing a violation of the Wiedemann-Franz law. The evolution of the Lorenz ratio with the gate induced charge in this regime is shown in Fig. 1.10(a), indicated by a dashed line for $k_B T = E_c/10$.

In the high temperature regime, $k_B T >> E_c$, the Coulomb oscillations are washed out. The gate voltage dependence of Lorenz ratio is shown in Fig. 1.10(a) by a dotted line for a temperature $k_B T = E_c/2$. The Lorenz ratio in this regime is only slightly grater than 1.

Fig. 1.10(b) shows the temperature dependence of the Lorenz ratio for different gate positions. The curves again confirm that the Lorenz ratio is slightly above 1 for high temperature regime ($k_B T >> E_c$) and increases to a certain maximum value, depending on the gate position, for a temperature $k_B T < E_c$.

Sequential transport is suppressed exponentially with lowering the temperature, as one goes away from the degeneracy. In the low temperature regime, $k_B T << \Delta_N$, at off degeneracy, higher order co-tunneling processes become the dominant transport process. This involves multi-electron processes via virtual tunneling (see Sec. 1.1.4). In this regime, the scattering is weakly dependent on energy and as a result the Lorenz ratio decreases and reaches a constant value

$$\frac{L}{L_0} = \frac{9}{5}. \tag{1.57}$$

The evolution of the Lorenz ratio with gate voltage in this regime is shown in Fig. 1.10 by the solid line for $k_B T = E_c/40$.

1.2.4   Thermoelectric transport in QD

The discussion in Sec. 1.2.1 indicates that a good thermoelectric material needs a strongly varying spectral function near Fermi energy. The discreteness in the energy spectrum of a *QD* can provide a strongly asymmetric spectral density around the Fermi energy of the system and hence can produce a strong thermoelectric signal. The electrical conductance of a *QD* junction was already discussed in Sec. 1.1.3, here we will discuss the thermopower in a *QD* junction.

Thermopower of a QD

Apart from the electrical conductance (G), the thermopower can be used as a spectroscopic tool in a *QD* junction which can give an information about the average energy transfer by the transport electrons, to which electrical conductance has no access.

The electric current produced in a *QD* junction, in the presence of a voltage bias ΔV and a thermal gradient ΔT across it, is contributed by electric and thermal origin and can be written by Eq. (1.35) as

$$I = G\frac{\Delta V}{T} + G_T\frac{\Delta T}{T^2}, \tag{1.58}$$

where $G_T \equiv L_{12}$, the thermoelectric coefficient that describes the current response to temperature difference. In Chapter 5 we will see that, the measurement of this *thermocurrent* gives a direct measurement of the thermopower S of the *QD*. This was defined above (Sec 1.2.1) as the voltage gradient generated per unit temperature gradient for zero current response. It can be understood as the external voltage bias that is required in order to compensate the thermally originated voltage (called thermovoltage V_{Th}) per unit temperature bias ΔT, for a zero current response. Therefore the thermopower can be written from Eq. (1.58) with the condition $I = 0$ as,

$$S = -\left[\frac{\Delta V}{\Delta T}\right]_{I=0} = \frac{1}{T}\frac{G_T}{G} = -\frac{\langle\varepsilon\rangle}{eT}, \tag{1.59}$$

where G_T/G is the Peltier coefficient Π of the device. The last term in the above equation follows from Eq. (1.39) and $\langle\varepsilon\rangle$ is the average energy carried by the electrons.

The thermopower for a *QD* in the linear response regime considering $\hbar(\Gamma^l + \Gamma^r) << k_BT$ has been presented by Beenakker et al. [7], both in the *classical-limit* with $k_BT >> \delta E$ and in the low temperature *quantum-limit* with $k_BT << \delta E$, where δE is the level spacing of the *QD*. It is also assumed for simplicity that the tunneling rates are energy independent. The resulting thermopower from this theory, in the *classical-limit* is given by,

$$S_{cl}^{seq} = -\frac{\Delta_{min}}{2eT}, \tag{1.60}$$

where $\Delta_{min} = \mu(N_{min})$ is the minimum energy to add an extra electron to the *QD* as defined by Eq. (1.17). The thermopower in this regime can be interpreted in terms of the average energy carried by the electrons, using Eq. (1.59). According to Eq. (1.60), in the zero temperature limit, the thermopower S has a sawtooth line-shape around zero as a function of the energy of the *QD*, tuned by the gate voltage. The period of sawtooth oscillation is the same as the Coulomb oscillations in electrical conductance. The behavior of the thermopower oscillation is shown in Fig. 1.11. One can notice that S crosses zero twice in a same period, once abruptly at the middle of the Coulomb valley (charge off-degeneracy) and a second time smoothly at the charge degeneracy point, aligned with the Coulomb peak of electrical conductance. This can be understood from a simple picture of sequential charge tunneling. First, at the charge degeneracy point, the level of the dot is aligned with the Fermi energy of the leads and the spectral density of the *QD* possesses a symmetry around the Fermi level of
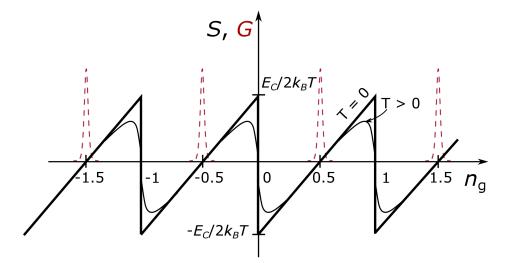
Fig. 1.11:   **Thermopower of a QD in the sequential tunneling classical limit**   The evolution of thermopower of a *QD* junction with gate voltage ($n_g = C_g V_g$), according to the linear response theory by Beenakker et al. [7] for zero temperature limit. At finite temperature the sharp sawtooth signal smears out. The Coulomb peaks of electrical conductance *G* are also shown for comparison. The thermopower is zero at each charge degeneracy point. Thermopower jumps abruptly at the center of Coulomb valley.

the leads. As a result the thermopower becomes zero due to electron-hole symmetry. Second, at the middle of the Coulomb valley i.e. at the charge off degeneracy point, two consecutive levels of the *QD* are situated above (the $(N+1)$th state) and below (the Nth state) the Fermi energy of the two leads at an equal distance of E_c. This situation also possesses a symmetry around the Fermi energy and hence the thermopower is zero again. But if one tunes the gate slightly away from the center of Coulomb-valley, the symmetry is broken and one of the contribution (either electron or hole) dominates with an average energy $E_c/2$. Therefore, being slightly off from the center of Coulomb-valley on either side causes a maximum of the thermopower at $T = 0$, $S_{max} = \pm E_c/2eT = \pm\frac{e}{4CT}$, using Eq. (1.60). As we go away from the center of the Coulomb-valley, the thermopower increases linearly with the energy of the dot, with a slope $1/2eT$. It crosses zero at degeneracy and continues to increase until the middle of the next Coulomb-valley before falling back to zero at the charge off degeneracy point. Therefore, at $T = 0$, the peak-peak amplitude of this oscillation is equal to E_c/k_BT in units of k_B/e and the period of the oscillation is $2E_c$. However, the sharp sawtooth signal becomes rounded at finite temperature [53, 54].

In the *quantum-limit*, $k_BT \ll \delta E$, the general picture is basically the same but the discreteness of the energy spectrum of the *QD* introduces more fine-structure in the sawtooth line shape of the thermopower. The thermopower in this regime is given by [7],
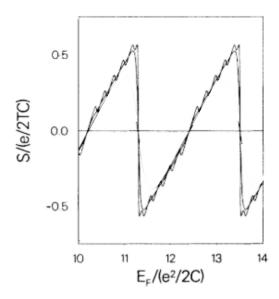
Fig. 1.12: Thermopower of a QD in the sequential tunneling quantum limit (Adapted from Beenakker et al. [7]) The evolution of thermopower of a *QD* junction with the energy, in the quantum limit $\delta E >> k_B T$, according to the linear response theory by Beenakker et al. [7]. The thermopower has two periods of oscillation; longer period is $(2E_c + \delta E)$ and the shorter one is δE.

$$S_q^{seq} = -\frac{1}{eT}\left[-\frac{\delta E}{2}Int\left(\frac{\Delta_{min}}{\delta E}\right) + \Delta_{min}\right]. \tag{1.61}$$

According to the above equation, the thermopower oscillates with the energy of the *QD* with two different periods. The long-period of the oscillations is due to the changes in the number of electrons in the ground state of the *QD*, with a period of $(2E_c + \delta E)$, equal to the period of Coulomb oscillation in electrical conductance. The shorter period of oscillations is due to the excited state of the *QD*, with a periodicity δE, equal to the energy spacing between the ground and excited states.

Effect of co-tunneling on the thermopower of QD

Although the linear response theory of thermopower of a *QD* [7] predicted a peak-peak amplitude of the thermopower oscillation to be $E_c/k_B T$ in units of k_B/e, the observed amplitude of thermopower oscillations in later experiments was found to be much smaller than that, with a modified line-shape [55–57]. This new line-shape of the thermopower is explained by the co-tunneling theory of thermopower by Turek and Matveev [9]. At very low temperatures and away from the charge degeneracy point, co-tunneling processes become dominant over sequential tunneling. This crossover temperature from the sequential tunneling

to co-tunneling is determined as,

$$T_c \simeq \frac{E_c}{ln[e^2/\hbar(G_l + G_r)]},$$

(1.62)

where G_l, G_r are the conductance of the left and right tunnel barrier. Therefore, for a temperature $T < T_c$, the contribution of co-tunneling to the thermopower becomes dominant. The co-tunneling contribution of the thermopower at a gate voltage away from the charge
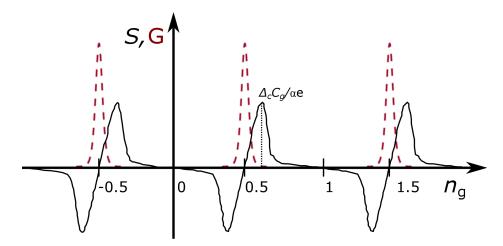
Fig. 1.13:   Co-tunneling thermopower of a QD   The evolution of thermopower of a *QD* junction with gate voltage ($n_g = C_g V_g/e$), including the co-tunneling contribution of thermopower, according to the co-tunneling theory by Turek et al. [9]. Coulomb peaks of electrical conductance *G* are also shown for comparison. The slope of the new sawtooth is opposite to linear response line-shape of Fig. 1.11. The abrupt part of the thermopower signal is now aligned with the Coulomb-peaks of conductance. Thermopower become vanishingly small in the co-tunneling regime.

degeneracy point, considering $\Delta_{min} >> k_B T$, is given by [9]

$$S^{co} = -\frac{4\pi^2}{5}\frac{T}{e}\left(\frac{1}{\Delta_{min}} + \frac{1}{\Delta_{min} - 2E_c}\right).$$

(1.63)

The above expression of thermopower is valid for the energy of the dot above the crossover energy (where co-tunneling dominates), otherwise it diverges as $\Delta_{min} \to 0$ near charge degeneracy. The crossover energy is given by,

$$\Delta_c \simeq \frac{k_B T}{e} ln\left[\frac{e^2}{\hbar(G_l + G_r)}\right].$$

(1.64)

In the weak coupling limit $G_l, G_r \ll e^2/\hbar$, the crossover energy $\Delta_c > k_B T$, i.e. the crossover from the sequential to co-tunneling regime occurs at an energy larger than the thermal width

of the conductance peak (typically within $10k_\text{B}T$) where the conductance is much smaller than its peak value.

Therefore, to get the full picture of the thermopower of a *QD* at very low temperature, one needs to consider sequential tunneling contribution of thermopower for a gate voltage $n_\text{g} < C_\text{g}\Delta_c/\alpha e$ and the co-tunneling contribution for $n_\text{g} > C_\text{g}\Delta_c/\alpha e$. This crossover energy then determines the maximum of the thermopower oscillation using Eq. (1.59) as,

$$S^{co}_{max} \sim \frac{1}{e} ln \left[\frac{e^2}{\hbar(G_l + G_r)} \right].$$
(1.65)

The behavior of the resulting line-shape of the thermopower is shown in Fig. 1.13. One can notice that the most abrupt part of the thermopower signal is now situated at the charge degeneracy points. Below the crossover energy, where sequential tunneling dominates, thermopower increases linearly with a slope $1/eT$. Co-tunneling processes above the crossover energy suppress the thermopower and make it vanishingly small in the blockade region.

1.2.5   Spin-correlated thermoelectric transport in QD junction

The electrical conductance and the spectral density of a *QD* in the Kondo spin-correlated regime is discussed in Sec. 1.1.5. In this section we will discuss the thermopower signal of a *QD* junction in the presence of Kondo-correlation and its temperature dependence. Solving the Anderson model for a *QD* with strong correlation in the framework of *NRG* method, the line shape of the thermopower and its temperature dependence was presented by Costi et al. [35, 36].

The thermopower is determined by the first moment of the spectral function A(ω, T) at the Fermi energy as [35],

$$S(T) = -\frac{\pi^2 k_\text{B}^2}{3e} T \frac{1}{A(0,T)} \left(\frac{\partial A}{\partial \omega} \right)_{\omega=0}.$$
(1.66)

The line-shape for the Kondo-correlated thermopower as a function of dimensionless gate voltage $V_\text{g} - V_{g,0}$, at two temperatures, below and above the Kondo temperature are shown in Fig. 1.14 (a), where $V_{g,0}$ corresponds to the middle of the Coulomb valley.

From the discussion of the spectral density of a Kondo-correlated *QD* in Sec. 1.1.5, we found that in the low temperature limit $T << T_\text{K}$, the Kondo-resonance is pinned to the Fermi level for a symmetric levels' position with respect to the Fermi-energy. As a result, the spectral function possesses a symmetry with respect to the Fermi level (Fig. 1.9 (a) with $\varepsilon_n = -U/2$). This is the situation for $V_\text{g} - V_{g,0} = 0$ in Fig. 1.14 (a), i.e. at the middle of the
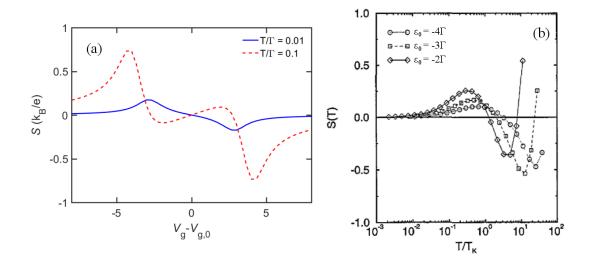
Fig. 1.14:   Thermopower of a Kondo-correlated QD with gate voltage and temperature   (a) Gate voltage dependence of the thermopower of a Kondo-correlated *QD* for two different temperatures below and above the Kondo temperature T_K. The thermopower shows a $2e$ periodic behavior. In the gate voltage regime where Kondo-resonance persists, shown by the dashed lines, the thermopower shows an opposite sign between the two curves. (Adapted from [58]). (b) Temperature dependence of the thermopower of a Kondo-correlated *QD* for different level positions in the Kondo regime. (Adapted from [35]).

Coulomb valley. Therefore the first moments of the spectral function below and above the Fermi energy cancel each other and hence the thermopower of the *QD* is zero. This is seen in Fig. 1.14 (a) at $V_g - V_{g,0} = 0$.

In the same temperature limit ($T << T_K$), for a gate voltage slightly off from the Coulomb valley i.e. for $V_g - V_{g,0} > 0$, an asymmetry is introduced on the levels' position with respect to the Fermi energy. We have seen in Sec. 1.1.5 that in this asymmetric Kondo-regime, the Kondo resonance is shifted slightly above the Fermi energy (Fig. 1.9 (b) with $\varepsilon_n > -U/2$) and the effective slope of the spectral function becomes positive. Therefore, according to Eq. (1.66) the thermopower holds a negative sign. This is seen in Fig. 1.14 (a) at $0 < V_g - V_{g,0} < 2$ for the blue-solid curve.

On further increase of the gate voltage, one gets closer to the degeneracy point where the *QD* enters in the mixed-valance regime. From the discussion in Sec. 1.1.5 we have seen that in this regime the Kondo resonance is overcome by the Coulomb peak. Still, the resonance peak in the spectral density lies above the Fermi energy and possesses a strong asymmetry. As a result the thermopower shows a maximum negative value in this regime, as seen in Fig. 1.14 (a) at $V_g - V_{g,0} \approx 2.5$ for the blue-solid curve. For $V_g - V_{g,0} > 4$ the thermopower falls back to zero.

With the particle-hole symmetry, the thermopower for the negative gate voltages $V_g - V_{g,0} < 0$ can be obtained using $S(-V_g) = -S(V_g)$. In this way one gets the full blue-solid curve in Fig. 1.14 (a) for $T = 0.01\Gamma < T_K$.

When one further extends the gate voltage into the evenly occupied diamond (e.g. $V_g - V_{g,0} > 8$, not shown in Fig. 1.14 (a)), the thermopower remains zero until the next degeneracy point (due to the non-existence of the Kondo-resonance in the even diamond), where it again shows a maximum but with an opposite sign compared the one at $V_g - V_{g,0} \approx 2.5$. Therefore, the thermopower signal in a Kondo-correlated QD possesses a period of $2e$ (in the unit of gate induced charge n_g), two times the period of the thermopower in the sequential and co-tunneling regimes.

Temperature dependence of thermopower in Kondo regime

The temperature dependence of the spectral density of a Kondo-correlated QD causes a temperature dependent thermopower in the Kondo-regime.

As discussed above, for $T << T_K$, the Kondo-resonance in the asymmetric-Kondo regime (i.e. $0 < V_g - V_{g,0} < 2$ in Fig. 1.14 (a)) is situated slightly above Fermi energy. As a consequence one obtains a negative thermopower, blue-solid curve in Fig. 1.14 (a).

Due to the strong temperature dependence of the Kondo-correlation, the Kondo-resonance starts to smear out with the increase of temperature. As a result, in the same regime (i.e. $0 < V_g - V_{g,0} < 2$), the slope of the spectral function reduces when the temperature increases and so the thermopower. The Kondo resonance vanishes almost completely above a temperature $T \approx 10 T_K$ and the spectral weight is shifted towards the nearest level. Therefore, at the same gate voltage ($0 < V_g - V_{g,0} < 2$), the slope of the spectral function becomes negative and as a consequence the thermopower becomes positive. This can be seen in Fig. 1.14 (a) for the red-dashed curve for $T = 0.1\Gamma$, having a positive thermopower at $0 < V_g - V_{g,0} < 2$.

Hence, the thermopower in the asymmetric Kondo-regime ($0 < V_g - V_{g,0} < 2$) shows a clear sign change between the two curves, below (blue-solid curve at $T = 0.01\Gamma$) and above (red-dashed curve at $T = 0.1\Gamma$) the Kondo temperature [58].

However, for the gate voltage $V_g - V_{g,0} > 2.5$, where the QD is in the mixed-valance regime, the resonance peak in the spectral density above the Fermi level does not disappear with increasing temperature, but rather it is broadened at a temperature $T > \Gamma$. Therefore the thermopower does not change sign in this regime. This is seen in Fig. 1.14 (a) with a same sign for both of the curve. The thermopower in this regime shows a large signal at high temperature due to the broadening of the resonance peak with increasing temperature.

The temperature dependence of the thermopower in the asymmetric-Kondo regime for different level of asymmetry in *QD*-level position is shown in Fig. 1.14 (b).

Therefore, this characteristic sign change of the thermopower in the Kondo regime can be considered as a "smoking-gun" signature of Kondo-effect in a *QD* system.

1.2.6 Qualitative comparison of Thermopower in different tunneling regimes

Here we compare the evolution of the thermopower signal with the position of gate for the
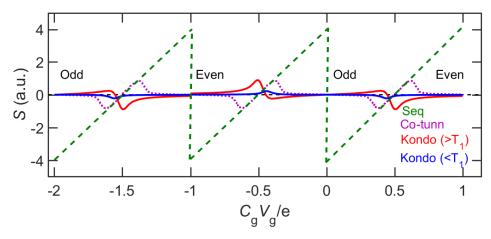
Fig. 1.15: **Gate voltage dependence of thermopower of a QD in different tunneling regimes** Qualitative comparison of the thermopower of a *QD* in three different regimes described in the previous sections. In the sequential tunneling regime (green-dashed), the sawtooth line-shape of the thermopower is presented according to theory of Beenakker et al. [7], with a periodicity of electron charge *e*. In the co-tunneling regime (magenta-dashed), the periodicity of the thermopower remains same, *e*, but the line-shape is modified, according to co-tunneling theory by Turek et al. [9]. In the presence of Kondo spin-correlation (red and blue) however the periodicity of the thermopower changes to 2*e*, with a same sign corresponding to the even or odd sector, according to the theory by Costi et al. [58].

three different tunneling regimes as discussed in the previous sections.

In the *sequential-tunneling regime*, the thermopower shows a sawtooth behavior [7], jumping abruptly at the off-degeneracy between the maximum amplitude of $\pm E_c/k_B T$. In between the two off-degeneracy points, it increases linearly with the slope $1/eT$, crossing zero at the charge degeneracy. The periodicity of this sawtooth oscillation is equal to electron charge *e* on the n_g axis as shown in Fig. 1.15 (Green-dashed line).

In the *co-tunneling regime*, the sawtooth shape of the thermopower signal is modified by the co-tunneling processes[9]. The combined line-shape of the thermopower signal in this

regime is shown in Fig. 1.15 (magenta-dashed line). Close to the degeneracy, thermopower increases linearly with the slope $1/eT$, crossing through zero at the degeneracy. While away from the degeneracy, where co-tunneling becomes the dominant transport process, the thermopower decreases with the distance from the degeneracy point and becomes zero again at off-degeneracy. The periodicity of the resulting thermopower signal is e, the same as in the sequential tunneling regime.

In the *Kondo-correlated regime*, however, the thermopower signal is fully modified by the presence of Kondo-correlation [58]. At very low temperature ($T < T_K$), a finite thermopower is observed in the oddly occupied Coulomb diamonds, due to the existence of the Kondo-resonance. The resulting line-shape of the thermopower in this regime is shown in Fig. 1.15 (blue). The thermopower changes sign between two consecutive charge-degeneracy points. The periodicity of the thermopower signal is $2e$, twice the periodicity in the sequential and co-tunneling regimes. Interestingly, with the increase of temperature ($T > T_1 \sim T_K$), the thermopower in this regime changes sign w.r.t the low temperature curve, recovering the $1e$ periodicity. The resulting thermopower signal is shown in Fig. 1.15 (red).

Therefore, like the electrical conductance G, the thermopower S can also be used a spectroscopic tool to understand transport mechanisms in QD junctions.

Chapter 2

Fabrication

In this chapter we will discuss the fabrication processes of the samples used for the two main types of experiment described in this thesis. We first considered the fabrication of a Single-Electron Transistor (*SET*), integrated with on chip local thermometer and heater (and cooler) for the measurements of thermal-conductance of an *SET* (Chapter 4). In the following section we describe the fabrication of a single-Quantum-Dot junction with local heater and thermometer, for the experiments of thermal and thermoelectric transport in a *QD* junction (Chapter 5). We have frequently used the well known 'Laser lithography' and 'Electro-beam lithography' techniques, the details of the technique can be found elsewhere [59–61].

2.1 Fabrication of NININ Single-Electron Transistor

The fabrication of device for the measurement of thermal conductance of a Single Electron Transistor consists of several steps, including, ground plane fabrication, metallic mask coating and the fabrication of the metallic SET with integrated Normal-Insulator-Superconductor (*NIS*) probes. The first two steps are required for the improvement of the measurement and reliably making the smallest structures on the substrate. All these steps are described below in detail.

2.1.1 Ground Plane

In an ideal Normal-Insulator-Superconductor (NIS) tunnel junction, the tunnelling current below the sub-gap Δ is expected to be zero at very low temperature, due to the presence of strong BCS energy gap in the superconductor. But in real experiments one routinely observe significant amount of leakage current deep inside the BCS gap [62–64]. This sub-gap current

reduces the performance of an NIS junction as a cooler or thermometer. In an experiment with high quality opaque tunnel junctions, Pekola et al. [65] showed that this sub-gap current appears mainly due to the photon assisted tunnelling rates of quasi-particles. To reduce this leakage current and improve the performance of an NIS junction, one has to filter out the rf noise coming from the electro-magnetic environment. One way to do this is to equip the dilution refrigerator with a measurement setup having sufficiently long lossy cables at the cold stage. Another way is to modify the sample fabrication in a way that the junction leads are capacitively coupled to the 'ground' of the measurement system, which can bypass the rf noise depending on the capacitance value. The dilution refrigerator that we have used in the experiment is equipped with approximately 1 m long Thermocoax (R) cable between the 1 K pot and the mixing chamber stages for each transport line. To improve the situation further, we introduce a metallic ground plane underneath the sample, which is capacitively coupled with the NIS junction leads.

Making the ground plane is the first step of our *SET* sample fabrication. We start with a single side polished 4" Si <100> wafer with 300 nm thermal oxide on it. The wafer is coated with an approximately 300 nm thick layer of a positive-tone e-beam resist (Allresist AR-P 6200) and then exposed the pattern of the ground plane by e-beam. After developing the exposed area, we deposit 2 nm of Ti, 30 nm of Au and again 2 nm of Ti respectively at 0° angle with respect to the source, in an e-beam evaporator. The purpose of the first Ti layer is to increase the adhesion of Au tom with the Si substrate while the final layer of Ti helps sticking the Al_2O_3 layer which will be deposited next. After lift off of the unnecessary metal by a suitable remover (Allresist AR 600-71), the wafer is coated with an approximately 50 nm thick layer of insulating Al_2O_3, grown by Atomic Layer Deposition (*ALD*) (see ALD Process). An *SEM* image of the full device on top a ground plane (white contrast) is shown in Fig. 2.1.

ALD Process

Atomic layer deposition (*ALD*) is a modern technique of depositing a thin layer of oxide in a controlled manner. The advantage of this technique is not only to deposit an arbitrary thickness of oxide, but also to be able to deposit a wide variety of oxides. The oxide produced by *ALD* is impurity less over a large area of surface. This is a multi-cycle process depending on the required thickness of the desired oxide. Each cycle of *ALD* consists of four steps, producing a roughly 1nm thick layer of oxide (depending on the precursor, for some precursor the relation between number of cycle and thickness is not linear). Fig. 2.2 shows the steps of the *ALD* process for the deposition of Al_2O_3. To begin with, the chamber of the *ALD* deposition system and different parts of it are set with a fixed temperature. A continuous
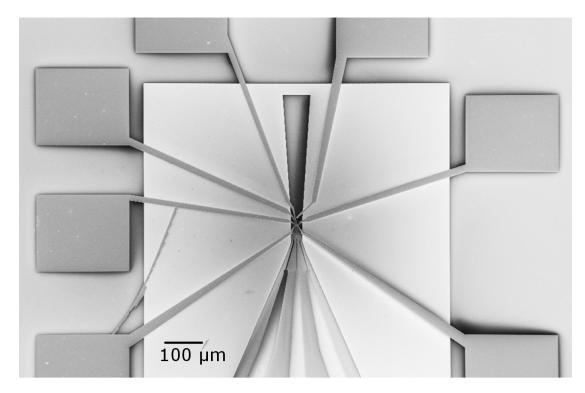
Fig. 2.1: Ground plane under the SET device Full device with a ground plane, the white contrast square region is the ground plane, all the leads are on top of the ground plane which gives a good high frequency noise filtering. The SET junction and the NIS probes are situated at the center of the ground plane.

flow of dry N_2 into the chamber of typically 5 sscm is also set in the beginning. When the temperatures of different parts are stabilized to their respective value, the first precursor (e.g. Tri-Methyl Aluminum (*TMA*) for Al_2O_3) is injected in the *ALD* chamber, we then wait for few seconds (typically 5-15 Sec depending on the particular recipe) so that the self-limiting substitution reaction of the precursor with the substrate can complete and the products can be purged out with the flow of N_2 gas. After that we inject the 2nd precursor, usually H_2O. Waiting for 5-10 sec completes the reaction and the program purges out the products from the chamber. In this way we deposit a single atomic layer of oxide (e.g. Al_2O_3) on top of the structures. We repeat the same cycle to achieve the desired amount of thickness.

2.1.2   Ge Metallic Mask

For the electron-beam lithography with simple design, soft resists like PMMA, PMMA-MAA are often used for defining the structures on the substrate. But if the design is complicated and contains many closely spaced small structures, making such pattern is difficult with a soft resist, as there is a high chance that the mask may collapse after the development. The
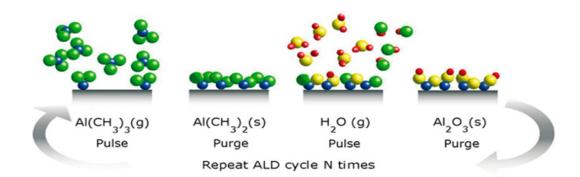
Fig. 2.2: **Steps of a single** *ALD* **cycle** (Adapted from Oxford instruments) Schematic diagram of the steps of a single layer of Al_2O_3 deposition on top a substrate using *ALD* technique. First, the precursor of Al_2O_3 TMA is injected in to the chamber, after the completion of the reaction the product is removed from the chamber with the purge of dry N_2, next the precursor H_2O is injected and in the same way products are purged out of the chamber and in this way a single layer of AL_2O_3 is deposited on top of the substrate. A single cycle produces approximately 1 nm thick AL_2O_3 layer, *N* cycles are repeated to get a *N* nm thick layer of Al_2O_3

free standing top resist is not stiff enough to hang without support. To avoid such resist collapse, we have used a metallic mask technique. Here we take the full wafer with ground plane already made on it and spin-coat it with an approximately 400 nm thick e-beam resist, namely P(MMA-MAA) copolymer (11% in ethyl lactate). Then we deposit a 22 nm thick germanium (Ge) layer inside an e-beam evaporator. This Ge layer will be used to form the metallic mask in the following step of lithography.

2.1.3   SET and NIS probes

Lithography

This is the final lithography step of the fabrication process. In this step we define the smallest structures of the device such as the NIN tunnel junctions, Source, Drain and Gate of the SET and the NIS probes of the thermometer or cooler. We first spin coat the previously processed wafer, containing the ground plane and Ge layer deposited on it, with a e-beam resist PMMA 2 %. After that we expose the pattern on that wafer by e-beam.

Development

The development process is very delicate step, we develop the exposed sample in the following way:

Table 2.1: Fabrication steps for *SET* device

#	Step description	Process	Comments
1	Ground plane	Resist coating	Allresist AR-P 6200
		E-beam exposure	100 kV, 180 nA, 350 uC/cm^2
		Development	MIBK+IPA 1:3
		Metalization	Ti(3 nm)/Au (30 nm)/Ti(3 nm) at 0°
		Lift off	Allresist AR 600-71 1 hour
		ALD	Al$_2$O$_3$ 50 nm
2	Metallic Mask	Resist coating	P(MMA-MAA) 11 % 400 nm
		Ge evaporation	22 nm at 0°
3	SET and NIS probes	Resist coating	PMMA 2 % 50 nm
		patterning	100 kV, 1 nA, 1000 uC/cm^2
		Development	MIBK+IPA 1:3, 1 min
		CF4 etching	100 sccm 40 mTorr, 40 W, 2 min 10 s
		Development	MIBK+IPA 1:3, 1 min
		Oxygen anisotropic	50 sccm, 30 mTorr, 40 W, 10 min
		Oxygen isotropic	50 sccm, 225 mTorr, 40 W, 50 min
		Metalization1	Cu (30 nm) @ 0°
		Metalization2	Al (20nm) @ 38°
		Oxidation	1-2 mbar 60- 90 s
		Metalization3	Cu (30) @ -25°
		Liftoff	Acetone 30 min

1. *wet development of top resist*: develop the top e-beam resist PMMA 2 % by rinsing it in MIBK/IPA for 30 sec followed by a rinse in a IPA bath for another 30 sec.

2. *Reactive Ion Etching (RIE) of Ge*: after the wet development of the top layer PMMA, the Ge metal underneath is etched away by anisotropic *RIE* with CF4 at 40 mTorr pressure and 40W power. In this way the pattern is now transferred to Ge layer.

3. *Wet development of lower resist*: after removing the Ge layer from the exposed area, we develop the lower thick layer of the copolymer resist by same way as in step 1. During the process of optimization, we learned that this is quite important step as it helps removing the lower layer resist and making the undercut wider already before oxygen plasma cleaning.

4. *Oxygen plasma cleaning*: the top thin layer of PMMA 2% and the developed area under Ge layer is cleaned by anisotropic RIE with oxygen at 30 mTorr, 40 W. Followed last by a more isotropic oxygen etching at 225 mTorr, 40 W. Now, as the top thin layer of PMMA is removed, the full mask is made of Ge only with a large undercut. The thickness of the top layer and limit of evaporation angle depends only on the Ge layer thickness. Metallic Ge is stiff enough to hang without support from bottom, in this way we create a large undercut without deforming the mask. This mask is now ready for metalization.

Metalization

To deposit metal on the mask, we load the sample into a multi-crucible e-beam evaporator equipped with tiltable sample stage, so that we can deposit more than one metal at different angle in the same vacuum cycle. The metal is deposited in the following steps:

1. First a 30 nm of Cu is deposited at 0° angle w.r.t the source. This initial Cu forms the SET drain lead (Green) as well as the main part of the source electrode (Red), as shown in Fig. 2.3.

2. Immediately after, we evaporate a 20 nm of Al. For this evaporation the sample holder is now rotated to an angle of 38°, resulting in an effectively 15 nm thick, downward shifted Al copy of the pattern. The Al layer forms the two, sub 200 nm long dots (Red dot on left and green dot on the right of Fig.2.3 (b)), connected to the source and drain Cu regions with transparent metal-to-metal contacts and at the same time the clean contacted lead from the end of Source electrode (shown in purple color in Fig. 2.3 (a)).
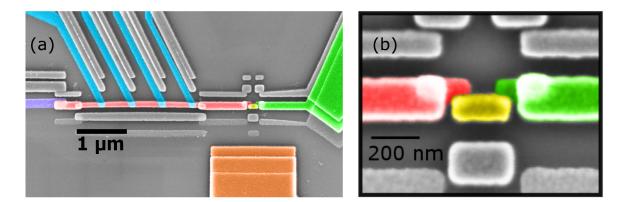
Fig. 2.3: **SEM image of the SET device** (a) Colored SEM image of the SET with different elements of the device shown in different color: the Source is shown in red, Clean-contacted Al lead at the end of source in purple, four tunnel-contacted Al leads in cyan, the Island in yellow, the Drain in Green and the Gate is shown in orange color. (b) Zoomed in view of the SET, showing two Al dots connected to the island via tunnel contact(in red and green on the left and right of the island), while on the opposite side they are connected to big metallic Cu strips, in order to destroy the SC of the Al dots

3. To form the AlO_x tunnel barrier for the SET and NIS probe tunnel juctions, the Al layer is subjected to *in-situ* static oxidation immediately after the deposition is completed. This is accomplished by injecting typically 1 - 2 mbar of oxygen into the deposition chamber for the duration of 60- 90 s.

4. To complete the fabrication, a second 30 nm layer of Cu is evaporated with the sample now tilted 25° in the opposite direction compared to preceding Al deposition. This upward-shifted copy of the mask pattern forms the SET island (Yellow in Fig. 2.3 (b)) as well as the N electrode of the NIS probes.

We lift-off the unnecessary metals by Acetone. As a result of three-angle evaporation through the mask, three projections of the complete mask pattern will be formed on the substrate. The irrelevant shadow copies of the various structures are shown uncolored in gray (Fig. 2.3). All the steps of the SET device fabrication are listed in the Table. 2.1

2.2 Fabrication of Single *QD* device

2.2.1 Gate and Contact pads

The fabrication of single QD device start with the metallic gate. In different mesoscopic experiments the gate can be implemented in different configurations depending on the sample requirements, including, side gates used for an SET, back and top gates used for gating

on nano-wire quantum dots, plunger gates used in a 2DEG QDs etc. The coupling of the island to the gate depends on the distance between them and on the relative permittivity of the dielectric medium in between them, therefore to have a good coupling we need very small distance (< 10 nm) between gate and island and a dielectric medium having relative permittivity > 1. In our device, we choose to use a metallic back gate, because this configuration of the gate allows us to have a distance between the gate and the island (Gold Nano-particles in our case) in the range of 5-8 nm. We use a metallic oxide as a dielectric medium to ensure good capacitive coupling between gate and island. Another advantage of using a back gate is that it can be easily adapted with the electro-migration (*EM*) process (a technique for controlled breaking a metallic constriction in order to create a nm-size gap, sec. 2.2.3).

In our design, the Gate is a 3 mm long and 200 μm wide rectangular structure (Fig. 2.4 (a)), with two micro-bonding pads at the two end. We have places for three devices on top of this gate, so that the same gate can be shared by three devices. The gate is made long and wide in purpose, the reason behind this particular design is that, first, we can gain one extra cryostat line by combining the gates of three devices and second, the overlap of contact leads of the device with the gate can give an efficient on-chip filtering against the *rf* noise. The contact-pads are 200x200 μm square structures (Fig. 2.4 (b)) connected with a leads near the gate. The smallest part of the *QD* device will be connected to the contact pads at the last step of fabrication. The contact-pads are used for micro-bonding the device with the cryostat sample holder pads.

The gates and contact-pads are usually very large area structures, therefore to save machine time, we first pattern them on a full wafer using laser lithography.

Laser Lithography Process

Usually one uses a single layer resist for such lithography, but in order to have a high quality gate without any defect, we use a bilayer laser lithography technique, developed at Institut Néel [66], as follows.

First we take a single side polished 2 inch Si <100> wafer with 500 nm of thermal oxide grown on it and bake it at 200° C for 4 mins. After pre-baking the wafer, we coat it with a first layer of photo-resist *LOR*3A followed by baking at 200° C for 2 mins, then we coat it with another photo-resist S1805 and bake it at 115° C for 1 min. Then the gate is patterned on the substrate by laser lithography. The exposed part is developed by rinsing the wafer in a bath of *MF*26 for 1 min followed by a bath of DI water for 1 min. This finishes the mask of the gate and makes it ready for metallization, an optical image of the gate mask after development is shown in Fig. 2.4(a).
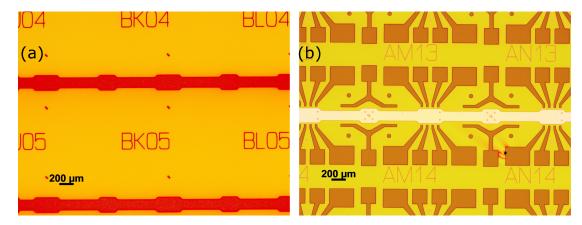
Fig. 2.4:   Optical image of the Gate and contact pad mask for QD device   (a) Gate mask after development of the first Laser-lithography exposure, additional marks and the numbers are for alignment in the next step; (b) Leads mask after development of the second Laser-lithography exposure, the Gates are already metalized here

To evaporate metal on the mask of the gate, we load the full wafer inside a e-beam evaporator and evaporate as a stack of 3 nm of Titanium (Ti), 30 nm of Gold (Au) and another 3 nm of Ti at 0° angle and at a very slow rate of 0.2 Å/ s. The first layer of Ti is used to increase the adhesion of the Si substrate with Au atoms so that it sticks well on the Si substrate, while the final layer of Ti helps sticking the oxide layer which will be grown on top of the gate electrode in the next step. The lift off of the unnecessary metal is done in two steps, first the wafer is put into a bath of Acetone for 15 minutes (Acetone can immediately dissolve the top layer of the resist S1805, but can not dissolve the bottom layer *LOR*3A), then we transfer the wafer in a bath of hot remover PG (or NMP) for 1 hour at 80° C. We finish the lift off process by rinsing the wafer with Acetone and IPA and then dry it with N2 gun.

Oxide Layer deposition

After finishing the lift off, the wafer is cleaned by Oxygen plasma using Reactive ion etching (*RIE*) for 5 mins. We now want to deposit a thin layer of oxide on top of the metallic gate structure. The oxide layer is deposited using Atomic Layer Deposition technique (*ALD*) (for the process of *ALD* see the Sec. 2.1.1). One can achieve the oxide layer on top of a metallic Aluminum (*Al*) gate by simply oxidizing the *Al* but we prefer *ALD* compared to normal oxidation technique because the oxide deposited by *ALD* is very uniform over a large area and is impurity less. This gives us a wide range for gate voltage applicability before reaching breakdown voltage. The ALD also gives us a wide variety of metallic oxide (with very high dielectric constant) to be deposited on the gate electrode. As the oxide is deposited layer by layer, the thickness of ultimate oxide layer is controllable precisely.

Table 2.2: *ALD* recipe for Al_2O_3 deposition

Fixed parameters	steps	Operation	time(s)
Precursor: Tri-Methyl Aluminium (TMA)	1	TMA injection	0.015
Precursor temperature: Room temperature	2	Wait	120
Tee temperature: 90° C	3	H_2O injection	0.015
Chamber temperature: 100° C	4	Wait	120
Bellow temperature: 150° C	5	go to step-1	

We deposit about 8 *nm* of Al_2O_3 on top of the metallic gate structure. Usually the thickness and quality of the oxide layer depends on different parameters of the *ALD* setup including, the precursor quality, temperature of different parts of the system, waiting time in between two steps, flow rate of dry N_2 gas etc. One need to optimize these parameters to get a good quality of oxide layer consistently. We use a standard recipe for the gate insulation, developed at Institut Néel [66], as described in Table 2.2.

Contact-pads

To fabricate the Contact-pads, we use the previously discussed laser lithography (Sec. 2.2.1). As the Contact-pads have to be perfectly aligned with the previously made gate, we use the small square marks made at the same step of the gate for the alignment during the patterning the contact pads. An optical image of the lead mask after development is shown in Fig. 2.4(b). It is found that the developer $MF26$ (for the photo resists $LOR3A$, $S18O5$) is corrosive for the metal oxide on top of the gate, so there should not be any overlap between contact leads and the previously made gate (otherwise one has to use different resist and developer). Therefore the alignment with the previous gate layer is very crucial. Sometimes it happened that, due to a misalignment, the contact pad patterns are exposed partially on top of the gate and as a result exposing the oxide layer on the gate to the chemicals. If this kind of misalignment occurs one has to restart the process from the beginning without proceeding further. After development, the mask of the contact-pad is metalized with Ti and Au respectively at 0° angle, at a rate of 0.2 Å/ s. After finishing the lift off with Acetone and remover PG, the wafer making process is completed.

At this stage the full 2 inch wafer contains about 100x100 arrays of gate and contact pads. In the next step we will fabricate the smallest part of the device on top of the gates, using electron-beam lithography.

2.2.2   Constriction and SNS junctions

To fabricate the smallest part of the device having dimensions < 100 *nm*, we use high energy (80 *keV*) e-beam lithography. For this we spin-coat the wafer having gate and contact pads on it, with a bi-layer e-beam resist PMMA-MAA 9% and PMMA 4%. The thickness of the bottom resist is about 750 nm while the top layer has thickness of about 250 nm. The purpose of the bi-layer resist technique is, first, to make the liftoff easier and second, to create asymmetric undercuts on the mask [67], which enables us to make shadow evaporation for creating clean contact SNS junctions without breaking the vacuum.

The design of the EM constriction and the SNS junctions are patterned on the resist. As the structures need to be properly aligned on top of the gate, we use the markers made at the step of the gate fabrication. During the course of the thesis, we iterate the sample design and improve it accordingly. The final structure of the design is discussed here.

The exposed sample is developed with a solvent *MIBK/IPA* 1 : 3. An optical image of the developed devices on top of the gate are shown in Fig. 2.5 (a), a zoomed view of a single device is shown in Fig. 2.5 (b).
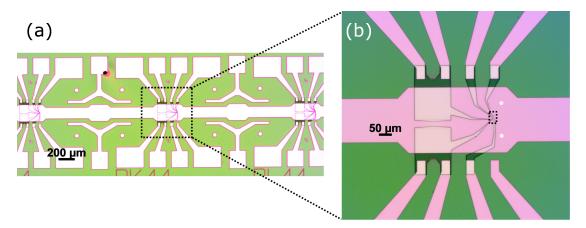
Fig. 2.5:   Optical image of the e-beam lithography made mask after development   (a) mask of three devices on top of a same gate. Two bonding pads are at the two ends of the long gate (not visible here), the mask has overlap with the leads with contact-pads made in the previous step (b) Zoomed view of the middle part of the mask, the mask has a large overlap with the gate to ensure good on-chip *rf* filtering. The rectangular section of this mask is shown in Fig. 2.6 (b) after liftoff.

Evaporation

After cleaning the developed sample by oxygen plasma we load the sample in an e-beam evaporator and deposit metals in different steps as follows,

1. First, we deposit a 11 nm of Platinum (*Pt*) at a large angle of $-42°$ with respect to the source. This creates a little 'butterfly' shaped constriction at the middle of the device (yellow colored in Fig. 2.6 (b)). As this is deposited at such a high angle, the *Pt* copy of the other parts of the device(source, drain and the Al leads) will be deposited on the wall of the resist and washed way during lift off.

2. Then we rotate the sample holder and deposit 25 nm of Gold (*Au*) at an angle of $-22°$. This creates a rectangular metallic island on the right of the constriction, which we call the 'Source' of the device and a bulky lead on the left of the constriction, the 'Drain' of the device, shown in red in Fig. 2.6 (b).

3. At the same angle we deposit a 3 nm of Titanium (*Ti*). This acts as a protective layer for *Au*, to avoid intermixing of *Au* and *Al* [68–70]. This technique improves the lifetime of the device.

4. Then we rotate the sample holder in the opposite direction and deposit a 80 nm thick Aluminum (*Al*) at an angle of $20°$ w.r.t the source. This creates the four *Al* leads (shown in light-blue color in Fig. 2.6), which are connected to the 'Source' via clean contact making four $S-N$ junctions.
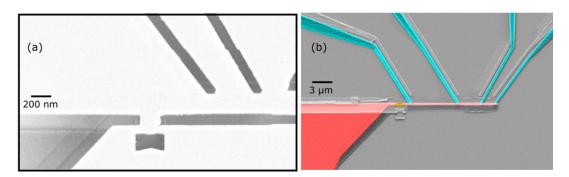
Fig. 2.6: **SEM image of the full device**   (a) Angled *SEM* image of the mask after metal evaporation and before liftoff. This part of the mask is completely hanging with the help of support from the sides, three layers of metal produced by the three angle evaporations are visible through the mask. (b) Rectangular section indicated in Fig. 2.5 (b) is shown here as a false colored *SEM* image after liftoff, showing different metals with colors: the Au made Source and Drain are shown in red, the Pt constriction in yellow and the four Al leads in light-blue. Unwanted shadows are not colored.

An *SEM* image of the evaporated sample before liftoff is shown in (Fig. 2.6 (a)).

The metal is then lifted off by a solvent N-Methyl-2-pyrrolidone (NMP) at 80° C and afterwards rinsed by Acetone, IPA and Ethanol to clean it properly and at last blow dry by nitrogen. An *SEM* image of the full device after liftoff is shown in the Fig. 2.6 (b). One can

see the 'Butterfly' shaped *Pt* constriction at the center of the device, which is connected to a rectangular shaped 'Source' on the left and a bulky drain on the right. The purpose of making the constriction out of *Pt* in a separate angle is to avoid any proximity superconductivity that may induced by the leftmost *Al* lead, on the constriction after we break it by electromigration. The *Al* leads are placed in such a way that they do not touch the 'normal-metallic' *Au* shadow of its own, before a length of about 6 μm. This is to avoid any inverse proximity effect on the *Al* leads.

This finishes the nano-fabrication the *QD* device. The lithographically made constriction will then be broken by electromigration technique, to create a nano-gap between source and drain. Subsequently, the *Au* nano-particles (*NP*) will be grafted inside the nano-gap to complete the *QD* transistor fabrication.

2.2.3 Electromigration

Electromigration (EM) is a process of creating a nano-meter sized spacing within a conductor. Under the influence of an electric field, electrons in a conductor are moving according to the direction of the applied electric field, during this movement they violently collide with the atoms. A transfer of momentum from the electrons to the atoms occurs due to the in-elastic collisions, causing a movement of the atoms and eventually breaking the metallic wire. The *EM* force can be identified as a combination of two terms, (1) the 'direct' force, proportional to the external electric field and (2) the 'electron-wind' force due to the momentum transfer from the electrons.

This process is already known for a long time as one of the major failure mode of microelectronic circuitry [71], but this failure mode was exploited for the first time to intentionally break a metallic gold nano-wire, in a controllable and self limiting way, by Park et al. [72]. In this first work, they current-biased a 15-20 nm thick metallic gold nanowire while measuring the voltage drop across it. After the completion of *EM*, they found that most of the devices have a measurable tunnel resistance, ranging from few $k\Omega$ to few tens of $G\Omega$, indicating that a gap of about 1 nm is created in the nanowire.

This brilliant application of *EM* opens up a channel to create a single molecule transistor and probe the transport properties through a single electronic nano-object [73–76]. Later, the technique was improved, by introducing an active feedback method by Strachana et al. [77] and a four-probe method to avoid the series contact-resistance [78].

In this thesis, we electromigrate the lithographically-made constriction either before (outside the cryostat) or after (*in-situ*) the deposition of gold nano-particles (*NP*). As *Pt* does not oxidize significantly at an ambient condition, one can electromigrate the lithographically made *Pt* constriction at room temperature, without having a risk of increase in tunnel
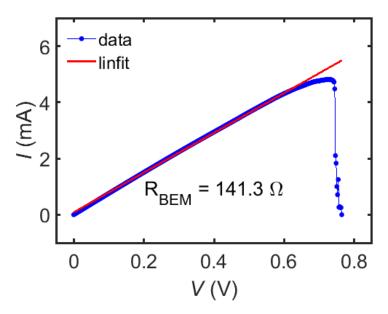
Fig. 2.7: **IV curve of a typical EM** A typical *IV* curve for an *EM* process. The resistance of the constriction before *EM* is measured to be $R_{BEM} = 141\ \Omega$. The *EM* process stops as soon as the measured conductance of the junction drops below a preset value.

resistance before low temperature investigation. Therefore we can deposit the *NP* after breaking the constriction and finally put the ready made 'QD Transistor' inside the cryostat for further measurements. The second way is to first deposit the *NP*s on the as made, unbroken constriction and put the whole sample with *NP*s inside the cryostat and electromigrate the constriction at liquid Helium temperature (4K), under high vacuum.

We found that the first method, produces sample with very weak coupling between source and drain, while the second method gives us strongly-coupled *QD* transistor. One possible explanation of this effect could be due to the contraction of the *Pt* atoms after the formation of *EM* gap at room temperature, which can continues to increase the size of the nano-gap as time goes on, while at low temperature this process becomes negligible.

For the *EM* of the constriction we apply a voltage bias across the constriction and simultaneously measure the current flowing through it. For an *in-situ EM* we apply the voltage bias from a fast measurement equipment 'Adwin Pro II' (a 16 bit data acquisition system with internal processors) and simultaneously measure the current flowing through it. Therefore, the conductance of the device is monitored by a fast feedback algorithm (developed by 'Nanospin' group in Institut Néel), with the Adwin Pro II and sets the bias back to zero as soon as the conductance drops below a preset value. The time to ramp down the bias to zero is about 10 μs, which is small enough to avoid any further *EM*.
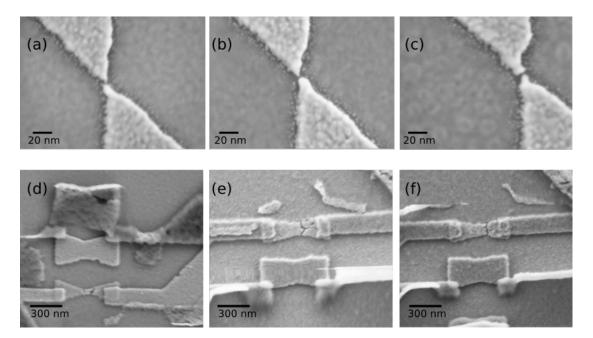
Fig. 2.8:   SEM image of the EM junctions   (a-c) *SEM* images of successful *EM* junctions, electromigrated in ambient condition and at room temperature; (e-f) *SEM* of the *EM* junctions electromigrated *in-situ* at 4*K*

EM outside the cryostat, were done at a probe station, in the same manner by voltage biasing the constriction. In this case, the conductance of the device was monitored by a Keithley 2000 multimeter. A typical *IV* curve for the *EM* process is shown in Fig. 2.7.

One advantage of doing *EM* at the probe station is that, there is no extra series resistance, except the contact resistance between the probes and the sample pads, of about 30 Ω. Therefore, most of the voltage drop is on the constriction and *EM* triggers at relatively low bias (typically below 0.4 V). This ensures less overheating and hence less chance of fusion of the leads. On the other hand, for an *in-situ EM*, we can not avoid the line resistance of the cryostat, of about 170 Ω each. Therefore, the *EM* takes place at a bias voltage > 1 V. Nevertheless, to avoid any significant over heating during *EM* process, we design the constriction in a way that it has a smallest cross section area. This allows us to reduce the current at which *EM* is triggered and hence the dissipated power. This requires the constrictions to be made as thin as possible. As we make the constriction in a separate angle, it is possible for us to make it thinner than 12 nm.

Fig. 2.8 shows the *SEM* images of few successful electromigrated junction. Top panel (a-c), shows the *EM* junctions created at the probe station at an ambient condition, while lower panel (d-f) shows the *EM* junctions made inside the cryostat.

2.2.4   Gold Nano-particle deposition

This is the last step of the *QD* device fabrication, where we trap a single *NP* between the source and drain, which serves as the 'Island' of our *QD* transistor. As mentioned before, the *NP*s can be deposited after or before the formation of nano-gap by *EM*.

We have used four different methods for depositing the *NP*s on the sample, given by,

1. Drop-casting

2. Self-assembling

3. Di-electrophoresis trapping

4. sub-monolayer evaporation of *Au*
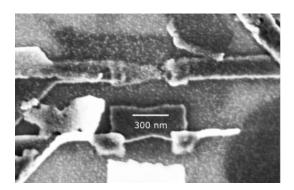
Here we describe all the methods separately.

Drop-casting:

This is one of the simplest method of *NP* deposition, here we put a drop of commercially available 5 *nm Au − NP* (from 'Nanocomposix') dispersed in Toluene and immediately dry out the dispersion solution by blowing dry N_2 on top of the sample. In this way, some of the *NP*s settle down on the substrate, while most of them are blown away with the dispersion solution. We repeat this process for $10 − 15$ times. The immediate blowing of the solution restricts the *NP*s to agglomerate with each other. The resulting density of the particles is very little as most of the *NP*s are lost in the process. Fig. 2.9 shows an SEM image of two such samples with 5 *nm Au − NP* deposited on it by this method. From the study of the process, we found that the yield of this method for a successful grafting of *NP* at the *EM* junction is about 3%.

Self-assembling of Au-NP:

Self-assembled layer of gold nano-particles on top of the *Si* substrate can be obtained by functionalizing the *Si* substrate with Salines terminated with aminopropyltriethoxysilane (APTES) [66, 79]. We have used 12 *nm Au − NP*s dispersed in a citrate solution for the silanization process. Fig. 2.10 shows the SEM image of the samples with *NP*s deposited on it by self-assembling method. The density of particles on the sample can be made higher than the *drop-cast* method, but we found that the citric acid in the dispersion medium reacts with the *Al* and destroys the sample (as can be seen in Fig. 2.10 (c, d), indicated by red arrow heads). Therefore, we did not use this method at all to deposit the *NP*s.
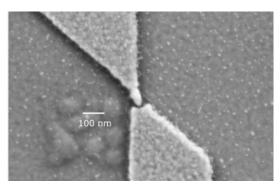
Fig. 2.9:   NPs deposited by drop-cast method   SEM image for the distribution of 5 *nm Au − NP*s deposited on top of the electromigrated junction, deposited by the drop cast method. The yield of this method for a successful *QD* device is about 3%.

Di-electrophoresis trapping:

In this method we trap the *NP*s within the *EM* created nano-gap between the *source* and *drain*, with the application of an electric field [80–85]. When an AC electric field is applied on the solution of *Au − NP*, an electric-dipole is induced on the *NP*s. According to the laws of electrodynamics, the dipoles feel an attractive electrostatic force when they are subject to a non-uniform electric field, called the di-electrophoresis (*DEP*) force. Therefore, the *Au − NP*s are attracted towards the place on the sample, where the field is most non-uniform and hence most strong *DEP* force. In this way, one can move the particles towards the *EM* junction by creating a non-uniform electric field around it.

We first electromigrate the constriction at room temperature to create a 5 − 10 *nm* gap between the *source* and *drain*. The *EM* broken junction is then wired according to the *DEP* setup, as shown in Fig. 2.11 (top), where an AC signal is applied to one end of the junction, while the other end is grounded through a 465 Ω series resistor. The voltage drop across the resistor is monitored during the process, by a Lock-In amplifier and an oscilloscope in parallel.

We have used a colloidal *NP* solution with three different diameters. For trapping the particles, we first put a drop of the *NP* solution on the sample and immediately turn on a sinusoidal signal of amplitude 1 V and frequency 100 K*Hz*. The full process of trapping takes about less than a minute. Initially, when there is not particle bridging the gap, measured voltage drop across the resistor is zero (ignoring the leakage current through the liquid of the *NP* solution) and after about few seconds to one minute a sudden jump in the voltage drop is recorded in the voltage measurement. This indicates the bridging of the nano-gap by the particles. After observing such a jump in the measured voltage we turn off the AC signal immediately and dry out the remaining solution by N_2.
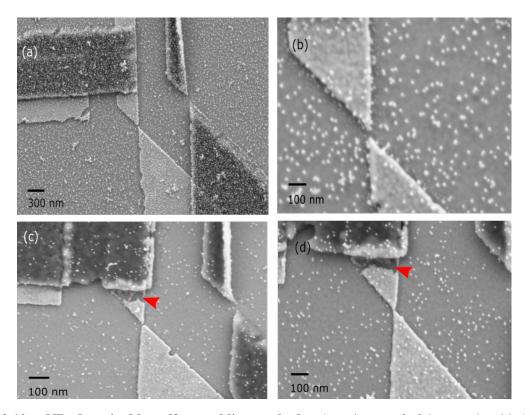
Fig. 2.10: NPs deposited by self-assembling method *SEM* image of of the sample with 12 *nm* *Au − NP*s deposited on top of the electromigrated junctions by self-assembling method. The process required the *NP*s dispersed in a citrate medium, but citric acid is found to be corrosive for the *Al*. This introduces defects at the junction of *Al* and *Au* in the device, as indicated by the red arrow-heads.

The *DEP* force, that determines the efficiency of the trapping process, depends on the radius of the particle, the effective dielectric constant of the medium and the frequency and amplitude of the AC signal. During the course of the thesis we have performed the *DEP* trapping on the *Au − NP* of three different sizes, 5, 12 and 50 *nm*.

DEP with 5 nm NPs: For the case of *DEP* trapping with a 5 nm *NP*s, the *DEP* force on the particles is found to be very little to attract them towards the junction. This could be improved with the application of higher frequency AC signal, but we did not have the possibilities to go beyond 100 K*Hz* (as we have used the internal signal of a Lock-in amplifier with a maximum frequency of 100 K*Hz*). The *SEM* images of some samples, after finishing the *DEP* process with a 5 nm *NP* solution, are shown in the Fig. 2.11, which indicates that the trapping of the 5 nm particles were not possible. Almost all the sample shows either an agglomeration of the particles due to multiple try of *DEP* on the same sample or a failure of the trapping process.

DEP with 12 nm NPs: With the increase of the particle size to about 12 nm, we found a moderate increase of *DEP* force and hence the trapping efficiency. The *SEM* images of few
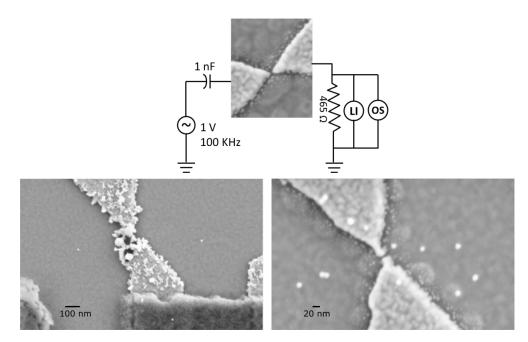
Fig. 2.11: **Deposition of 5 nm GNPs by DEP method** (Top) Circuit diagram for *DEP* process. An AC bias is applied across the electromigrated junction, with a drop of *NP* solution on it. The voltage drop is measured across an external series resister (465 Ω) using a Lock-in (LI) amplifier and an oscilloscope (OS) in parallel. (Bottom) *SEM* images of the some samples with 5nm *Au* − *NP*s deposited by *DEP* method. Instead of trapping, in most of the cases we found the agglomeration of the *NP*s at the side of the Au structures.

samples after finishing the *DEP* trapping with 12 nm *NP*s are shown in Fig. 2.12, where one can notice that the trapping of individual *NP* is possible. In some cases, the agglomeration of the particles are also found. For some other batches, a fusion of the *NP*s is observed, forming a weak *Au* nano-wire bridging the gap.

DEP with 50 nm NPs: We have also performed the *DEP* trapping with a *NP* of diameter of 50 nm. The *DEP* force is found to be substantially strong in this case. Fig. 2.13 shows the *SEM* images of few of the samples with 50 nm *NP* trapped by *DEP* process. The images indicate the successful trapping of individual *NP* between the *source* and *drain*. In some cases we found the gathering of the particles near the *EM* junction, while in some other images indicate a fusion of the individual particles forming a nano *Au*-island. This could be due to the delay in turning off the electric field after the trapping occurred.

One drawback of the *DEP* process is that the electromigrate the constriction needs to be done already before *NP* deposition, in an ambient condition. Therefore, this method is not adequate, if one has to create the nano-gap *in* − *situ*.
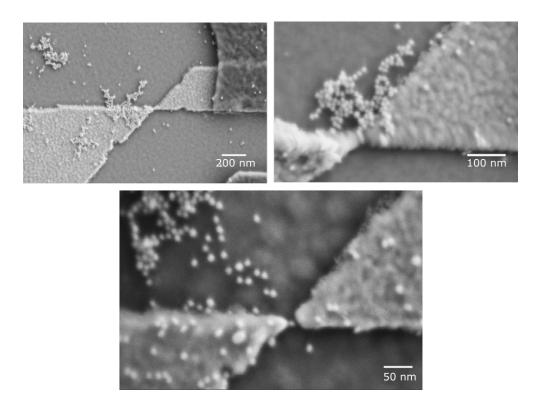
Fig. 2.12: Deposition of 12 nm GNPs by DEP method *SEM* images of few samples with 12 *nm Au − NP*s deposited by the *DEP* method. For 12 nm *Au − NP*s the trapping of *NP* is possible in some cases, in some other cases agglomeration and fusion of several particles is observed.

Sub-mono layer evaporation of *Au*:

Another method of *NP* deposition that we have performed is the evaporation of a small amount of *Au* on top of the sample inside an e-beam evaporator. This creates a sub-mono layer of *Au* in the form of small droplets on the substrate [86, 87]. We have used this method of *Au − NP* deposition for the case of both before and after the creation of *EM* gap.

For a deposition of *Au − NP* after *EM*, we first break the constriction outside the cryostat, in an ambient condition. Then clean the electromigrated sample with Acetone, IPA and ethanol and afterwards with the oxygen plasma for 5 *sec*. This cleaning step is necessary particularly to clean the *EM* junction area before *NP* evaporation. Then we load the sample inside an e-beam evaporator and deposit about 1-2 *nm* of *Au* on the sample at an evaporation rate of 0.02-0.04 *nm/sec*. Instead of forming a continuous metallic *Au* thin film, individual *Au* atoms are evaporated and settled down on the substrate, forming a layer of self-assembled nano-particles. The size of the particles are not very well controlled, this depends on the parameters including, the rate of evaporation, final thickness of the metal etc. After that, we test the tunnel resistance of the junctions in a probe station. If the resistance of the junction is
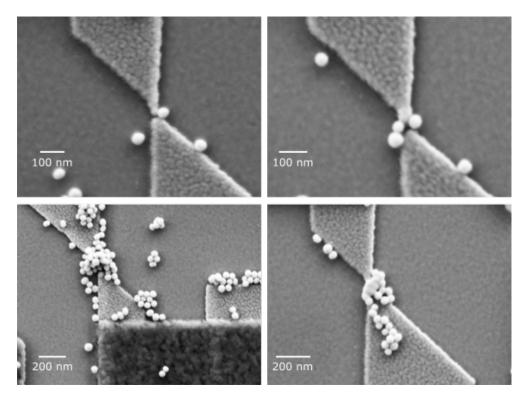
Fig. 2.13:   **Deposition of 50 nm GNPs by DEP method**   *SEM* images of the *EM* junctions with 50 *nm NP*s deposited by *DEP* method. For 50 nm *NP*s the trapping force is sufficiently high and as a result *NP*s gathered near the *EM* junction. Clearly the size of the particles is much higher than the *EM* gap, therefore few *NP*s ends up at the side of the gap. In some cases the fusing of the *NP*s, forming a *Au*-nanobridge is observed.

found below 10 MΩ, we consider that as a successful device and select that kind of devices for further low temperature measurements.

If we evaporate the *NP*s before the formation of *EM* gap, we directly load the sample inside an e-beam evaporator after finishing the lift off and cleaning by oxygen plasma, and evaporate in the same way about 1-2 nm of *Au*. In this case, the *EM* is done inside the cryostat at 4 *K*.

SEM images of few samples are shown in Fig. 2.14. Form the images, one can notice that the density of particle is very high. The distribution of the particle-size is found to be in range of $5 - 10$ *nm*. These particles are small enough to serve our requirement for a *QD*, with a sufficiently high charging energy and electronic-level spacing.

Selection of the most efficient method

As evident from the SEM image of a sample (Fig. 2.6), we have many probes connected to the source of the *QD*-transistor in order to accomplish the thermal transport measurement

Fig. 2.14: **Evaporation of Au NPs** *SEM* images of few samples with $Au-NP$s deposited on top of the *EM* junctions by the evaporation of few nm of Au in an e-beam evaporator. The density of the particle is very high, with a distribution of particle size between 5-8 *nm*.
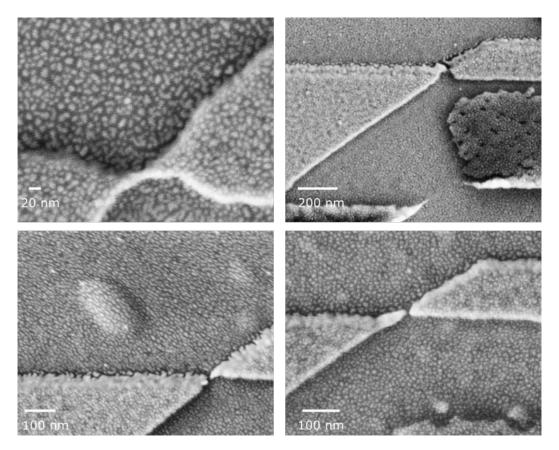
through the QD. We need at least 8 separate cryostat lines to connect a single device, therefore with a 27-line cryostat one can cool-down maximum 3 devices only in a single run. Given the stochastic nature of the *NP* deposition, this is very small number in order to get a successful *QD* device. This technical constraint demands us to find a *NP* deposition recipe with very high yield. All the four processes of *NP* deposition discussed above has some pros and cons, so we have to select the best one with highest yield.

From study of the deposition process we found that, the yield for getting a successful device using *drop cast* method is only about 3 %, Which is very small compared to our requirement.

In the *self assembly* method, the citric acid in the solution is found to be corrosive for the aluminum. We often observed either a complete removal of the *Al* or a damage of the device at the interface between *Au* and *Al* (Fig. 2.10 (c, d)).

The *DEP* trapping of *NP* does not work reasonably well for 5 and 12 *nm* particles, while it works very well for a *NP* with 50 nm diameter, but a *NP* with a 50 nm diameter is very

Table 2.3: Fabrication steps for single *QD* devices

#	Step description	Process	Comments
1	Back-gate and contact pads	Resist coating Laser exposure Development Metalization Lift off ALD Contact pads	Photo resist: LOR3A, S1805 50 mJ/cm^2 MF26/DI water Ti(3 nm)/Au (30 nm)/Ti(3 nm) at 0° Remover PG at 90°C Al$_2$O$_3$ 8 nm pattern by Laser-litho, evaporation Ti(3 nm)/Au(30 nm)/Ti(3 nm) at 0°
3	Constriction and SNS junctions	Resist coating E-beam exposure Development Wet cleaning Dry cleaning Evaporation-1 Evaporation-2 Evaporation-3 Liftoff cleaning	P(MMA/MAA) 9%/ PMMA 4% 50 nm 100 kV, 1 nA, 1000 μC/cm^2 MIBK+IPA 1:3, 1 min IPA, dry N_2 O_2 plasma, 10 W, 15 s Pt (11 nm) @ −42° Au+Ti(25 nm+3 nm) @ −25° Al(80 nm) @ 20° NMP @90° C 30 min Acetone/IPA/Ethanol, O_2 plasma 10 W 10s
4	Electromigration	ambient condition *in-situ*	probe station, small line resistance Adwin Pro-II, high line resistance of cryostat
4	GNP deposition	Drop-cast Self-assembling (APTES) Di-electroPhoresis (DEP) Sub-monolayer *Au* evaporation	∼ 3 % yield good concentration but damages device worked only for 50 nm *Au − NP* >70 % yield, 5 − 10 *nm* distribution

close to the dimensions of an *SET* island. Therefore we can not use these particle as a *QD*, as the charging energy of a 50 *nm* particle is expected to be very small (close to a typical *SET* of few 100 μeV) and a single electronic-levels are not accessible due to unresolvable level spacing.

The *sub-mono layer evaporation of Au* method is very random in terms of particle size, but the density of particle is very high. As a result we get an yield more than 70 % for a successful device, both in the case of *after EM* and *before EM*. The size of particles produced in this method are small enough to serve as a *QD*.

The measurements with QD devices described in this thesis, are made with 'Sub-mono layer *Au* evaporation' method. Initially, the evaporations are done after the formation of *EM* gap out side the cryostat, in an ambient condition. This gives rise to some successful *QD* device, but with very weak tunnel coupling between the *QD* and leads. We improved the tunnel coupling by performing the *EM* inside the cryostat, after the *NP* evaporation.

Chapter 3

Local Thermometry and Refrigeration

Free electrons in metal, obeying Fermi-Dirac statistics, can be defined at a finite electronic temperature (T_e). This can be measured directly by measuring any physical quantity that depends on temperature. In an experiment with mesoscopic devices, the choice of the electronic thermometer is determined by its application and how well it fits with the environment of the device. Most of the commonly used thermometers in a mesoscopic experiment are secondary thermometer, i.e. one has to calibrate it against a known temperature. The mostly used electronic thermometers are Normal-Insulator-Superconductor (*NIS*) tunnel junctions and Coulomb-Blockade thermometer. In the course of this thesis we have used the *NIS* thermometry for the measurement of thermal conductance of an *SET* and a new thermometry technique with an *SNS* proximity junction is developed for the measurement of heat flow in a *QD* junctions. The principle of these two thermometers will be discussed in this chapter.

3.1   NIS tunnel junction thermometry

A tunnel junction between a normal metal (*N*) and a superconductor (*S*) is one of the mostly used thermometer in mesoscopic heat transport experiments. We make such junctions by creating a tunnel barrier of Aluminum oxide (AlO_x) between Aluminum (*Al*) and Copper (*Cu*). An *SEM* image of such a NIS junction with the thermometry circuit is shown in Fig. 3.2 (b).

The energy diagram of a NIS tunnel junction at a finite bias V_{NIS} is shown in Fig. 3.1. The distribution function of the normal-metal *N* at a finite temperature (governed by the Fermi distribution) on the left is plotted with respect to energy on the vertical axis. The insulating layer in the middle is shown as a potential barrier, while the density of states (*DOS*) of the superconductor with an energy gap of 2Δ around the Fermi energy is shown on the right. At equilibrium, in the absence of any external bias, the Fermi level of the

normal metal is aligned to the Fermi level of the superconductor i.e. to the middle of the superconducting gap of the superconductor. As the Cooper pairs can not exist in normal metal, no flow of current is possible. Conduction is possible only through the tunneling of the quasi-particles, which is forbidden by the strong superconducting (*SC*) gap Δ. Therefore, in order to have conduction of quasi-particles through the tunnel barrier, one has to lower (raise) the chemical potential of the superconductor (normal-metal), by applying a relative voltage bias across the junction (Fig. 3.1). The conduction is unblocked when the bias voltage exceeds the superconducting gap, Δ. At a bias voltage $V_{\mathrm{NIS}} \gtrsim \Delta/e$, the quasi-particles can tunnel across the barrier, producing a quasi-particle current across the tunnel junction. The tunneling rate Γ_{NIS} of quasi-particles in a *NIS* tunnel junction can be obtained from the
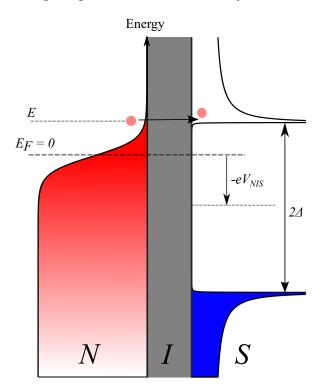
Fig. 3.1:   Energy diagram of a NIS junction   *DOS* of the Normal metal (*N*) and the Superconductor (*S*) are plotted along the horizontal axis with respect to the energy on the vertical axis. Fermi energy of the normal metal is taken as the reference. A bias voltage V_{NIS} on the *S* with respect to *N* lowers its chemical potential by eV_{NIS}. Only the excited quasiparticles with energy $E \approx k_{\mathrm{B}}T_{\mathrm{N}}$ above the Fermi level can tunnel across the barrier

Eq. (1.4). For a normal-metal, the density of states near the Fermi energy can be taken as a constant. Therefore, we can use the normalized density of states of the two reservoirs in Eq. (1.4) as, $n_1 = n_{\mathrm{N}} = 1$ and $n_2 = n_{\mathrm{S}}$, where $n_{\mathrm{N}}, n_{\mathrm{S}}$ are the normalized density of states of the normal metal and the superconductor respectively. The average tunnel current I_{NIS} though

the junction can be written after some simplifications as

$$I_{\mathrm{NIS}} = \frac{1}{2eR_{\mathrm{T,NIS}}} \int_{-\infty}^{\infty} dE n_{\mathrm{S}}(E) \left[f_{\mathrm{N}}(E - eV_{\mathrm{NIS}}) - f_{\mathrm{N}}(E + eV_{\mathrm{NIS}}) \right], \tag{3.1}$$

where $R_{\mathrm{T,NIS}}$ is the tunnel resistance of the junction. The normalized *DOS* of superconductor is given by

$$n_{\mathrm{S}}(E) = \mathrm{Re} \left(\frac{|E + i\gamma|}{\sqrt{(E + i\gamma)^2 - \Delta^2}} \right), \tag{3.2}$$

γ being the Dynes broadening parameter of the superconducting gap and

$$f_{\mathrm{N}}(E) = \frac{1}{\exp(1 + \frac{E}{k_{\mathrm{B}} T_{\mathrm{N}}})} \tag{3.3}$$

is the Fermi distribution function of the Normal metal, at a temperature T_{N}.

The tunneling current at a bias below the sub-gap Δ is expected to be exponentially suppressed with decreasing temperature due to the presence of strong *BCS* gap. Yet, a small sub-gap leakage current is routinely observed in experiments [62, 88, 63, 64, 89, 90]. This is often attributed to the Dynes parameter (Eq. (3.2)), incorporating the effect of finite lifetime of the quasi-particles into the *BCS DOS* [91, 92], which can be ascribed to the photon-assisted quasi-particle tunneling [65]. The leakage sub-gap current can also attributed to higher order tunneling of the Cooper pairs via Andreev reflection [93–96], by which a Cooper pair in *S* enters into *N* splitting into two electrons of opposite spin and momenta or vice versa.

In Fig. 3.1 it is shown that the *DOS* of the normal metal at a finite temperature T_{N} is smeared around the Fermi energy, of the order of $k_{\mathrm{B}} T_{\mathrm{N}}$, where k_{B} is the Boltzmann constant. Therefore, at a bias $V_{\mathrm{NIS}} \approx \Delta/e$, the onset of the tunnel current depends on the level of smearing of the *DOS* and hence on the temperature of the normal-metal. It can also be seen from Eq. (3.1) that the tunnel current depends only on the distribution function $f_{\mathrm{N}}(E)$ of the normal metal. This is valid as long as the superconducting gap can be assumed to be a constant, equal to its zero-temperature value. Therefore, measuring the voltage drop across the *NIS* junction with a constant current bias of $I_{\mathrm{NIS}} = I_{\mathrm{th}}$, one can directly measure the distribution function $f_{\mathrm{N}}(E)$ of the normal metal and hence its equilibrium temperature T_{N} using Eq. (3.3) [62, 97–99].

Fig. 3.2 (a) shows the calculated $I - V$ curves of a *NIS* junction at different bath temperature T_{b}, equal to the temperature of the normal metal T_{N}, using the Eq. (3.1). The parameters used in the calculation are from a regular *NIS* junction (shown in Fig. 3.2 (b)) with a constant *SC* gap $\Delta = 208 \ \mu eV$, a tunnel resistance $R_{\mathrm{T,NIS}} = 13 \ k\Omega$ and a Dynes broadening parameter $\gamma = 8 \times 10^{-4} \Delta$. The *IV* curves are smeared out with the increasing

temperature, due to the smearing of the distribution of the normal metal. If we take a cut of the *IV* curves at a fixed current $I_{NIS} = I_{th}$, different onset voltage can be found for different curves corresponding to a particular electronic temperature of the normal metal. Thus, the measured voltage at a constant current $I_{NIS} = I_{th}$ can directly give the equilibrium electronic temperature of the normal metal.
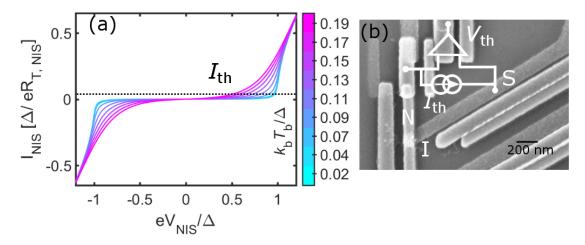
Fig. 3.2: Calculated NIS IV characteristics   (a) Tunnelling current of a *NIS* junction with respect to the applied voltage bias at different bath temperatures T_b ranging from $k_B T_b = 0.02\Delta$ to 0.19Δ, Δ being the superconducting gap of Al of 208 μeV (b) SEM image of a typical *NIS* junction with the thermometry circuit, a constant bias current I_{th} is chosen from the *IV* characteristics shown on the left, where the measured voltage is most sensitive to the temperature

Although the *NIS* junctions are very convenient to use as an on chip thermometer to measure the local electronic temperature, the characteristics of the junctions are not always very consistent and depend on the fabrication parameters. This implies that, it can not be used as primary thermometer and has to be always calibrated with respect to a known temperature. In the experiment described in Chapter 4, we calibrate the *NIS* thermometer with respect to our known cryostat temperature. Calibration is done at equilibrium, so that the cryostat temperature (equal to the phonon temperature) can be attributed to the electronic temperature of the normal metal. We biased the junction with a constant current, bias current set point is chosen to be low enough such that the voltage drop across the junction is well below Δ (so that the thermometer probe can not cool the normal metal, discussed in the following sec. 3.2). The voltage drop across the junction is measured with respect to known bath temperature, the measurement circuit being shown in Fig. 3.2 (b). Therefore, converting the measured voltage with the aid of the calibration curve gives us the electronic temperature of the normal metal. A typical calibration curve is shown in Fig. 3.3.
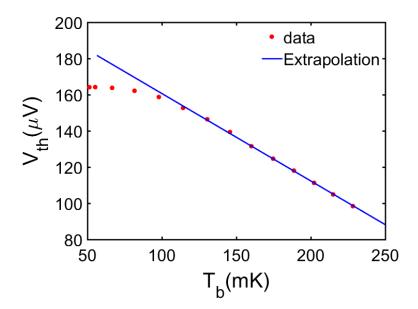
Fig. 3.3: NIS thermometer calibration Measured voltage across a *NIS* junction as a function of the bath temperature T_b gives the calibration of the thermometer. A saturation of the measured voltage is found at a bath temperature below 100 mK, this puts a limit on the sensitivity of the thermometer at low temperature.

3.2 NIS tunnel junction refrigerator

Apart from thermometry, a *NIS* tunnel junction can also be used as a mesoscopic solid-state refrigerator, which can cool down the electrons in the normal part of the junction with respect to their environment temperature. This can be achieved by voltage biasing the tunnel junction with a voltage $V_{\text{NIS}} \lesssim \Delta/e$ [62, 97]. When a *NIS* junction is biased with a voltage just below the sub-gap Δ, the high energy electrons in the N above the Fermi energy can tunnel into the S across the barrier, while electrons near the Fermi level can not tunnel due to the strong energy filter imposed by the *SC* gap Δ. In the other way, when the voltage bias is applied on the S, the quasi-particles with relatively low energy below the the sub-gap Δ can only tunnel into the N. Due to this energy filtering by the *SC* gap, heat is evacuated from the normal metal, as a result the electronic temperature of the normal metal goes below the environment and an electronic refrigeration is possible.

The heat current from the N to S, $\dot{Q}_{\text{NIS}}$ can be written in the same manner as the tunnel current using Eq. (1.47)-(1.49) as:

$$\dot{Q}_{\text{NIS}} = \frac{1}{e^2 R_{\text{T,NIS}}} \int_{-\infty}^{\infty} dE n_{\text{S}}(E)(E - eV_{\text{NIS}}) \left[f_{\text{N}}(E - eV_{\text{NIS}}) - f_{\text{S}}(E) \right], \qquad (3.4)$$

which is deposited to the *S* in addition with the Joule dissipation due to the quasi-particle tunneling, $I_{\text{NIS}}V_{\text{NIS}}$. The calculated cooling power $\dot{Q}_{\text{NIS}}$ for a *NIS* tunnel junction with respect
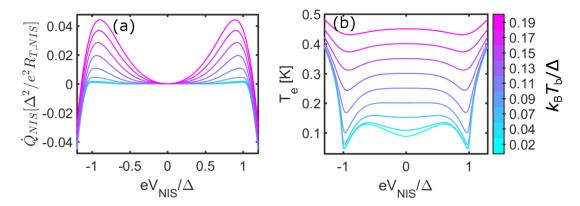
Fig. 3.4:   Calculated NIS cooling power and electronic temperature of the normal-metal   (a) Cooling power of a *NIS* junction with respect to the applied voltage bias at different bath temperature T_{b}, ranging from $k_{\text{B}}T_{\text{b}} = 0.02\Delta$ to 0.19Δ, where Δ is the *SC* gap of Al taken to be 208 μeV and temperature independent. Positive cooling power indicates cooling of the nomal-metal while negative corresponds to heating due to Joule dissipation, the optimal cooling power is obtained at a cooler bias $V_{\text{NIS}} \lesssim \Delta/e$. (b) Electronic temperature of the normal-part of the *NIS* tunnel junction as a function of the cooler bias and at different bath temperature T_{b} ranging from $k_{\text{B}}T_{\text{b}} = 0.02\Delta$ to 0.19Δ, obtained from the heat balance between cooling power of the *NIS* junction and the $e - ph$ coupling power at the corresponding bath temperature. At low bath temperature, the calculated electron temperature is found to be above the bath, which can be due to the extra parasitic noise coming from the electromagnetic environment. This overheating can also be attributed to the andreev current mostly significant for a less opaque tunnel junction [96]

to the applied voltage bias at different temperatures $T_{\text{b}} = T_{\text{N}} = T_{\text{S}}$ (up to a temperature where we can assume Δ to be temperature independent) is shown in Fig. 3.4 (a). A positive value of $\dot{Q}_{\text{NIS}}$ indicates the extraction of heat from the normal metal and hence cooling of the same. As it can be seen from the plots, the cooling power $\dot{Q}_{\text{NIS}}$ has a nonlinear dependence with the voltage bias V_{NIS}. It has a maximum and positive value at a bias $V_{\text{NIS}} \lesssim \Delta/e$ for all the temperatures. Above this bias, it produces the usual Joule heating due to the quasi-particle current, which gives rise to a large negative value of $\dot{Q}_{\text{NIS}}$. In the low temperature limit, $T_{\text{N}} \leq T_{\text{S}} \leq \Delta/k_{\text{B}}$ where we can assume Δ as a constant, the optimal bias at which the cooling power maximizes, can be approximated as $V_{\text{NIS,opt}} \approx (\Delta - 0.66k_{\text{B}}T_{\text{N}})/e$, whereas the corresponding optimal cooling power is given by [100],

$$\dot{Q}_{\text{NIS,opt}} = \frac{\Delta^2}{e^2 R_{\text{T,NIS}}} \left[0.59 \left(\frac{k_{\text{B}}T_{\text{N}}}{\Delta} \right)^{3/2} - \sqrt{\frac{2\pi k_{\text{B}}T_{\text{S}}}{\Delta}} \exp\left(\frac{-\Delta}{k_{\text{B}}T_{\text{S}}} \right) \right]. \qquad (3.5)$$

The efficiency of extracting heat from the normal metal by the *NIS* refrigerator is defined by the ratio of its cooling power $\dot{Q}_{\text{NIS}}$ to the total applied power, $P_{\text{total}} = I_{\text{NIS}}(V_{\text{NIS}})V_{\text{NIS}}$. It is expressed by the coefficient of performance (η) as,

$$\eta = \frac{\dot{Q}_{\text{NIS}}}{P_{\text{total}}} = \frac{\dot{Q}_{\text{NIS}}(V_{\text{NIS}})}{I_{\text{NIS}}(V_{\text{NIS}})V_{\text{NIS}}} \tag{3.6}$$

Similar to the optimal cooling power in the low temperature limit, the optimal efficiency a *NIS* refrigerator at a voltage bias $V_{\text{NIS}} \approx \Delta/e$ in the low temperature limit can be written as [100],

$$\eta_{\text{opt}} \approx 0.7\frac{T_{\text{N}}}{T_{\text{c}}}; \tag{3.7}$$

where the *SC* gap Δ is taken to be constant, $\Delta = 1.764 k_{\text{B}}T_{\text{c}}$ and T_{c} is the critical temperature of the superconductor.

In quasi-equilibrium condition, i.e., when the mean electronic escape time from the normal metal is longer than the $e-e$ interaction time [101–103], the effective electronic temperature of the normal metal is determined by the heat balance between the incoming cooling power $\dot{Q}_{\text{NIS}}$ from the *NIS* tunnel junction and the outgoing heat current (power) due to the relaxation of the electrons with phonons coupled to the bath temperature, given by the $e-ph$ coupling power $\dot{Q}_{\text{e-ph}} = \Sigma\mathscr{V}\left(T_{\text{N}}^5 - T_{\text{b}}^5\right)$ [62]. The heat balance equation in the steady-state then reads,

$$\dot{Q}_{\text{NIS}} - \Sigma\mathscr{V}\left(T_{\text{N}}^5 - T_{\text{b}}^5\right) = 0 \tag{3.8}$$

where Σ is a material dependent constant and $\mathscr{V}$ is the volume of the normal metal coupled to the bath via $e-ph$ coupling. Often in low-temperature experiments, a parasitic noise coming from the electromagnetic environment can heat up the normal-metal not allowing it to thermalize to the bath temperature, which is more significant towards the low temperatures. In that case, a constant parasitic power P_0 is accounted within the term $\dot{Q}_{\text{NIS}}$ in the heat balance equation (Eq. (3.8)).

Fig. 3.4 (b) shows the calculated electronic temperature versus the applied voltage bias, solving the heat balance equation (Eq. (3.8)) for a normal metal island made of *Cu* with the material dependent constant $\Sigma = 2.6 \times 10^9 \, Wm^{-3}K^{-5}$ [62] and with a volume $\mathscr{V} = 1.5 \times 10^{-20} \, m^3$. As it is expected, the maximum temperature reduction of the normal metal from the bath temperature is obtained for a voltage bias $V_{\text{NIS}} \approx \Delta/e$ and an overheating above the bath temperature is obtained at higher bias voltages.

3.3   SNS proximity junction thermometry

When a superconducting metal is placed in close proximity of a normal metal via clean (direct) contact, the superconducting pair amplitude can penetrate into the normal metal over a length of $L_T = \sqrt{\hbar D / 2\pi k_B T}$, known as the thermal coherence length, where, $D = v_F l_e / 3$ is the electronic diffusion constant, l_e, v_F being the electronic mean free path and the Fermi velocity of the normal metal, respectively. This phenomenon is well known as proximity effect [104–112]. This induces a weak superconducting gap in the spectrum of the normal metal. In an *SNS* junction where a normal (N) metal is placed between two superconductor (S) in transparent contact, the density of states in the normal metal is modified and a mini gap is induced in it [113–118]. As a result a supercurrent can flow though the *SNS* junction [119–121].
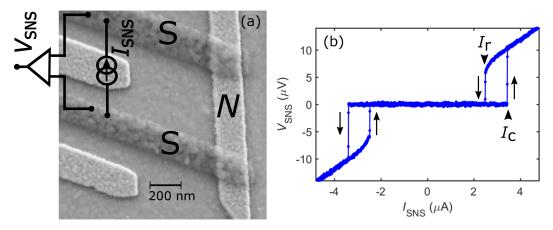
Fig. 3.5:   SNS IV characteristics   (a) SEM image of an SNS junction with the circuit for thermometry (b) A typical *IV* characteristics of an SNS junction for forward and backward sweep. Sweep direction of the current is indicated by the arrows. The current in the forward sweep at which the junction switches to the resistive state is indicated as critical current I_c and the current in the backward sweep at which the junction switches back to superconducting state is indicated as retrapping current I_r. In this specific junction, $I_r < I_c$ showing that the junction is hysteretic. The overheating of the *N* due to Joule dissipation in the resistive state is found to be the origin of the hysteresis [122]

3.3.1   Andreev transport in SNS junction

The transport of supercurrent in an *SNS* junction is governed by multiple Andreev reflection [123–126]. The full process of supercurrent transport through an *SNS* junction is depicted in the drawing of Fig. 3.6. This can be explained in the following way. Let us consider an electron in the normal metal with an energy, $E < \Delta$, with respect to the Fermi level, impinges on the right *NS* interface of the junction and is reflected back a phase-coherent

hole of same energy but with an opposite momentum vector. As a result a Cooper pair of electrons of opposite spin is created in the right superconductor. The phase coherent hole travels through the normal metal and impinges again at the left *NS* interface and reflected as a phase-coherent electron into the normal metal. As a result it annihilates a Cooper pair in the left superconductor. In this way one Cooper pair in the left *S* is transported to the right *S* through the normal metal in the middle via a phase-coherent multiple Andreev reflection. This process continues in a cycle producing a phase coherent state, called Andreev bound state [127, 108, 120]. These states carries the supercurrent in *SNS* junction [128, 129, 124, 120, 121].
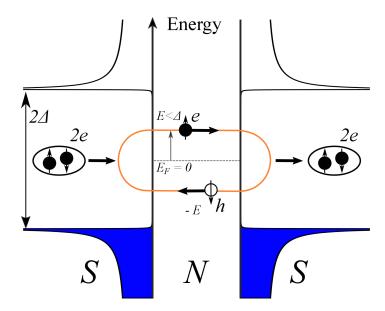
Fig. 3.6: **Supercurrent transport in an SNS junction by multiple Andreev reflection** An electron in the normal metal with an energy $E < \Delta$, with respect to the Fermi energy and with spin *up* reflected from the right *NS* interface as a hole of enegy $-E$ and spin *down*, which is again reflected from the left interface as an electron with enrgy E and spin *up*, producing a phase-coherent Andreev bound state. As a result a Cooper pair from the left superconductor is transported to the right one causing a flow of supercurrent in *SNS* junction

3.3.2 Hysteresis in a Proximity SNS junction

Fig. 3.5 (a) shows the *SEM* image of a typical *SNS* junction used for the measurements in this thesis, with the biasing circuitry to characterize it. The *SNS* junction is current biased with a constant current I_{SNS} and the voltage drop across it V_{SNS} is measured. A typical *IV* characteristics of the junction for forward and reverse sweep is shown in Fig. 3.5 (b). One can notice that, in this specific junction, the current at which the junction switches from the superconducting (*SC*) state to the resistive state and vice versa, are not the same for forward

and reverse sweep. This indicates that the junction has a hysteretic behaviour. The switching current in the forward sweep where the junction switch from *SC* state to resistive state is called the critical current (I_c), while the switching current in the reverse sweep where the junction recovers the *SC* state is called the retrapping current (I_r) of the junction. The origin of hysteresis in an *SNS* junction was a long standing issue until last decade [130–134], and is now well understood to have thermal origin [122]. According to the Resistively Capacitively Shunted Junction (RCSJ) model [135, 136] of Josephson junction, the hysteresis can appear due to the capacitance of the junction. But in a proximity *SNS* junction the geometrical capacitance of the junction is negligible, meaning the behaviour is over-damped. Still, one regularly sees the existence of significant hysteresis of the critical current in a proximity *SNS* junction (Fig. 3.5 (b)). With the aid of additional *NIS* probes, Courtois et al. [122] measured the temperature of the normal metal of an *SNS* junction and found that the electrons in the *N* gets overheated once it switches to the resistive state. It does not go to the equilibrium temperature of the system (i.e. to the superconducting state) until the bias current is reduced below the retrapping current $I_r < I_c$ and hence the junction shows a hysteresis.

3.3.3 Critical current of SNS junction

The proximity effect induces the superconducting correlation in the normal metal of *SNS* junction producing a supercurrent carried by the phase-coherent Andreev bound states. The critical current of the junction falls exponentially with the length of *N*-metal in the *SNS* junction, $I_c \propto \exp(-L/L_T)$. In experiments, the length of the junction L is larger than the mean free path l_e of electrons and smaller than the electronic phase-coherence length l_ϕ, $l_e < L < l_\phi$, so the transport is considered to be diffusive and phase-coherent. The energy scale that is relevant in the study of proximity *SNS* junction is the Thouless energy $\varepsilon_{th} = \hbar D/L^2$ [108, 106]. The Thouless energy describes the electronic diffusion process in the normal metal, $\varepsilon_{th}/\hbar$ gives the rate at which the electrons diffuse across the sample, which is relevant specially for the non-equilibrium supercurrent transport [137–139]. When the length of the junction is larger than the superconducting coherence length $\xi_0 = \sqrt{\hbar D/\Delta}$ of the superconductor, where Δ is the superconducting gap, which is equivalent to $\Delta >> \varepsilon_{th}$, the junction is considered to be in the *long-junction limit* [105, 134]. Here we will consider the long-junction limit only.

Temperature dependence of I_c

Temperature dependence of the critical current in an *SNS* junction has been studied for long time within the Ginzburg-Landau theory [140], but the predicted behavior is correct only

close to T_c. Later for a diffusive *SNS* microbridge the temperature dependence was well described by Likharev with the quasiclassical Usadel equations [110, 109, 141, 142]. A more general study of the Josephson effect in diffusive *SNS* junction was described with the approach of quasiclassical Green's function in imaginary time [104, 129, 105].

This temperature dependent feature of the *SNS* junction can be used for thermometry in order to measure the local electronic temperature of the normal metal. The critical current of an *SNS* junction is a monotonous function of temperature. In the high temperature limit, i.e. $k_B T_e >> \varepsilon_{th}$, the critical current increases with the decrease of electronic temperature. At low temperature a saturation appears when the temperature is smaller than the Thouless energy, $k_B T_e < \varepsilon_{th}$. The critical current at absolute zero temperature is a constant value depending on the Thouless energy of the junction.

In the high temperature limit ($k_B T_e >> \varepsilon_{th} \equiv L >> L_T$), the critical current can be written from the Usadel equation as [104, 105],

$$eR_N I_c = 64\pi k_B T_e \sum_{n=0}^{\infty} \frac{L}{L_{\omega_n}} \frac{\Delta^2 exp(-L/L_\omega)}{[\omega_n + \Omega_n + \sqrt{2(\Omega^2 + \omega_n \Omega_n)}]^2}, \qquad (3.9)$$

where R_N is the normal state resistance, $\omega_n = (2n+1)\pi k_B T_e$ is the Matsubara frequency, $\Omega_n = \sqrt{\Delta^2 + \omega_n^2}$ and $L_{\omega_n} = \sqrt{\hbar D/2\omega_n}$

At lower temperatures $k_B T_e \lesssim \varepsilon_{th}$ calculation of I_c is much more difficult as it involves the solution of the Usadel equation at all energies. At zero temperature the normalized critical current is a constant [105]:

$$eR_N I_c = 10.82\varepsilon_{th} \qquad (3.10)$$

For a temperature $k_B T_e > 5\varepsilon_{th}$, sum in Eq. (3.9) is essentially contributed by the first frequency term $\omega_0 = \pi k_B T_e$ with $L_{\omega_0} = L_T$. Therefore, the expression for the critical current in the Eq. (3.9) can be approximated in the limit of $\Delta/\varepsilon_{th} \to \infty$ as,

$$eR_N I_c = \frac{32}{3+2\sqrt{2}} \varepsilon_{th} \left(\frac{L}{L_T}\right)^3 e^{-L/L_T} \qquad (3.11)$$

3.3.4 Measurement of critical current

The critical current I_c of an *SNS* junction can be measured by simply measuring the switching current of the junction in a single sweep of the biasing current, but the measurement of such single event can be erroneous, as the switching of the junction is a stochastic process [134]. This can be explained by the fictitious particle in the *RSJ* model [128, 135, 136], trapped inside a tilted oscillating potential board, where the slope of the potential board is governed by critical current of the junction. For a small biasing current, the slope of the potential board

is small enough to trap the particle into the oscillating potential barrier, implying the junction to be in the *SC* state. As current increases the potential becomes more tilted and the escape of the particle is possible at the critical current. The escape of the particle is a stochastic process as the process can be triggered by thermal or quantum activation. Therefore, the switching current has a certain probability distribution at certain temperature, depending on the thermal or quantum noise. We measure the I_c of the *SNS* junction and calibrate it as a thermometer with respect to bath temperature in two ways, DC single sweep measurement and by AC statistics measurement of the switching current.

DC measurement of I_c

For the DC measurement of I_c we bias the *SNS* junction with a DC current and measure the voltage drop across it. From the IV characteristic we extract the critical current I_c, defined by the value of the current at which the measured voltage is at least larger than a threshold voltage V_{Th} above the noise level of the voltage measurement. Fig. 3.7 (a) shows the *IV*
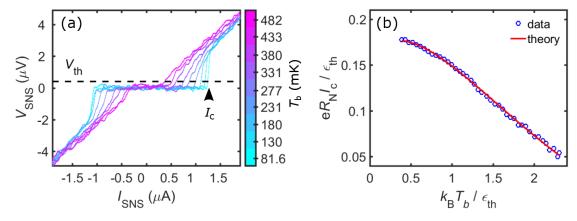
Fig. 3.7: DC calibration of SNS thermometer   (a) DC IV characteristics of an *SNS* junction at different bath temperatures, the switching current I_c is indicated by the arrow, defined by the current at which the voltage across the junction exceeds the threshold value V_{Th} (b) The critical current I_c of the junction at different bath temperature gives the calibration of the thermometer, here both the axes are normalized, the solid line is the fit of the data with the theory of Eq. (3.9). We use the measured normal-state resistance and the diffusion constant (D) as fixed parameter and the Thouless energy (ε_{th}), interface transparency η as the free parameters. The fit gives an estimate of $\varepsilon_{th} = 10\ \mu eV$ and the effective length of the normal metal (L_{eff}) matching very well with the geometry of the junction revealed by *SEM* images.

curves of a typical *SNS* junction (Fig. 3.5 (a)) at different bath temperature, a threshold voltage V_{Th} is defined at $0.2\ \mu V$ (where the junction is already switched to normal state) for extracting the critical current of the junction. The extracted critical current as a function of the bath temperature is shown in Fig. 3.7 (b). This gives the calibration of the thermometer

from the DC measurement. Both the axes are normalized with the Thouless energy. The solid line shows the fit of the data with the Eq. (3.9). From the fit of I_c vs T_b data we extract the parameters of the junction. The diffusion constant $D = 76 \, \text{cm}^2/\text{s}$ of the normal metal for this particular junction is determined by the normal state resistance of the junction, which is used in the fit to extract the Thouless energy $\varepsilon_{th} \simeq 14 \, \mu\text{eV}$. The effective length of the N-metal $L_{eff} = 600$ nm is very close to the estimate from *SEM* image. As the Thouless energy ε_{th} is very small compared to the thermal energy $k_B T_b$, an unsaturated temperature dependence of I_c is found for the range of temperature of 100-400 mK. A saturation is observed below 80 mK, where the Thouless energy is comparable to the $k_B T_b$. This saturation in I_c might also come from heating of the normal metal by parasitic noise.

AC measurement of I_c

As the switching of the junction from the *SC* state to the resistive state is a stochastic process, a statistical measurement is required to determine the critical current I_c correctly. This requires thousands of measurements of the switching current at the fixed condition of the junction environment, to get the distribution of switching currents. It is meaningless to perform such a huge number of switching current measurement by DC single sweeps, as this is time consuming and therefore it is difficult to keep the junction environment unchanged. For this reason we developed a new way of measuring the statistics of the switching current, by biasing the junction with an AC signal [143–145]. This method is used in the measurement of temperatures described in Chapter 5. Fig. 3.8 shows the measurement scheme for AC statistics measurement of the switching current with a triangular AC signal of frequency 300 Hz, amplitude 130 mV and with an offset + 10 mV. This AC voltage signal is used to current bias the *SNS* junction through a $100 \, k\Omega - 1 \, M\Omega$ biasing resistor, much higher than the junction resistance, thereby satisfying proper current biasing condition. Other than a triangular wave form, we could also use a sinusoid and sawtooth signal for the statistics measurement. The choice of adding offset to the signal is to remove unnecessary overheating for the negative part of the oscillation period.

The switching current is recorded by an oscilloscope triggered just above the switching of the junction. In this way 3000 measurements of switching currents are obtained in just 10 sec. A histogram of such measurements of switching current at a constant bath temperature $T_b =$105 mK is shown in in Fig. 3.9. The envelope of the histogram is fitted with a Gaussian (shown in solid line) in order to extract the average of the distribution, indicated by the red arrow in Fig. 3.9. One can notice that the histogram shown in Fig. 3.9 has an asymmetric nature, it has a longer tail towards the lower bias current. This kind of behavior of the histograms are more pronounced at a very low temperatures below 100 mK. This could be
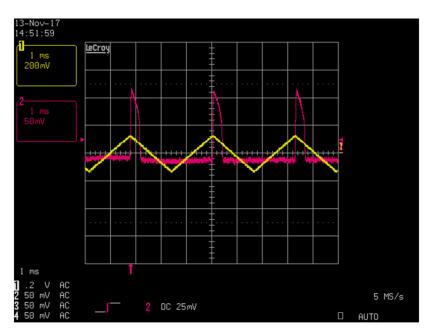
Fig. 3.8:   Switching current statistics measurement procedure   Screen-shot of the oscilloscope (LeCroy Waverunner LT224) used for the measurement of the switching current statistics. In channel-1 (shown in Yellow) we probe the input bias voltage (which is used for current biasing the *SNS* junction), in this case it is a triangular signal of 300 Hz frequency, 130 mV amplitude and with an offset of +10 mV. The measured voltage across the *SNS* junction is probed by the channel-2 (shown in Red) after amplification. The measured voltage signal is zero until the input bias current is below the critical current. A sudden jump of the measured voltage is attributed to the switch of the junction from superconducting state to resistive state once the bias current exceeds the critical current. Above this current an Ohmic behavior of the junction produces a linear decrease of measured voltage and finally a sudden drop of the voltage to zero is again attributed to the reduction of the bias current below the retrapping current when the junction comes back to the superconducting state. The oscilloscope is triggered to a value just above the zero base line of the output voltage signal, when the junction is already switched, indicated by the 'red-arrow' on the y-axis. In this way the the oscilloscope records the value of the input bias voltage (and hence the bias current) at which the junction is switched for each period.

understood as the effect of thermal noise, which can induce a switching for a low bias-current, while for a bias-current above the average value of the distribution, the switching process is more deterministic and will in any case occurs below the maximum value. We use the average of the distribution $[I_{SNS}]_{avg}$ or the most probable switching current $[I_{SNS}]_{P_{max}}$ as the actual critical current of the junction.

The above mentioned procedure describes the measurement of the most probable critical current of the *SNS* junction at a single bath temperature. We use this method to calibrate the *SNS* junction thermometer with respect to the known bath temperature. The histograms of 3000 measurements of switching current at different bath temperature, with a fit of the envelope of each histogram with a Gaussian, is shown in Fig. 3.10. Form the histograms in
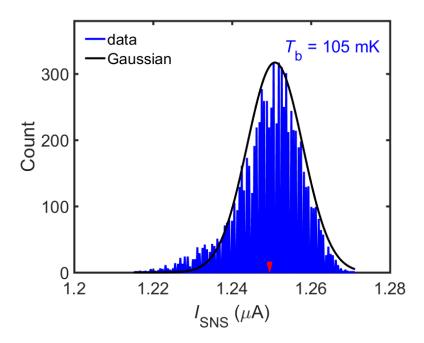
Fig. 3.9: **Histogram of switching current** Histogram plot of the 3000 measurements of switching current of an *SNS* junction at a bath temperature of 105 mK. The full measurement takes only 10 sec. The solid line is the Gaussian fit of the histogram. The average of the distribution is indicated by the red arrow, consider as the critical current of the junction.

Fig. 3.10, a clear trend can be found that, the height of the histogram is decreasing, while the width is increasing with temperature. Indicating that the measurement is more deterministic towards low temperature.

The extracted average switching current from each histograms at different bath temperature is plotted as a function of the bath temperature in Fig. 3.11 (left), while the standard deviation of the histograms as a function of the bath temperature T_b is shown in Fig. 3.11 (right).

Temperature dependence of the width of the histogram

The distribution of the switching current of the junction has a certain width, given by the thermal or quantum noise. At high temperature the width of the histogram is determined by the thermal energy $k_B T$, as the dominant contribution comes from the thermal activation. If one extends the theory of *SIS* junction to *SNS* junction, the width of the histogram in this high temperature regime can be found as, $std[I_{SNS}]/I_{SNS} \approx (k_B T/\varepsilon_{th})^{2/3}$. At low temperature the thermal energy is very small and most of the contribution to the distribution of switching current comes from the quantum tunneling across the barrier. The quantum tunneling onset temperature is defined as $T^* = \hbar\omega_p/2\pi k_B$, where $\omega_p/2\pi$ is the plasma frequency of the
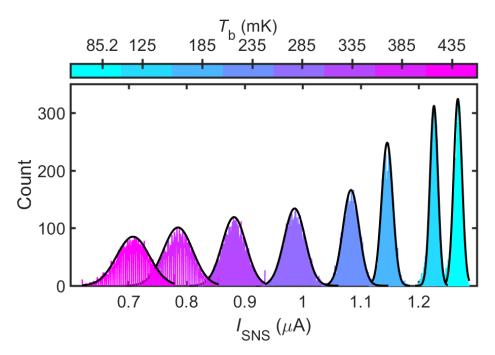
Fig. 3.10: **Histograms of switching current at different bath temperature**   Histograms of the switching current of an *SNS* junction at several bath temperature, with a Gaussian fit for each histogram. One can easily notice that the height and width of the histogram changes with temperature, with a trend that the height drops with temperature, while the width increases. This is attributed to the thermal noise present at higher temperature which helps the junction to switch and gives a broader distribution.

quantum well. The onset temperature is of the order of $\varepsilon_{\text{th}}/k_{\text{B}}$. Below this temperature the critical current get saturated, with a dependence of $T^{4/5}$. From the plot of standard deviation of histograms as a function of temperature (Fig. 3.11 (Right)), we can easily distinguish the two regimes. The high temperature regime, where the standard deviation increases linearly with temperature and low temperature regime, where it is saturated. A linear fit of the data is also shown in Fig. 3.11 (right). The data in the high temperature regime fits better with a T dependence, compared to a $T^{2/3}$ dependence. The saturation of standard deviation is observed at a bath temperature $T_b = 155$ mK, while the estimate of T^* from the fitted value of the $\varepsilon_{\text{th}} \simeq 14\ \mu eV$ gives a value $T^* \simeq 164$ mK. Therefore the observed onset temperature matches well with the estimation.

3.3.5   Performance of an optimized SNS thermometer

Our final goal is to measure the heat-flow through a *QD* junction, which requires a very sensitive thermometer at an operating temperature < 100 mK, in order to detect a little change of electronic temperature. We optimized the sensitivity of the *SNS* thermometer
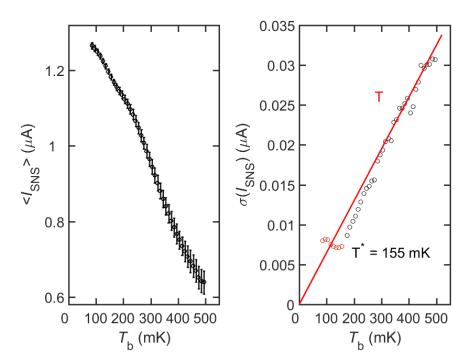
Fig. 3.11: AC calibration of a SNS thermometer (a) The average of the distribution of the switching current is plotted as a function of the bath temperature, the error-bar comes from the standard deviation of the distribution. (b) The standard deviation for each of the distributions of the switching current is plotted as function of the temperature. We can notice that this curve has two regimes, the standard deviation drops with temperature when the bath temperature is sufficiently high, while it gets saturated at lower bath temperature, indicating the onset of macroscopic quantum tunneling

with several repetitions of the junction parameters including, length, thickness of the normal metal and thereby reducing the Thouless energy of the junction. At the optimization stage, the normal part of the *SNS* junctions and the electromigartion-constriction were made at the same step of metal-evaporation. Therefore the thickness of the normal part of the *SNS* junctions could not be varied independently. This restriction was lifted by adding a third angle of evaporation.

Here, we analyze the sensitivity of an optimized thermometer integrated with a dummy *QD*-device (*SEM* of the device is similar to Fig. 2.6 (b)). The constriction is broken by electromigration but no nano-particles are deposited. Therefore, the device can be essentially considered as a $\sim 5\ \mu m$ long and ~ 100 nm wide rectangular metallic *Au*-island, with a short *SNS* junction for measuring its electronic temperature and a relatively longer *SNS* junction to heat it up. In the steady state, the temperature of the island is determined by the heat balance
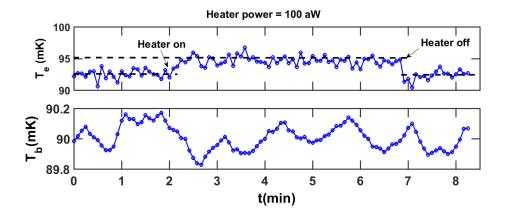
Fig. 3.12: **Real time trace of the temperature with the application of 100 aW power** Temperature of the normal metal source island measured as function of time. An increase of the temperature of about 5 *mK* is observed with the application of 100 aW power to the source island. This increase of the local electronic temperature of the source results form the heat balance between the input Joule heating power of 100 aW and the heat relaxation to the phonon bath. Similarly the thermalization to the bath temperature is observed with the withdrawal of heating. This measurement indicates that the *SNS* thermometer is capable of measuring a heating by a very small heating power of the order of 100 *aW*.

between the input-heat from the heater $\dot{Q}_H$ and the heat-leak through the phonons, i.e.,

$$\dot{Q}_H - \Sigma \mathcal{V} \left(T_e^5 - T_b^5 \right) = 0, \tag{3.12}$$

where Σ is a material dependent parameter and $\mathcal{V}$ is the volume of the island.

The *SNS* thermometer is calibrated against the known cryostat temperature (Fig. 3.11 (right)). No saturation is observed in the calibration (I_c vs T) curve even at the base temperature of ~ 80 *mK*. From the calibration curve (Fig. 3.11 (right)) we obtain the sensitivity of the thermometer to be $dI_c/dT = 1.5 \ \mu A/K$. The average error in the measurement of I_c is 5 *nA*, within 70 % confidence level. From this two values the noise in the temperature measurement is found to be $200 \ \mu K/\sqrt{Hz}$.

In order to know whether the thermometer can detect heating by a very small heating-power, we performed an experiment to measure the temperature of the island in real time, at a bath temperature $T_b = 90$ *mK*. We measure the temperature of the island by the statistical measurement of 500 switching events of the *SNS* junction. From the histograms of the switching current we obtain the average switching current I_c. The real time trace of the electronic temperature of the island is shown in Fig. 3.12.

Initially, the heater is turned off, we measure the equilibrium temperature $T_e \sim 92.5$ mK as obtained from the calibration of the thermometer.

The heater is set to a constant current bias of 5 *nA*, driven by a 1.3 *V* isolated voltage source with a 200 *M*Ω bias resister. This biasing current dissipates on the heater junction of resistance $R_H \approx 9$ Ω (rough estimate from the four probe normal-state resistance of the thermometer junction) and deposit a heating power of $\dot{Q}_H \approx 100$ *aW* on the island. We measure a decrease in I_c and hence an increase in the electronic temperature as soon as we turned on the heater. The electronic temperature of the island can be extracted by solving the heat balance equation (Eq. 3.12), using the sample parameters, $\Sigma = 2.4 \times 10^9$ $Wm^{-3}K^{-5}$ for *Au*, the volume of the island $\mathcal{V} = 2 \times 10^{-20}$ m^3 obtained from the *SEM* image. We found that above observed temperature increase of $\Delta T_e \sim 3$ *mK* (Fig. 3.12) matches with the estimation with a heater junction resistance $R_H = 3.5$ Ω, almost 3 times smaller than the rough estimate of $R_H \approx 9\Omega$ (from the four probe normal-state resistance measurement of the thermometer junction). This discrepancy with the estimated value of R_H could be due to the parasitic heat loss from the island, e.g. though the *Al* leads due to anti-proximity effect.

3.4   NIS vs SNS thermometry

Since we have used the two thermometry techniques based on *NIS* or *SNS* junctions in the measurement of local electronic temperature, in this section we describe a comparison between the two in terms of their performance and identify its pros and cons from the experimental point of view. This is summarized in the Table 3.1.

1. *Impedance*: Very high impedance for *NIS* junction typically 10-50 *k*Ω; while *SNS* junction has very low impedance typically 2-10 Ω;

2. *Access resistance*: *NIS* junctions are not suitable for conductance measurement due to the high access resistance (con); while *SNS* junctions are perfect for conductance measurements, e.g. an *SNS* thermometer can be integrated with a *QD* device due to a negligible access resistance (pro);

3. *Modification of DOS of sample*: a *NIS* junction does not modify the DOS of the normal metal whose temperature need to be measured (pro); but the *SNS* junction induces a mini hard gap in the DOS of the normal metal (con);

4. *Sensitivity*: a *NIS* thermometer regularly saturates below 100 mK (con); while *SNS* thermometer can be sensitive even below 100 mK (pro);

Table 3.1:   Comparison between *NIS* and *SNS* thermometry with Pros and Cons

Issues	NIS	SNS
Impedance	high impedance	low impedance
Access resistance	high access resistance	negligible access resistance
DOS modification	Do not modify	induces a mini hard gap
Sensitivity	saturates below 100 mK	sensitive below 100 mK
measurement difficulty	simple single measurement	longer statistical measurement
Dissipation	Dissipates	Dissipates above I_c
Lifetime	no degradation	depends on materials
Thermal insulation	good	only below 300 mK

5. *Measurement difficulty*: for *NIS* junction thermometer measurement of temperature is simply done by a single measurement of voltage drop across the junction; while for *SNS* junction thermometer a complicated and relatively long statistical measurement of the critical current is required in order to measure the temperature correctly;

6. *Dissipation*: a *NIS* junction dissipates at the tunnel barrier (con) ; while the *SNS* junction dissipates only above the critical current (pro);

7. *Lifetime and consistency*: *NIS* junctions are not degraded over time and the behaviour is more consistent (pro); but for *SNS* junction depending on the choice of metal the lifetime of the junction can be very short (con);

8. *Thermal insulation*: *NIS* junction has a good thermal insulation at all temperature (pro); but *SNS* junction has effective thermal insulation only for a bath temperature below 300 mK (con);

Chapter 4

Thermal Conductance of a Single-Electron Transistor

In this chapter, we present a combined measurement of both heat and charge conductance through a metallic Single-Electron Transistor (SET). It is a small metallic 'Island' coupled to two thermal reservoirs, called the 'Source' and 'Drain' of the transistor. The electrons in the island are subject to a strong electron-electron interaction. Therefore, one needs to pay an extra charging energy, in order to tunnel an extra electron into the island. The reservoirs are treated as Fermi-sea of non-interacting electrons, obeying Fermi-Dirac statics. The energy selective tunnelling of electrons from the reservoir to the island, hints the existence of rich physics in the heat flow through these devices, which is being mostly unexplored yet, in spite of good understanding of charge transport in these devices. Here we present a simple yet challenging measurement to probe the heat flow though the SET. The device acts as a heat switch depending on the applied gate potential. Pure heat and charge transport measurements allow us to check the validity of the celebrated Wiedemann-Franz (WF) law. A strong violation of the WF law is observed away from the degeneracy point. The observed deviation agrees well with the theoretical expectation. Measured heat flow through the SET is found to be strongly non-linear with squared temperature, deep inside the coulomb blockade region.

4.1 Device specifications

The thermal transport measurement in an SET requires the extraction of exact amount of heat flow from one side to the other through the SET island. Heat is not necessarily conserved in the circuit, as it can leak out via many paths, which are not easily measurable. Our approach is to measure the quasi-equilibrium electronic temperature of both the leads of the SET. This

gives us quantitative determination of the heat flow through the island by making a heat balance out of all possible paths of heat flow.

For this, we made the devices with two types of design, 'Symmetric' and 'asymmetric' *SET*. In the symmetric design, we made both the source and drain of the *SET* out of a very narrow and small volume metallic island, in order to thermally decouple both of the leads from environment. We have thermometer and cooler/heater probes connected to both of them. Therefore, one can heat/cool and measure the electronic temperature of both of the leads at the same time. An *SEM* image of a symmetric *SET* is shown in Fig. 4.1.
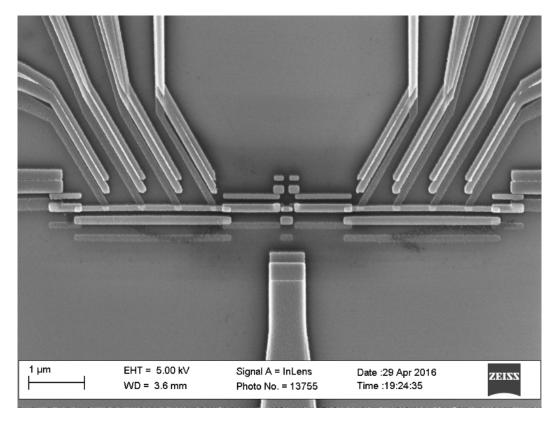
Fig. 4.1:   SEM image of a symmetric SET   SET with symmetric Source and Drain. Four *Al* probes are connected on both sides via tunnel barrier in order to measure and change the electronic temperature.

During the measurements with the *symmetric SET*, we found that the heat balance of the system is disturbed due to the cross-talk between the measurement setup for the temperature measurement of both leads simultaneously, with the *NIS* thermometers. Therefore, we move to the *asymmetric* design of the SET, where we measure the electronic temperature of the source only, while electronic temperature of the drain is inferred from the bath temperature, due to good coupling to the phonons. All the measurements presented in this chapter are with *asymmetric SET*.

In the asymmetric design, the drain of the SET is connected to a bulky electrode and therefore is well thermalized to the bath temperature, while the source is again made narrow and tiny, in order to decouple it from the environment. The island of the SET is made very small in volume in order to be able to neglect the e-ph coupling in it. Fig. 4.2 (a) shows a color SEM image of the full device while Fig. 4.2 (b) shows schematics with the same colors for each element.

The source is thermally decoupled from the bath, in spite of the probes connected to it. This is achieved by reducing its volume, which decreases the e-ph contribution to the heat leak from it, and by connecting it through a clean contact to an Al lead. This superconducting Al lead connected at the end of the source acts as a thermal mirror because of the superconducting gap present in Al, on the other hand it allows us to perform the charge transport measurement. Additionally, four superconducting Al leads are connected to the source via tunnel contacts, which serve either as thermometer to measure the local electronic temperature of the source or to heat up (cool down) the source electrons above (below) the bath temperature.

If we concentrate on the central part of the device (Fig. 4.2 (b)), we can see another beauty of the design, that the Cu island (yellow) is connected to the source (red) and drain (green) through two small pieces of Al strips(100 nm), which are oxidized before the deposition of the Island. The two Al strips are in clean contact with huge metallic source and drain, which renders them normal by inverse proximity effect, while they are in tunnel contact with the island [146]. The advantage of making the tunnel junctions for the SET in this way is that this is the easiest way of making very stable *AlOx* layer between two normal metal structures. We can precisely control the thickness of the tunnel barrier by controlling the time of oxidation and pressure of injected oxygen.

4.2   SET characterization

In order to understand the thermal transport through the SET, we need to first characterize it by charge transport, to estimate the charging energy E_C and the tunneling resistance R_T. Assuming symmetric junctions with identical resistances $R_T/2$, a straightforward and reliable way to obtain them is to make a fit to the measured minimum and maximum current I_{SET} at each bias voltage V_{SET} with the orthodox theory. In this thesis we mainly consider two samples with identical geometry, one with high tunnel resistance (Sample A) and another with small tunnel resistance (Sample B) (see Table 4.1). Fig. 4.2 (d) shows the differential conductance of Sample B, at 50 mK as a function of both the SET bias V_{SET} and the average number $n_g = C_g V_g / e$ of electrons induced electrostatically by the gate potential V_g on the island. Here C_g is the capacitance between the gate and the island. Coulomb diamonds (in
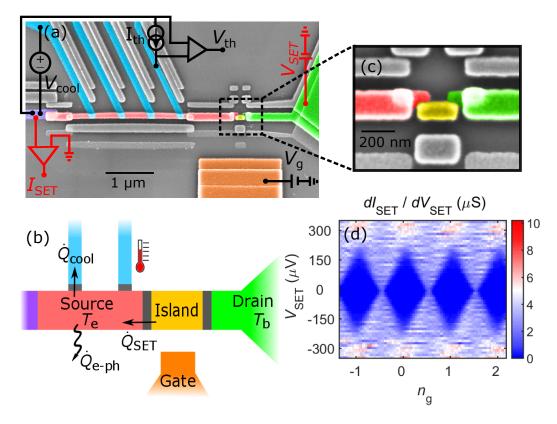
Fig. 4.2:   A single electron transistor with heat and charge transport measurement set-up (Adapted from Dutta et al. [103]) (a) False-colored SEM image of the full device. The circuit in red indicates the charge transport set-up, while the black one stands for the heat transport set-up. (b) Schematic of the device, with the different elements shown in colors. (c) Zoomed-in view of the central part of the SET. (d) Differential conductance map of sample A SET at 50 mK against drain-source voltage V_{SET} and induced charge n_{g}.

dark blue) are regions of zero current through the SET. Every diamond is centered around an integer value of n_{g} and defines a fixed charge state on the island.

At zero bias, the charge conductance is thus vanishing, except in the vicinity of the degeneracy points at half-integer values of n_{g}. At these points, two charge states have the same energy and the conductance (for small barrier transparency) is half the high-temperature value, which is related to the fact that only these two states are involved. The measured current I_{SET} at $T_{\text{b}} = 72$ mK, as a function of the applied bias V_{g}, at different gate voltage V_{g} (blue dots along the vertical direction), enclosed by the calculated envelope curves corresponding to I_{SET} at $n_{\text{g}} = 0$ and at $n_{\text{g}} = 1/2$, are shown in Fig. 4.3 for sample B. From this procedure, performed at several bath temperatures T_{b}, we estimate $E_{\text{C}} = 155\,\mu$eV and $R_{\text{T}} = 82$ kΩ for sample A, $E_{\text{C}} = 100\,\mu$eV and $R_{\text{T}} = 26$ kΩ for sample B (see Table 4.1). The charge transport causes some dissipation at the tunnel barriers, which produces extra Joule heat in the leads. Therefore one should not consider a constant temperature (equal to the bath temperature)

Sample	Total tunnel resistance (R_T)	Charging energy (E_C)
A	$164\,\text{k}\Omega$	$155\,\mu\text{eV}$
B	$52\,\text{k}\Omega$	$100\,\mu\text{eV}$

in the calculation, for both of the leads. To estimate the parameters more accurately, we consider the thermal balance in the source to extract its electronic temperature. This is again used in the calculation of the *SET* parameters.
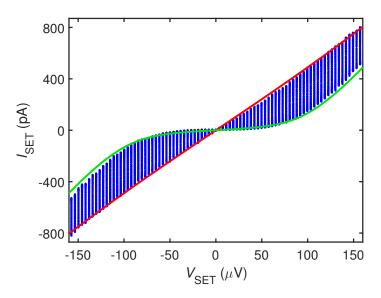
Fig. 4.3:   IV characteristics of an SET at different gate positions   SET current for Sample B, plotted for different values of the induced charge n_g as a function of V_{SET}, together with envelope curves calculated at $n_g = 0$ (green) and at $n_g = 1/2$ (red).

4.3   NIS thermometer and cooler characterization

Apart from the *SET* parameters, we also need to characterize the *NIS* junctions that will be used as thermometer or cooler/ heater, in order to study the heat transport through the *SET*. We use one of the four *NIS* junctions as an electronic thermometer. For the calibration of the thermometer, the *NIS* junction is biased with a constant current of few *pA* and the voltage drop across the junction is measured as a function of the bath temperature [62, 99, 98]. The biasing current has to be small enough so that the voltage drop is much below the superconducting gap of *Al*, in order to avoid any significant cooling. A typical calibration curve is shown in Fig. 4.4.
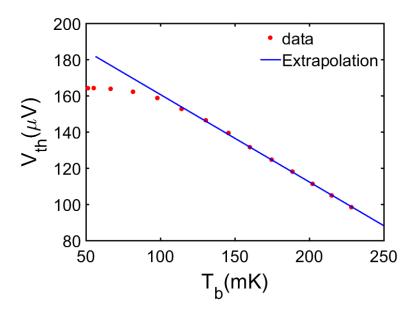
Fig. 4.4: Calibration of the NIS thermometer A typical calibration of a *NIS* thermometer with respect to known bath temperature.

To estimate the cooling (heating) power of the cooler junction we need to characterize the cooler (heater) junction. We do this by fitting the measured IV characteristics of the *NIS* junction with theory (Eq. (3.1)). The fitting gives us the values of the normal state tunnel resistance $R_{\mathrm{T,NIS}}$, low-temperature superconducting energy gap Δ, and the dimensionless Dynes broadening parameter γ.

The low-temperature IV characteristic of the NIS cooler (heater) junction of sample B is shown in Fig. 4.5, both on linear and logarithmic scale, together with the calculated I_{NIS}. For this sample we obtain $R_{\mathrm{T,NIS}} = 13.2$ kΩ, $\Delta = 208$ μeV, and $\gamma = 8 \times 10^{-4}$. When compared to effects caused by the overheating of the superconducting electrode, the exact value of γ or other subgap features of the I–V curve do not play a significant role in modeling the cooling power of the NIS junction at voltages V_{NIS} close to Δ/e.

4.4   Heat transport measurement

In this experiment, our approach is to study the thermal balance in the source when it is heated or cooled. In every thermal measurement, we ensured that no current is flowing through the SET, so that pure heat transport can be considered. The thermal conductance of the SET is inferred from the heat balance in the source, and then compared to the electrical conductance measured in parallel.
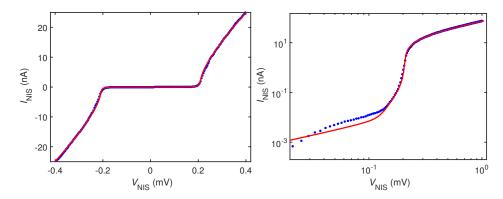
Fig. 4.5: IV characteristics of the NIS junction with theoretical fits Current–voltage characteristic of one NIS junction of sample B on (left) linear and (right) logarithmic scale. Fits are shown as full red lines.

We will consider here that the electron population of the source is in quasi-equilibrium at a well-defined (electronic) temperature T_e. This is justified as the mean electron escape time from this element is longer than the estimated electron-electron interaction time [101]. By heating or cooling electrons in the source, its electronic temperature T_e can be different from the temperature of the phonons thermalized at the bath temperature T_b.

We apply proper voltage bias to the *NIS* junction, to cool or heat the source electrons with respect to phonons. The cooling and heating of the source electronic bath is illustrated for sample B in Fig. 4.6 left. Here one NIS junction to the source is used for thermometry while a second junction acts as a cooler used for cooling/heating. At a low cooler bias V_{cool}, the electronic temperature T_e is below the bath temperature T_b of 152 mK (indicated by a horizontal dashed line in Fig. 4.6 left) so that cooling is achieved. The maximum temperature reduction of about 50 mK is reached at a potential drop V_{cool} of about 190 μeV, close to the gap Δ for Al. A larger cooling is obtained when the gate potential is adjusted so that electron transport through the SET is blocked ($n_g = 0$) and so is thermal transport through it. At higher bias of the cooler ($V_{cool} > \Delta$), an electron overheating is obtained: $T_e > T_b$. Again, the electron temperature change (here an increase) is larger when the SET is blocked. The electron temperature at a fixed cooler bias but as a function of the gate potential is displayed in Fig. 4.6 right. Clear temperature oscillations are obtained, with an opposite sign for the electron cooling and the over-heating regimes. This demonstrates the contribution of the thermal conductance of the SET to heat transport.
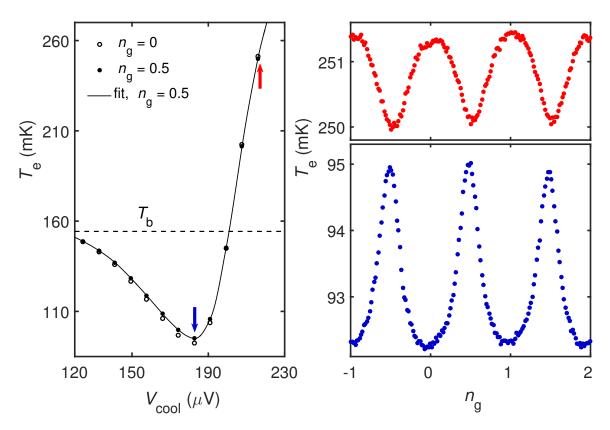
Fig. 4.6: Gate modulated heat transport (Adapted from Dutta et al. [103]) Left: Variation of electronic temperature T_e of sample B source with cooler bias voltage, at gate open ($n_g = 0.5$) and gate closed ($n_g = 0$) states, at a bath temperature T_b of 152 mK. The full line is a fit of the gate-open state data, see text. Right: Temperature modulation by the gate voltage expressed in terms of induced charge n_g in the heating regime (top) and in the cooling regime (bottom) at cooler bias points indicated by the blue and red arrows in the left plot.

4.5 Analysis

In order to quantify the thermal conductance through the SET, we describe the thermal balance in the source following a thermal model depicted in Fig. 1b. In this model, the electron bath in the source receives the power $\dot{Q}_{cool}$ from the cooler junction, with a positive or negative sign corresponding to cooling or heating respectively. It can be obtained using Eq. (1.47) and (1.48) [62]

$$\dot{Q}_{cool} = \frac{1}{e^2 R_{cool}} \int_{-\infty}^{\infty} (E - eV_{cool}) n_S(E) [f_{source}(E - eV_{cool}) - f_S(E)] dE - \dot{Q}_0, \qquad (4.1)$$

where R_{cool} is the tunnel junction resistance of the cooler, $n_S(E)$ is the (BCS) density of states of the superconductor, $f_{source,S}(E)$ is the thermal energy distribution function in the source or the S lead of the cooler at respective temperatures T_e and T_S. The parasitic power

$\dot{Q}_0$ takes into account imperfect thermalization of the electrical connections. The main energy relaxation channel for the source electrons is the coupling to phonons, with a power following,

$$\dot{Q}_{\text{e-ph}} = \Sigma \mathscr{V} (T_{\text{e}}^5 - T_{\text{ph}}^5), \tag{4.2}$$

where Σ is characteristic of the material, $\mathscr{V}$ is the volume, and T_{ph} is the phonon temperature here assumed to be equal to the bath temperature [62]. Eventually, the SET transmits a power $\dot{Q}_{\text{SET}}$ to the source.

Here we assume that there is no heat loss in the island, i.e. whatever heat enters to the island from the source goes to the drain. The volume of the island is so small that the electron-phonon coupling is negligible here. We check this assumption separately, by calculating the e-ph power loss out of the island. By considering the temperature of the island to be the average of the temperature of two leads, we found that the e-ph coupling power of the island is less than 5 % of the heat flow through the *SET*, $\dot{Q}_{\text{SET}}$ and hence most of the heat is transported through the *SET* without any further loss in the island.

4.5.1 Calibration of heat flow at a known gate position

In order to quantify all the relevant parameters for the thermal balance, we calibrate the heat flow through the system at a known position of gate. This can be either the gate voltage corresponding to the gate-close position $n_{\text{g}} = 0$ or to the gate-open position $n_{\text{g}} = 0.5$, because at these two position we can approximate the heat flow to be zero or to be governed by Weidemann-Franz (*WF*) law, respectively. The approximation of zero heat flow through the *SET* is only valid when the tunnel coupling of island to the lead is very weak, meaning there are no co-tunnelling processes at the centre of the Coulomb-diamonds. In contrast, the other assumption at the gate-open position is always valid.

The validity of the second assumption, that the heat flow at gate-open position is governed by *WF* law can be checked with sample A. As the coupling in sample A is very weak, we can assume here the heat flow to be zero at the gate-close position with a good approximation and we found a perfect match of the heat flow at gate-open position with the *WF* value. Therefore, we use the second assumption at gate-open position to calibrate the heat flow for both samples A and B.

At the gate-open position $n_{\text{g}} = 0.5$, the two charge states involved in electron transport have the same electrostatic energy. Electron transport is thus (for small barrier transparency) unaffected by electron interaction and the Wiedemann-Franz law is expected to be valid. The power $\dot{Q}_{\text{SET}}$ can thus be calculated from the measured differential conductance for charge dI/dV at low bias using *WF* law (Eq. (1.40)). We use the following thermal balance for the

source electrons,

$$\dot{Q}_{\text{SET}} - \dot{Q}_{\text{cool}} - \dot{Q}_{\text{e-ph}} = 0, \tag{4.3}$$

in order to extract the cooling/heating power $\dot{Q}_{\text{cool}}$. Here the electron-phonon coupling power $\dot{Q}_{\text{e-ph}}$ is calculated using the actual volume $\mathscr{V}$ and a parameter value $\Sigma = 2.8\,\text{nW}\,\mu\text{m}^{-3}\,\text{K}^{-5}$, close to the expected value for Cu [147]. The parasitic power $\dot{Q}_0$ is found to be 0.1 fW in agreement with previous works [148].

The thermal balance model (Eq. (4.3)) is complicated by the deviation of $\dot{Q}_{\text{cool}}$ from the ideal value predicted by Eq. (4.1) when one assume $T_S \equiv T_b$, i.e. the S electrode of the *NIS* cooler junction being perfectly thermalized to the bath temperature. In reality the S lead can be at an elevated temperature T_S, compared to the bath temperature T_b due to the injection of non-equilibrium quasiparticles at $eV_{\text{cool}} \approx \Delta$ and improper evacuation of the same. In experiments, this overheating of the superconducting lead can be avoided by adding a quasiparticle trap [149–153], we do not have that possibility in our experiment. Still, at each cooler bias V_{cool} and bath temperature T_b, we solve the thermal balance Eq. (4.3) at gate-open position ($n_g = 0.5$) using T_S as a free parameter to fit the measured electronic temperature T_e of the source. In this way we found that at a bath temperature $T_b \approx 150\,\text{mK}$, the superconductor temperature shows values $T_S \approx (250 - 450)\,\text{mK}$, cf. Fig. 4.7. The order of magnitude of the T_S appears realistic when compared to experiments in similar structures [152].

There is another way of heat loss from the *SET* source, by the thermal conductance of the superconducting lead connected to the source by clean contact. The thermal conductance of a pure superconductor is exponentially suppressed by the superconducting gap, with respect to its normal state thermal conductance. But when the superconductor is in proximity to a normal metal, the inverse proximity effect induced in the superconductor over a length, of the order of the superconducting coherence length ($\xi_0 = \hbar D/2\Delta$, Where D is the diffusion constant of electrons), can cause some thermal conductivity inside the superconductor. It is shown in experiment [154] that, the thermal conductance of the superconductor is negligible if the length of the superconductor exceeds a 'safe-length' of about 6 μm before it touches the normal metal and if the operating temperature is below 300 mK. These two conditions are satisfied in our experiment, therefore, we can neglect this contribution in the thermal balance. All our calculations are consistent for bath temperatures up to 300 mK where thermal leakage through the superconducting lead of the source starts to contribute significantly.

Once the elevated T_S has been extracted in the above manner, we can use it as well as the *measured* T_e, to extract $\dot{Q}_{\text{SET}}$ from the heat balance. Notably, this procedure is independent of the model for the SET heat flows – it rests only on the assumption that $\dot{Q}_{\text{SET}}(n_g = 0.5)$ fulfills the Wiedemann-Franz law (Eq. (1.40)).
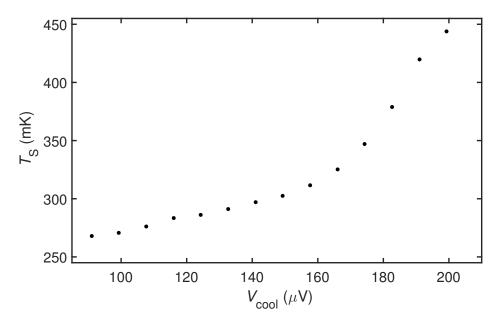
Fig. 4.7:   Temperature of the superconductor with NIS cooler bias   Calculated value of the NIS cooler superconductor temperature T_S for sample B, used in the fit of Fig. 4.6 data.

4.5.2   Heat balance at arbitrary gate positions

The preceding analysis at the gate open state provides us with a full knowledge of the thermal behavior of the source, including all physical parameters for electronic cooling and electron-phonon coupling. We now assume that, whatever the gate potential is, the temperature of the superconducting leads of the cooler varies with the cooler's bias as determined above in the gate open case. The measured values of the source electronic temperature $T_e(n_g)$ are used to calculate the heat flowing through the SET from Eq. (4.3) as,

$$\dot{Q}_{SET} = \dot{Q}_{cool} + \dot{Q}_{e\text{-}ph}, \tag{4.4}$$

as a function of n_g. Considering the limit of a small temperature difference, the SET heat conductance is then calculated as,

$$\kappa = \frac{\dot{Q}_{SET}}{|T_b - T_e|}. \tag{4.5}$$

Figure 4.8 shows both the heat conductance κ and the charge conductance σ for samples A and B, as a function of the gate potential. Both quantities were measured at the same bath temperature. An SET bias of about 20 μV and an electron cooling by about 25 mK were used for the charge and the heat transport measurements respectively. The charge conductance is plotted in units of the low-bias gate-open conductance σ_0. The heat conductance is plotted in
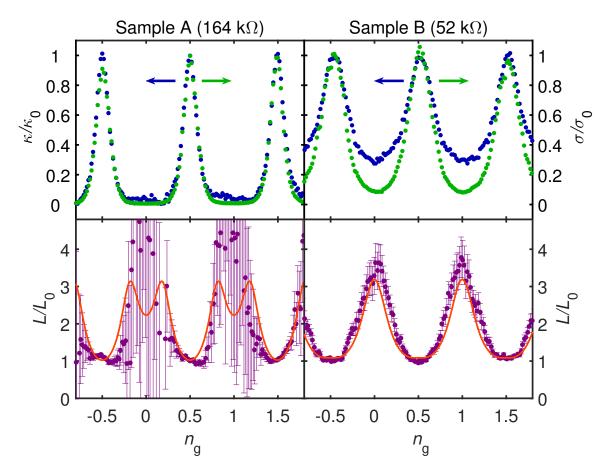
Fig. 4.8: Comparison of charge and thermal conductance   (Adapted from Dutta et al. [103])
Top: Thermal (blue dots) and charge (green dots) conductances of the SET at a bath temperature of 132
mK (left, sample A) and 152 mK (right, sample B) in units of the conductances in the gate-open state
κ_0 and σ_0. The thermal flow through the SET was calculated assuming that the Wiedemann-Franz law
is fulfilled at the gate-open state. The charge transport was measured at a bias of 22.4 μV (sample
A) and 19.2 μV (sample B). The heat transport data was acquired by cooling the source electronic
bath by 30 mK (sample A) and 22 mK (sample B) below the bath temperature. Bottom: Lorenz ratio
(purple dots) defined as L/L_0 where $L = \kappa/(\sigma T_m)$ for sample A (left) and sample B (right). The
error bars are related to the uncertainty in temperature measurement. The Wiedemann-Franz law sets
$L = L_0$. The red line is the theoretical prediction based on Ref. [13].

units of the Wiedemann-Franz value in the gate-open state,

$$\kappa_0 = \sigma_0 L_0 T_m. \tag{4.6}$$

We use here the mean temperature,

$$T_m = \frac{(T_e + T_b)}{2}, \tag{4.7}$$

so that a linear response is expected in the Wiedemann-Franz regime even for the case of a significant temperature difference $T_e - T_b$.

For both samples A and B, the charge and heat conductances oscillate with n_g. In the case of sample A (top left), the two conductances mostly overlap over the full gate potential range. Close to the gate-closed state, the two conductances seem to deviate one from the other but their absolute values are small. In contrast, sample B exhibits a clear deviation from the Wiedemann-Franz law. At the gate closed state, the heat conductance clearly exceeds the charge conductance multiplied by L_0T.

4.5.3   Violation of Wiedemann-Franz law

In order to get more insight, let us now consider the Lorenz factor defined as L/L_0 with

$$L = \frac{\kappa}{(\sigma T_m)}. \tag{4.8}$$

The Wiedemann-Franz law sets a Lorenz factor equal to unity. In contrast, for sample B the Lorenz factor (Fig. 3 bottom right) oscillates between 1 at gate-open state and about 4 at gate closed state. Sample A shows essentially the same behaviour over the gate potential range where it can be accurately determined whereas error bars are very large in the vicinity of the gate-closed state due to vanishingly small conductances. This experimental result shows a significant violation of the Wiedemann-Franz law in the *SET*.

We have performed the same analysis at several cooler bias points and found similar behaviour observed in Fig. 4.8. The results in the heating regime shown in Fig. 4.9, where the cooler bias is set to a value less than Δ, superconducting gap of *Al*. Here, the source electronic bath is hotter than the bath temperature by 60 mK (Sample A) and 52 mK (Sample B) and the charge transport measurements were taken at a bias of 22.4 μV (Sample A) and 19.2 μV (Sample B). It shows that the deviation of the heat flow from the Wiedemann-Franz value holds for the full range of the cooler bias, both in the cooling and heating regimes. In this case, the temperature difference is significant. It is then particularly important to use, in the calculation of the Lorenz factor, the temperature T_m that is the mean between the cold side (the bath temperature) and the hot side (the electron temperature).

The physical origin of the violation of the Wiedemann-Franz law resides in the energy selectivity of electron transport through an SET. As a consequence of this, the population of electrons flowing through the SET is non-thermal. For instance, at the gate-closed state, only electrons with an energy (counted from the Fermi level) above the charging energy E_C contribute to the zero-bias SET conductance. These electrons obviously carry the same (electron) charge but a higher energy. Thus the heat conductance does not decay due to
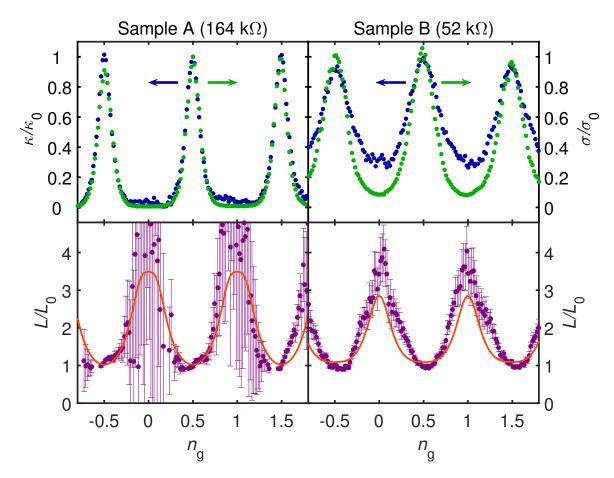
Fig. 4.9: **Comparison of charge and thermal conductance in the heating regime**   Top: Thermal and electrical conductances of the SET for sample A (left) and sample B (right) at a bath temperature of 132 mK (sample A) and 152 mK (sample B). The thermal flow through the SET was calculated assuming that the Wiedemann-Franz law is fulfilled at gate-open state. The charge transport measurement was done at a bias of 22.4 μV (sample A) and 19.2 μV (sample B). The heat transport data was acquired by heating the source electronic bath by 60 mK (sample A) and 52 mK (sample B) above the bath temperature. Bottom: Lorenz ratio defined as L/L_0 where $L = \kappa/(\sigma T_{\mathrm{m}})$ for sample A (left) and sample B (right). The red line is the theoretical prediction.

interactions as much as the charge conductance does and the Lorenz number exceeds its basic value L_0. Electron co-tunneling can counter-balance this, as it involves electrons with an energy close to the Fermi level. The cross-over to the co-tunneling regime shows up at the gate-closed state as a maximum of the Lorenz factor at a temperature $T \approx 0.1 E_{\mathrm{C}}/k_{\mathrm{B}}$ [13].

In order to calculate the Lorenz ratio we have used the existing theory from Kubala et al.[13]. Fig. 4.8 and Fig. 4.9 bottom panel show as full lines the calculated Lorenz factor in parallel with the experimental data for cooling and heating regime respectively. The theoretical prediction and the experimental data matches very well for both of the cases, within error bars. There are no free parameters in this comparison with theory.
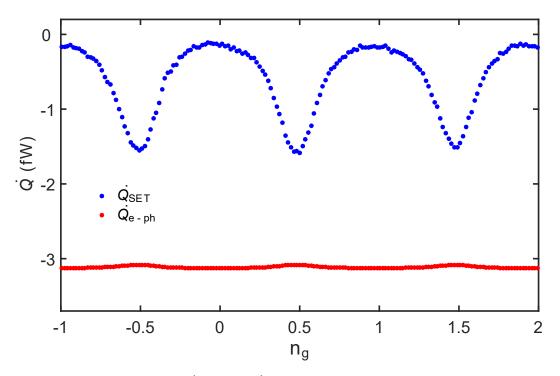
Fig. 4.10: comparison of $\dot{Q}_{\mathrm{SET}}$ and $\dot{Q}_{\mathrm{e\text{-}ph}}$ at different gate positions Dependence of the electron-phonon coupling power $\dot{Q}_{\mathrm{e\text{-}ph}}$ and the power flow through the SET $\dot{Q}_{\mathrm{SET}}$, on the gate potential, related to the data of Fig. 4.6.

All the parameters are taken from the preceding analysis of charge and heat transport measurement. The main relevant parameters here are $k_{\mathrm{B}}T/E_{\mathrm{C}} \approx 0.06$ and 0.12 for sample A and B respectively and the measured values of the SETs conductance.

For sample A in the cooling regime, theory predicts a relative minimum in the gate-closed state, due to the presence of co-tunnelling process, which cannot be checked in the experiment due to experimental uncertainties. The error bars account the uncertainty in the measurement of temperature and the electrical conductance.

4.5.4 Non-linear heat flow

We have also compared the percentage of total heat flow via all possible heat relaxation processes. The amount of heat flow by the two most dominant heat relaxation process, e-ph coupling and thermal conductance of the *SET* as a function of the gate voltage, are shown in Fig. 4.10. It is observed that the power flow through the SET can represent up to 30% of the total power flow at 150 mK.

Further, we investigated the power law in an *SET* at different gate voltages. From the heat balance in the source island, we extract the heat flow, $\dot{Q}_{\mathrm{SET}}$ flowing through the SET beyond
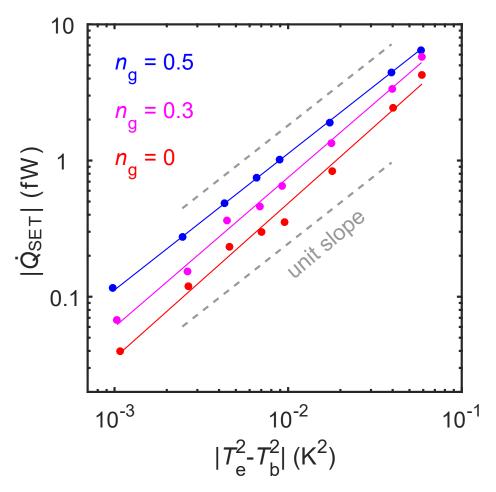
Fig. 4.11: Non-linear heat flow through SET (Adapted from Dutta et al. [103]) Non-linear heat flow through sample B SET at different gate states as a function of the difference of the squared temperatures between the source and the bath (symbols) together with power-law fits (full lines). The slopes are 1.00, 1.10 and 1.14 respectively at gate positions $n_g = 0.5$, 0.3 and 0. Unit slope expected for the linear regime of heat transport is shown as dotted grey lines.

the regime of small temperature differences. In the linear regime, the thermal conductance κ is proportional to temperature, leading to the quadratic dependence of the power on the source (T_e) and drain (T_b) temperatures:

$$\dot{Q}_{SET} = \int_{T_b}^{T_e} \sigma_0 L \, dT = \frac{\sigma_0 L}{2}(T_e^2 - T_b^2) = \sigma_0 L \frac{T_e + T_b}{2}(T_e - T_b) = \sigma_0 L T_m (T_e - T_b), \quad (4.9)$$

where T_m is the average temperature of the leads.

Fig. 4.11 shows the measured heat flow through the *SET* as a function of the squared temperature difference at different gate position, on a log-log plot. This includes data from both heating and cooling regimes and compares experimental data (dots) to the above law. In the gate-open case $n_g = 0.5$, slope is 1 as assumed in the calibration, i.e. the heat flow is

quadratic in temperature as expected from the Wiedemann-Franz law. If we go away from the gate-open state, a larger slope is found, up to 1.14 at $n_g = 0$, indicating that the heat flow at these gate positions is non-linear. Further theoretical work is needed to compare this observation to theoretical predictions.

4.6 Conclusions

In conclusion, we have measured a gate controlled heat flow through an *SET*, making it a gate tunable heat switch. The celebrated Wiedemann-Franz law is strongly violated, as soon as one moves away from the charge degeneracy point, turning on the strong $e - e$ interaction in the transport process. The heat-flow is found to be strongly nonlinear in the Coulomb-blockade regions. Our experimental observation agrees very well with the theory.

Chapter 5

Thermal and Thermoelectric Transport in a Quantum-Dot Junction

In this chapter we present the measurement of heat-flow and thermoelectric transport through a Quantum-Dot (*QD*) junction. Several experiments were performed during the thesis with different *QD* junctions, here we consider mainly three experiments with distinct results.

In the first part of the chapter (Sec. 5.1) we present a general characterization of the Gold nano-particles (*GNP*) made out of evaporated Au. It gives a general idea about how we extract different parameters of the QD, which is the starting point of every experiment with *QD* junction.

In the second part we present the measurement of heat balance through a *QD* junction in the presence of a finite bias and temperature gradient (Sec. 5.2). The *QD* acts as a *heat-valve* between the hot source and cold drain reservoir, operated by the gate voltage. At the gate-open state, whenever the heat flown out of the source exceeds the heat deposited by the Joule-heating at finite bias, a drop of the electronic temperature of the source from its equilibrium-gate-closed value is observed.

In the last part of this chapter we present two experiments for the thermoelectric transport though a *QD* junction in two different tunneling regimes. First, with a weakly coupled dot (Sec. 5.3) (with significant co-tunneling at the middle of the Coulomb diamonds) and second, with a strongly coupled dot with Kondo spin-correlation (Sec. 5.4).

5.1   Characterization of evaporated gold nanoparticles

In the experiment described in chapter 4, we have considered a *metallic-island*, where the electrons are subject to strong Coulomb interactions and as a consequence we have observed

a charging energy gap in the energy spectrum, but the dimensions of the island are still large enough compared to the wavelength of the electrons (typically <1 nm). Therefore the transport of electron is not coherent, the energy spectrum can be considered continuous, with a charging energy gap. Here in this chapter, we will consider an *island* whose dimensions are reduced down to few nano-meters, such that it is comparable to the wavelength of electrons. Then the electron transport is coherent. As a result, the continuous energy spectrum splits into few discrete energy levels, with a finite level spacing.
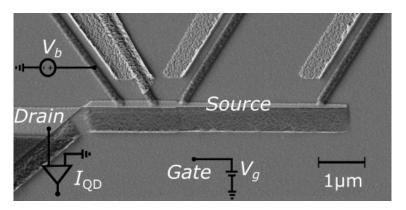
Fig. 5.1: **Charge transport circuit diagram** SEM image of sample with the circuit diagram for charge transport measurement. Any of the *SN* probes connected to the source can be used to bias the *QD* junction and the current is measured from the drain

We create these *QD*s by the deposition of Gold nano-particles (GNP). This can be done in several ways as described in Chapter 2 (Sec. 2.2.4). Here we choose the most reproducible method of nano-particle deposition, where a small amount of *Au* (1-2 nm thickness with a rate of about 0.02 *nm/s*) is evaporated, forming self-assembled nano-particles, which serve as *QD*s. Placing the *QD* at the nano-gap between the *source* and *drain* lead, created by electromigration, we fabricate a single *QD* transistor. A metallic plane underneath the hole sample separated by an approximately 8 nm thick Al_2O_3 oxide layer is used as *gate*. In addition, four superconducting *Al* leads are connected to the *source* via clean contact, which can be used either to probe the *QD*, heat the source island or to measure the temperature of the source island. For the details of fabrication refer to Chapter 2 (Sec. 2.2).

The circuit diagram for the electrical transport measurement is shown in Fig. 5.1, with an *SEM* image of the sample. We apply a bias voltage V_b on the *QD* junction from the one of the *SN* probes connected to the source and measure the current I_{QD} from the drain, as a function of the voltage applied on the gate, V_g. The conductance of the junction is measured using a lock-in amplifier. A small AC modulation voltage of 10 μV, at frequency f of 77 Hz (not a multiple 50 to avoid 50 *Hz* noise) is applied on the *QD* junction, superimposed with the DC bias voltage. The resulting AC current through the junction, locked at the same

frequency f, is measured by a lock-in amplifier (Standford Research System, SR 830). In this way we directly measure the differential conductance dI_{QD}/dV_b of the QD junction. The lock-in measured stability diagram for the conductance of the QD junction is plotted in the $V_b - V_g$ plane, as shown in Fig. 5.2. The diamond shaped black region of zero conduction can
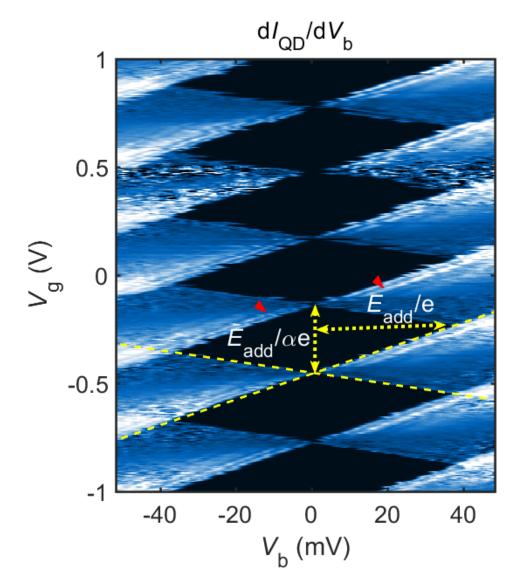
Fig. 5.2: **long range stability diagram of the QD made of evaporated Au NP** Conductance map of the QD in the bias and gate voltage plane. The Coulomb diamonds are identified as the black regions. Inside the conductive region some highly conductive bright lines can be observed, indicated by the red arrow-heads. These lines are the indication of quantization of energy of the QD. The extents of a diamond gives the amount of addition energy E_{add} needed to put an extra electron into the QD level.

be identified as the well known Coulomb diamonds, where the charge transport is blocked by the charging energy gap of the dot. As a broad picture, the stability diagram of the QD is

looking similar to that of the metallic island for the *SET* in chapter 2 (Fig. 4.2(d)), but if we look carefully into it, one can identify high conductance line structures (indicated by the red arrow heads) running in parallel to the edge of the Coulomb diamonds. These line structures in the conductance map indicate that the transport of electrons involves discrete electronic levels. This is the signature for energy quantization in the nano-particle.
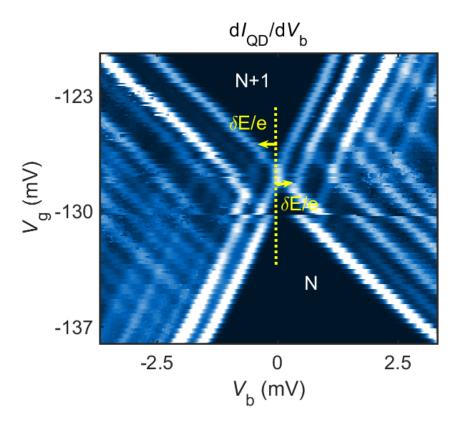
Fig. 5.3:   Resolved stability diagram of the *QD* made of evaporated Au NP   Zoomed conductance map of the *QD*, showing that the electronic levels are very well separated and resolvable

From the analysis of the conductance map in Fig. 5.2 we can extract the parameters for the *QD* device using the formalism described in Sec. 1.1.3. By looking at the two-slopes of the diamonds we can see that the corresponding slopes are similar for each diamond, hence within the gate voltage range (± 1 V) shown in Fig. 5.2, we have probed the charge transport through a single nano-particle only. The charge conductance for some gate voltage range shows unstable behavior (for example the diamond at $V_g = 0.5$ V), this is probably due to the electrostatic switches by the nearby nano-particles. The positive and negative slopes of the diamonds are found to be (according to Eq. (1.25)) $\beta = 0.169$ and $\beta' = 0.385$ respectively. These two slopes gives the estimation of the asymmetry in capacitance between source and drain using Eq. (1.26) as, $C_d/C_s = 1.88$, which is reasonable for a *QD* junction depending on the structure of the electromigration nano-gap between source and drain. The gate coupling

Table 5.1: The parameters of the studied QD

E_c (meV)	β	β'	$\alpha(\%)$	C_d/C_s
18	0.169	0.385	11.7	1.88

factor or the *lever-arm* can be estimated using Eq. (1.27) as, $\alpha = 11.7\%$, matching well with the *QD* devices with similar thickness of gate oxide layer [66]. The gate coupling factor in these devices usually varies from 1% to 30%. From the extents of the Coulomb diamonds along both axes (as indicated in Fig. 5.2), the charging energy of the *QD* can be found to be $E_c \approx 18$ meV, matching well with a nano-particle diameter of 8-10 nm, which is the average dimension of evaporated nano-particles reveled by *SEM* images (Sec. 2.2.4). From the estimation of the charging energy and the two slopes, the capacitances are found to be $C_g = 5.22 \times 10^{-19}$ F, $C_d = 2.56 \times 10^{-18}$ F and $C_s = 1.35 \times 10^{-18}$ F. All these parameters are matching very well with the previously studied similar *QD* devices [66, 155].

The line-structures in the conductance map corresponding to the single *QD* levels are not very clearly resolvable in Fig. 5.2 due to the coarse measurement. But these are clearly visible in the zoomed and resolved conductance map shown in Fig. 5.3. From this conductance map we can find the level-spacing between the *QD* levels. The level spacing between the ground-state and the first excited-state is obtained directly from the map (see Sec. 1.1.3) as $\delta E \approx 130 \, \mu eV$, which is much larger than the thermal energy $k_B T_e \approx 8 \mu eV$ at the operating temperature $T_e = 80$ mK, so that it is possible to resolve the *QD* levels. Different parameters of the *QD* studied are listed in the Table. 5.1.

The above described experiment of charge transport through a *QD* junction made of evaporated *Au* nano-particles gives a good example for characterization of a *QD* junction.

In the following sections, we will present the three main experiments with *QD* junctions, where, in addition to the charge-transport we will also consider thermal originated transport. As the parameters for the *QD* junctions varies from device to device, we have to characterize the specific device at the beginning of each experiment by performing charge transport though it. The extracted parameters from the charge transport will be useful for analyzing the thermoelectric measurements.

5.2 Exp 1: A gate tunable quantum dot heat valve

In this section we will discuss about an experiment where a single-*QD* level is used as a *heat valve* between two electronic reservoirs kept at different temperatures. By tuning the *QD* level with the help of the applied gate voltage we manipulate the heat flow though the *QD* junction. We measured the temperature of the source as a function of bias and gate voltage

and found Coulomb-diamond shapes in the electronic temperature map. A low temperature region (w.r.t gate-closed temperature) is observed in the temperature map at the gate-open and zero bias condition, indicating the thermalization of the hot source through the *QD* level. At a small but finite bias, the thermalization of the source through the *QD* level is compensated by the Joule-heating produced by the tunneling of electrons and the temperature of the source is found to be close to its equilibrium value. With the increase of bias, Joule-heating overrides the thermalization through *QD* and a overheated region is found in the temperature map.

5.2.1   Device Preparation

The device fabrication processes are very similar to that in the previous section, with some modifications in the design, that the constriction is made out of Pt deposited at a different angle, in order to avoid proximity induced superconductivity on the source lead.

We prepared the full device with a narrow metallic *Pt* constriction, which is connected on one side to a narrow metallic rectangular *Au* structure (the *Source*) and on the other side to a bulky metallic *Au* lead (the *Drain*). The source side is integrated with its local *SNS* thermometer and heater. All the structures are placed on top of a metallic back gate. After that a 1-2nm of *Au* is evaporated on top of the *as-made* sample to deposit the *Au NP*s on the unbroken sample and cooled-down in a highly filtered dilution refrigerator.

The lithographically made constriction is electromigrated at 4 K, under a high vacuum of 10^{-7} mbar. The conductance peaks in the *gate-traces*, measured at 4 K gives us initial indications for the presence of some nano-particles within the nano-gap between the *source* and *drain* formed by *EM*. With this confirmation we proceed for further low-temperature measurements.

5.2.2   Charge transport

To understand the characteristics of the *QD* junction we need to first study the charge transport through it. We perform the charge transport measurement at the bath temperature of 70 mK. The conductance of the *QD* junction is measured by a lock-in amplifier. The map of the conductance (converted into μS) in the $V_b - V_g$ plane is shown in Fig. 5.4. The highly conductive lines form the edges of Coulomb diamonds. Fine structures corresponding to the single electronic levels inside the conductive part of the diamonds are not resolvable, yet a drop of conductance within the two Coulomb edges gives a clear indication that the transport involves a single electronic level of the *QD*.

Using the same method as described in Sec. 5.1, we can extract the parameters of the *QD* junction. From the shape of the Coulomb diamonds one can notice that one edges is
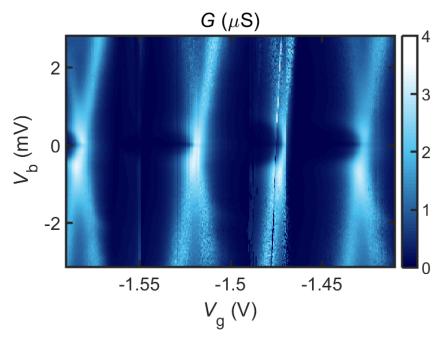
Fig. 5.4: Conductance map of the QD**: Exp 1** Stability diagram of the QD from the charge transport measurement. The QD coupling to the leads is strongly asymmetric. The single levels are not resolved in this map due to the strong coupling.

brighter than the other, this tells us that the coupling of the NP to the leads are strongly asymmetric. We can extract the effective tunneling rate, considering that the bottle-neck in tunneling is situated at the weakly coupled lead and therefore the total tunnel rate $\Gamma = \Gamma^l + \Gamma^r$, is given by that of the strongly coupled lead. It can be directly obtained from the width of the conductance peak at the brighter Coulomb edge. The tunnel coupling is extracted as $\hbar\Gamma \approx 170 \; \mu eV \equiv 40 GHz$, indicating a strong coupling of the QD and the lead. This strong coupling washed out the steps in the $I_{QD} - V_b$ characteristics and hence the fine structures in the conductive part of the Coulomb diamonds. The lever-arm of the gate can be extracted from the two slopes of the Coulomb diamonds (using Eq. (1.27)) as, $\alpha = 13$ %. Given the visible charge switches (probably due to nearby nanoparticles) and the striking similarities of the consecutive conductive regions, we cannot exclude that these are replicas of a single charge state. Assuming that they are real we find the charging energy of the QD to be $E_c = 4 \; meV$. Therefore, for this device, $k_B T < \Gamma < E_c$ and the single electronic level can not be consider as a sharp-resonant peak but rather a broadened Lorentzian shaped peak of width Γ.

5.2.3 Thermal transport

The measurement of thermal transport in the QD junction needs a very precise and sensitive thermometer, as one needs to measure a very small change in electronic temperature of

the lead as a result of the heat flow through the *QD*. We use the local *SNS* thermometer integrated with the *source* to measure its electronic temperature. We assume that the electronic temperature of the drain is that of the cryostat, as the drain is very well coupled to the bath temperature due to its large volume.
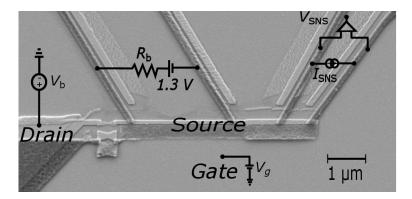
Fig. 5.5: **Circuit diagram for thermal transport**   SEM image of sample with the circuit diagram for thermal transport measurement. The longer *SNS* junction on the left used as heater of the Source and the shorter *SNS* junction on the towards the end of the source used as thermometer.

Characterization of the SNS thermometer and heater

The circuit diagram for thermal transport measurement is shown in Fig. 5.5. The shorter *SNS* junction (of length ≈ 700 *nm*) formed by the pair of *Al* leads towards the end of source is used as the thermometer. The $I - V$ characteristics of the *SNS* junction at the base temperature $T_b = 75$ *mK* is shown in Fig. 5.6 (a). The forward and backward $I - V$ traces show that the *SNS* junction has very little hysteresis, because, with a very small switching current of $I_c \approx$ 1.5 μA there is almost no overheating of the normal metal [122]. A statistics of the switching current is measured by plotting the histograms of 3000 switching events. This is done by biasing the *SNS* junction with an AC current and recording the switching by an oscilloscope, as described in detail in Sec. 3.3.4. The average of the histograms gives the most probable critical current of the junction. The thermometer is calibrated by measuring the average switching current as a function of the known bath temperature of the cryostat. A calibration curve of the thermometer is shown in Fig. 5.6 (b), including a fit with theory (Eq. (3.9)). By fitting of the calibration curve (I_c vsT_b) with theory (Eq. (3.9)), we get the estimate for the parameters of the junction including the diffusion constant $D = 49$ cm^2/s, the Thouless energy $\varepsilon_{th} = 13$ μeV, comparable to $k_B T_b$ at $T_b = 100$ *mK*. As result, a saturation of the average critical current is observed below 80 *mK* (Sec. 3.3.3). The saturation at such a low temperature may also be partly due to parasitic heating by noise.
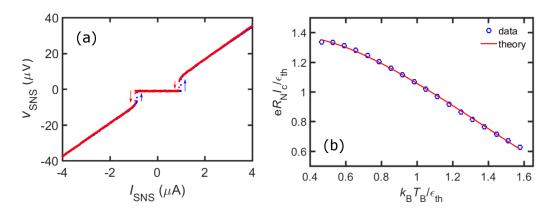
Fig. 5.6: Calibration of thermometer (a) A DC $I - V$ characteristics of the *SNS* thermometer at a bath temperature $T_b = 75\ mK$. The critical current of the junction can be found to be $\approx 1.5\ \mu A$. The forward (blue) and backward (red) traces shows that there is very little hysteresis. (b) Calibration of the *SNS* thermometer against the known bath temperature with the statistical measurement of the switching current of the junction. The calibration is done at an equilibrium condition of the source, without any external heating and bias voltage on the gate. A saturation in the calibration curve is found below 80 mK.

The relatively longer *SNS* junction (length $> 3\mu m$) on the source, closer to the constriction, has no super-current and hence it can be used as a heater governed by the Joule dissipation on the source island. The resistance of the heater junction is inferred from the normal state resistance of the thermometer junction (measured by four probe method) and from the dimensions of the heater junction, to be $R_H = 30\ \Omega$. The input heating power into the source therefore can be estimated as, $\dot{Q}_H = I_H^2 R_H$, where $I_H = (1.3/R_b)\ A$ is the heater bias current from a 1.3 V battery with a variable biasing resistor R_b.

Pure thermal transport

For a pure thermal transport one should ensure that there is no DC current flowing through the *QD*. For the measurement of pure thermal transport through the *QD*, we heat the source with a constant heating power so that source temperature T_e is higher than that of drain T_b and measure the temperature of the source as a function of the gate voltage, while the drain side remains floating. This ensures that in the steady state no flow of charge is possible and the transport is governed by the thermal gradient only. Since the spectral density of the *QD* has a highly broadened shape, one should expect a maximum heat-flow at the charge-degeneracy point [156] and hence a maximum drop of source-temperature (T_e) at the same gate voltage setting. But, in the experiment we do not measure any drop of T_e, rather we measured a rise (compared to its equilibrium value) whenever the gate voltage passes through the charge degeneracy value. One possible way to interpret this observation is the effect of noise. When

the drain lead remains floating it catches noise from the electromagnetic environment, which can act as an effective AC bias on the *QD* junction. Therefore, whenever we make the junction conductive by setting the gate voltage to charge degeneracy value, a flow of charges occurs between the source and drain. The Joule heating due to this current deposits some heat power on the source and hence increases the temperature. Another possible explanation could be that the drain is not purely floating, for example due to a small leakage to the gate, which applies an effective bias between the drain and source. So we conclude that, a *pure heat transport* measurement is not possible with this sample unless one gets rid of these issues.
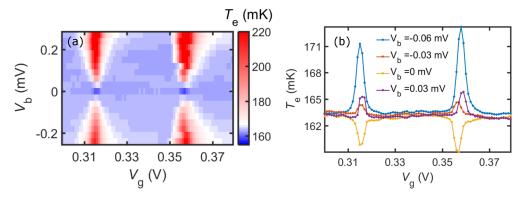
Fig. 5.7:   **Coulomb blockaded temperature map**   (a) Map of the *source* electronic temperature, when it is heated by constant DC heating power $\dot{Q}_H \approx 6 \ fW$ (estimated from the DC heating current and resistance of the heater junction), while the *drain* is assumed to at a bath temperature $T_b = 80 \ mK$. A Coulomb blockade structure is observed in the electronic temperature. As a result of the heating, *source* temperature is measured to be $(T_e)_{n_g=0} \approx 164mK$ in the Coulomb blockaded regions, where there is almost no flow of heat through the *QD*. While, at the charge degeneracy one can observe a range of the bias over which the cooling of the *source* is measured due to the opening of the heat valve between the hot *source* and cold *drain*. Just above and below the zero bias, the heat produced by the Joule dissipation at the barrier compensates the cooling and hence a temperature equal to the gate-closed value is observed. At large bias, the Joule heating dominates and an overheating is observed. (b) Few individual gate traces of the temperature around the zero bias.

Mixed charge and thermal transport

In order to solve the above problem we define the potential of the drain, by applying a small bias. This fixes the potential of the leads to a definite value.

We measure the temperature of the source as a function of the applied bias and gate voltage while the source side is heated by a constant DC heating power of $\dot{Q}_H \approx 6 \ fW$ (estimated from the DC heater bias current and resistance of the heater junction) from an isolated DC current source and the drain side is assumed to be at a bath temperature $T_b = 80$

mK. The measured electronic temperature of the source is plotted in the $V_b - V_g$ plane in Fig. 5.7 (a). The individual gate-traces of the electronic temperature of the source are shown in Fig. 5.7 (b).
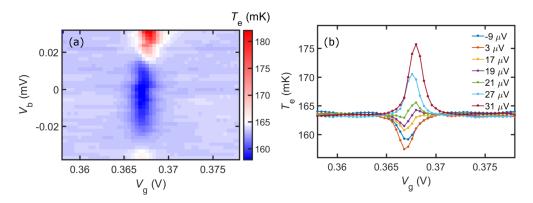
Fig. 5.8:   Resolved temperature map   (a) A better resolved map of the *source* electronic temperature near zero bias, with the similar measurement condition as in Fig. 5.7. The cooling region at the charge degeneracy point, over a certain range of bias above and below zero-bias, is clearly visible. While at a finite but small bias the source temperature is measured to be equal to gate-closed value, due to the balance of heat flow through the *QD* with the heat produced by the tunneling electrons. On further increase of bias an over heated region is measured in the conductive part of the Coulomb-map. (b) Few individual gate traces of the temperature around the zero bias.

To interpret this observation, let us first consider the zero bias line. At gate closed positions, for example in the Fig. 5.7 (a), 0.33 *V* < V_g < 0.35 *V*, V_g <0.31 *V* or V_g >0.36 *V*, we assume that there is no heat-flow though the *QD*. We measured a steady-state equilibrium temperature of the source $(T_e)_{n_g=0} = 164$ *mK*. This temperature increase is determined by the balance between heat-input by the heater and the heat-output by the $e - ph$ relaxation. At this zero-bias condition when we tune the gate voltage to degeneracy point, for example in the Fig. 5.7 (a), V_g =0.32 *V* and 0.36 *V*, the flow of heat through the *QD* becomes possible and the hot-source tends to thermalize to the cold-drain. Therefore we measured a drop of the temperature to $(T_e)_{n_g=0.5} = 159$ *mK* $< (T_e)_{n_g=0}$. This demonstrates a gate tunable heat flow through the single-*QD* level at zero-bias.

However, at finite applied bias on the *QD*, a usual Joule-heating is produced upon tunneling of electrons, this heating power is deposited (partly) on the source. Therefore, at the gate-open, finite bias condition, there are both thermalization of the source by the heat flow through the *QD* level and heating (w.r.t gate-closed temperature) by the Joule-power upon tunneling of electrons. The heat-flow and hence the thermalization is determined by the thermal conductance of the *QD* junction. So the heat flow is always constant at a fixed temperature difference ΔT, but the Joule-heating by the current increases with the bias. At a certain small but finite bias, the thermalization is compensated by the heating and we

measured the temperature equal to the gate-closed value. This feature of the temperature map is clearly visible in Fig. 5.8 (a), where the measurement conditions were similar to that of Fig. 5.7. Further increase in bias produces more heating, in this high bias regime Joule heating dominates over the thermalization and hence we found an overheated region with very high temperature.

Therefore, as a broad picture, the temperature maps show Coulomb diamond features with a low temperature region at charge degeneracy point around the zero bias, an overheated region for the conducting part of the diamond and an equilibrium temperature region at the middle of the diamonds where the transport is blocked by the charging energy gap. For a weakly coupled dot ($\hbar\Gamma \ll k_B T$) one expect to see refrigeration in the Coulomb blockaded area, due to the filtering of the high energy electrons by the charging energy gap [157, 158]. But here we do not see this effect probably due to the strong coupling of the *QD* with the leads.

We analyze the map in the following way: for the zero bias line in the map, at the *gate-closed* condition, we assume that there is no flow of heat through the *QD* i.e., $\dot{Q}_{QD} = 0$. Therefore the input heat $\dot{Q}_H$ from the heater makes a balance with the heat flown out via $e-ph$ coupling $\dot{Q}_{e-ph}$. Any parasitic heat loss $\dot{Q}_0$ (for example through the *NS* leads) is included in $\dot{Q}_H$ for simplicity. The steady state heat balance equation at the gate-closed state is given by,

$$\dot{Q}_H - \dot{Q}_{e-ph} = 0. \tag{5.1}$$

Solving the above heat balance equation with the use of measured steady state temperature $T_e = 164 \; mK$, and a bath temperature is at $T_b = 80 \; mK$, we get the relevant parameters of the device such as the the $e-ph$ coupling parameter $\Sigma = 2.4 \times 10^9 \; Wm^{-3}K^{-5}$, close to the expected value for *Au* [62] and the volume of the source island $\mathcal{V} = 2 \times 10^{-20} \; m^3$.

At a finite bias and arbitrary gate position the heat-balance equation reads,

$$\dot{Q}_H - \dot{Q}_{e-ph} - \dot{Q}_{QD} + \dot{Q}_{Joule} = 0, \tag{5.2}$$

where $\dot{Q}_{QD}$ is the heat-flow through the *QD* and $\dot{Q}_{Joule}$ is the Joule-heat power.

Solving the above equation, with a model for heat-flow in the limit of an *SET* [13] and the previously obtained sample parameters, we can extract the electronic temperature of the source. Fig. 5.9 shows such a map of the extracted electronic temperature. Strikingly, even though the model considers an *SET* with parameters (such as charging energy E_c, tunnel resistance R_T) similar to that of the sample, it captures the broad picture of the temperature map (Fig. 5.8(a)). But, it can not explain some of the detailed features, such as the edges of the cooling region are not properly aligned to the heating region (see Fig. 5.8 (a), near $V_b =$

$0.02\,mV$), therefore a temperature gradient inversion is observed in the individual gate traces, for example near $V_b = 20\,\mu V$ in fig. 5.8 (b). A better analysis of this observation is ongoing.
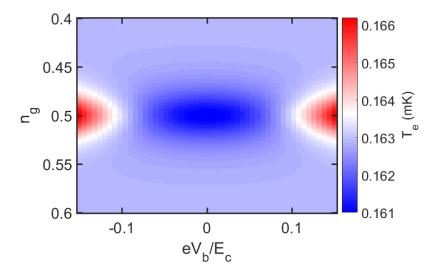
Fig. 5.9:   **Simulated electronic temperature of the source**   The calculated temperature of the source island of the *QD* junction solving the heat balance equation (Eq. (5.2)). The unknown sample parameters are extracted by solving the gate closed heat balance equation (Eq. (5.1)). A model for heat-flow in the *SET* limit is used [13].

Contrarily, solving the above heat balance equation (Eq. (5.2)), with the measured electronic temperature T_e and the sample parameters, one can extract the heat flow through the *QD* at small bias and the heat dissipation by the tunneling electrons at very high bias. The latter analysis is incomplete at the moment.

This experiment of heat transport provide us the way of measuring a heat flow in a *QD* junction at finite bias. Such an experiment combined with charge transport can be useful for demonstrating a *QD* heat engine and to measure its efficiency. The experiment can also give a quantitative estimation of Joule dissipation due to the tunneling of electrons in an isolated island. This produced probably the first Coulomb-blockaded electronic temperature map.

5.3 Exp 2: Thermoelectric transport in a weakly coupled QD

Here we present the measurement of the thermopower of a weakly coupled *QD* junction by measuring its thermo-electric current response. We also introduce, to the best of our knowledge, a new method for measuring the thermovoltage.

5.3.1 Device preparation

All the initial steps of device fabrication are same as described in the Sec. 5.2. The main difference in the fabrication process compared to the previous is that the electromigration of the constriction was done at room temperature in an ambient condition. After the formation of a nano-gap between source and drain by the electromigration, 1-2 nm of *Au* is evaporated on top of the electromigrated sample in order to graft a *Au* nano-particle within the *EM* gap (for details of fabrication refer to Sec. 2.2).

As the *EM* and the *NP* evaporation were done before putting the sample into the cryostat, we had a chance of choosing the *good* devices by measuring the tunnel resistance between source and drain. For this particular device in this discussion, we found a drop of tunnel resistance from about a few *G*Ω to 5 *M*Ω, before and after *NP* evaporation. This gives an indication that some *NP*s are bridging the gap between the source and drain. We then cooled down the sample in a dilution refrigerator for low temperature measurements.

5.3.2 Charge transport

Before going to the thermoelectric transport measurements, one needs to first characterize the *QD* by measuring the $I-V$ characteristics of the junction in the similar way as discussed in Sec. 5.1. For the charge transport measurement, a voltage bias is applied from the source side while the current through the *QD* junction is measured from drain, as a function of the gate voltage. The conductance of the junction is measured using a Lock-In amplifier. The circuit diagram is similar to the one shown in Fig. 5.1. The $I-V$ characteristics of the *QD* junction for a constant gate voltage corresponding to the charge degeneracy is shown in Fig. 5.10 (a) and a stability diagram for differential conductance of the *QD* junction is shown in Fig. 5.10 (b). By analyzing the conductance map in a similar manner as described in Sec. 5.1, we can extract all the parameters of the QD.

The positive and negative slopes of the Coulomb diamond are obtained as $\beta = 0.254$, $\beta' = 0.448$. The gate coupling factor is found to be $\alpha = 16.2$ %, comparable to the device with similar gate structure. The asymmetry in the capacitance of the dot to the source and drain is $C_\mathrm{d}/C_\mathrm{s} = 1.32$, comparable to the *QD* device discussed in the previous section. For this particular *QD* only one charge degeneracy point is observed within our accessible gate voltage range, therefore an exact estimation of the charging energy E_c is not possible. The lower limit of the charging energy is approximately given as $E_\mathrm{c} \approx 200$ meV. The three capacitances are estimated as $C_\mathrm{g} = 6.5 \times 10^{-20} F$, $C_\mathrm{d} = 1.9 \times 10^{-19} F$, $C_\mathrm{s} = 1.45 \times 10^{-19} F$, matching very well with similar devices. If carefully looked one can identify many line structures inside the conductive region of the conductance map. Out of these, the faint
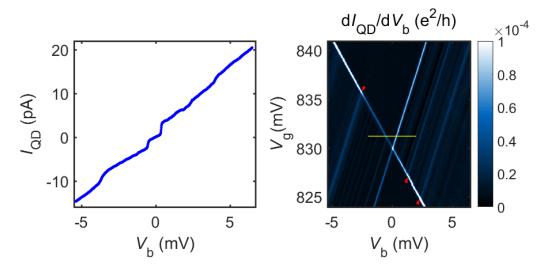
Fig. 5.10: Conductance map of the *QD*: Exp 2   (a) Current-Voltage characteristics of the *QD* junction along the yellow line shown in (b) at a fixed gate voltage $V_g = 831.2\ mV$, the step height for positive and negative currents allow us to estimate the two tunnel rates. (b) Stability diagram for differential conductance of the *QD* junction. The differential conductance is calculated from the measured I_{QD} vs V_b curves at different gate voltages. Due to the very high charging energy E_c (> 200 meV) of the *QD*, only one charge degeneracy point is observed at $V_g \approx 830$ mV, separating two charge states. The black contrast regions are the Coulomb blockaded area. The bright lines separate the blockaded region from the conductive region forming the Coulomb diamond edges. Inside the conductive region some bright lines (indicated by red arrow-head) are observed, these lines correspond to the quantized single levels of the *QD*. Beside these lines some other regularly spaced line structures can also be found in this conductive region, these could be attributed to the vibrational modes of the *QD*

and very closely spaced structures could be attributed to the vibrational or other bosonic modes present in the *QD* and the brighter line structures are identified as the single quantized levels of the dot. Therefore, from the conductance map we can see that there are two lines corresponding to the single electronic levels ending up at the Coulomb edge of the charge state $(N+1)$ with a level spacing between the ground state and the first excited state of $\delta E_{N+1} = 2.55\ meV$. Similarly we can see two lines corresponding to the two electronic levels ending up at the Coulomb edge of the charge state N. The level spacing between ground and first excited state for this charge state is $\delta E_N = 1.34$ meV.

    The curve for I_{QD} vs V_b can be used to determine the tunneling rates of electrons through the two tunnel junctions using Eq. (1.28). The step in current for positive and negative bias voltage are directly obtained from the curve as $I_+ = 2.61$ pA and $I_- = 1.52$ pA. The tunneling rates for the two junctions are found to be [25], $\Gamma^l = 10.1$ MHz and $\Gamma^r = 84.9$ MHz. For this *QD* device $\hbar\Gamma \ll k_B T$, it can be considered in the weak coupling regime.

$E_c^{\min}$ (meV)	β	β'	$\alpha(\%)$	C_d/C_s	Γ^l (MHz)	Γ^r (MHz)
200	0.254	0.448	16.2	1.32	10.1	84.9

All the parameters obtained from the charge transport measurement are listed in Table 5.2

5.3.3   Thermoelectric transport

In the previous section we have measured the current though the *QD* junction in the presence of a voltage bias, but the temperature of the *source* and *drain* leads were equal. Therefore the generated current is purely due to the applied voltage bias. Here we consider the situation when a finite temperature difference is applied across the *QD* in addition to the voltage bias.

We measure the current response in the *QD* junction as a function of bias and the gate voltage, with a constant temperature gradient across it. The circuit diagram for this
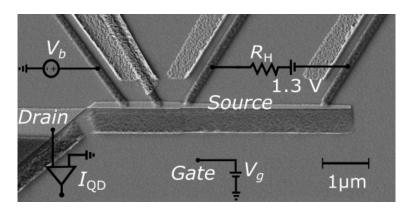
Fig. 5.11:   Thermoelectric transport circuit diagram   SEM image of sample with the circuit diagram for thermoelectric transport measurement. The longer *SNS* junction on the right side is used as heater of the Source and another *SN* probe on the left side is used to bias the QD junction while the current is measured from Drain.

measurement is shown in Fig. 5.11. The longer *SNS* junction ($> 3\mu m$) on the source island is used as a heater, driven by an isolated DC current source (a 1.3 V battery with a variable biasing resister R_H). The small volume of the source island decouples it from the bath at low temperature, therefore we can heat it up above the bath temperature. While the drain is assumed to be well coupled to the bath due to its large volume. So the temperature of drain is assumed to be always equal to the bath temperature. In this way we create a constant temperature difference between the source and drain in the steady state. A voltage bias V_b is

applied from another *Al* probe and the current is measured from drain side, as function of the applied bias voltage and the gate voltage.
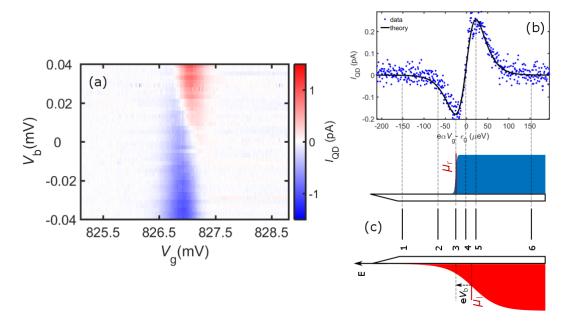
Fig. 5.12:   **Thermocurrent response of the QD**   (a) The map of the thermocurrent of the *QD* junction as a function of bias voltage V_b and gate voltage V_g, measured at the base temperature $T_b \approx 70\ mK$, with a constant heating power $\dot{Q}_H \approx 0.3\ pW$ on the source (estimated from the DC heating current and resistance of the heater junction). Interestingly, the positive current part of the diamond enters into the negative bias region and same is true for the negative current part of the Coulomb-diamond. (b) A line-cut of the thermocurrent map at a constant bias close to $V_b = 0$. The black line is the fit of the data with the linear response theory, using the temperature of the leads as free parameters. The temperature of the source and drain leads obtained from the fit are $T_s = 235\ mK$ and $T_d = 143\ mK$. (c) The transport mechanism through the *QD* in the presence of a finite temperature and voltage bias across it. With application of the gate voltage one can manipulate the position of the *QD* level. Different positions of a single *QD* level are shown by the numbers. The shape of measured thermocurrent can be explained by the position of the single level.

Fig. 5.12 (a) shows the map of the current in the $V_g - V_b$ plane, measured at a bath temperature $T_b = 70\ mK$, with a constant heating current of $I_H \approx 100\ nA$ on the source. One interesting feature of the current map to notice is that the apex of the positive current part of the Coulomb diamond (red) is not aligned with the negative current part (blue) (unlike a usual Coulomb-diamond, for example Fig. 5.10), rather they run in parallel for some range of bias voltage, i.e. the measured current has both positive and negative sign for some bias voltages. A line trace of the map at a constant bias voltage slightly below $V_b = 0\ V$ is shown in Fig. 5.12 (b), the black line gives the fit of the data with a linear response theory, using the temperature of the leads as free parameters (theoretical help from Paolo Erdman is acknowledged). The temperature of the source and drain lead found from the fit are $T_s = 235$

mK and $T_d = 143 \; mK$. The fitted value of T_s matches very well with a rough estimate. But we find a deviation of fitted value of T_d from the bath temperature T_b. This could be due to the thermal cross-talk between source and drain through the substrate phonons. This shows that assuming T_d not to be affected by the heating on source is probably not totally correct, especially for very high heating power.

Fig. 5.12 (c) shows the mechanism of the transport with a single *QD* level. Let us consider a finite bias between the hot-source and the cold-drain lead. With the application of the gate voltage we can move the *QD* level reversibly along the energy axis. First at the position 1, the level is far away from the Fermi-level of both of the leads, hence a zero current is observed. When the level is at the position 2, the high energy electrons from the hot source lead can tunnel and produce a negative current against the applied bias voltage (considering the absolute value of the electronic charge), with a maximum in the same direction until the level hits the Fermi-level of the cold-drain lead at position 3. With further increase of gate voltage, the level enters within the bias-window (eV_b) and a usual transport from drain to source with a positive current starts to contribute. At the charge degeneracy point, indicated by 4, the level is at the middle of the bias-window, the two currents compensate each other and the net current becomes zero. With the particle-hole symmetry we can get the opposite picture when the level goes below the bias window. For example at the position 5, the current become maximum in the positive direction, due to the dominated flow of electrons from clod-drain to the empty hole-states of the hot-source lead. With further increase in gate voltage the level goes deep inside the Coulomb-diamond and the current become zero again, e.g. at position 6.

The fitting of the thermocurrent data gives a good idea about the electronic temperature of the two leads and can be used as an intrinsic thermometer. We can use this technique to determine the temperature difference between the source and drain, independent of an external thermometer.

Thermovoltage measurement Scheme

The thermovoltage is defined as the potential difference between the hot and cold reservoir, in the absence of DC charge current, that arises due to the temperature gradient between them. Therefore the measurement of thermovoltage of a *QD* junction requires the measurement of open-circuit voltage of a high-impedance device.
This is experimentally challenging because:

- it is difficult to have the drain purely floating.

- no voltmeter has infinite input impedance. Therefore it may shunt the thermovoltage when the device impedance goes very high.

- the equilibration times to reach the true zero-current state at such high impedances can be extremely long.

As a result one may never measures the full amplitude of the thermovoltage of the device.

Here we describe a, to the best of our knowledge, new way of measuring the thermovoltage in a high impedance junction. Our measurement protocol is the following, for each fixed value of the gate voltage, we sweep the bias voltage and measure the full $I(V)$ characteristics (Fig. 5.13). Therefrom, we can define $-V_{\text{Th}}$ as the bias voltage at which the current goes through zero, realizing thus perfect open-circuit conditions. The line-shape of the extracted thermovoltage is shown by black dots on the same figure.
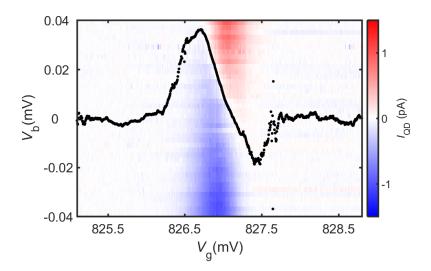
Fig. 5.13: Thermovoltage of a QD junction determination of thermovoltage directly from the measurement of the thermocurrent in a *QD* junction (Fig. 5.12). The negative-thermovoltage $(-V_{\text{Th}})$ is defined, at each gate position, as the applied bias voltage where the measured current is zero, thereby achieving a perfect open-circuit condition. The black line shows the gate voltage dependent line-shape of the thermovoltage in the *QD* junction.

5.3.4 Thermopower

The thermopower *S*, also known as the *Seebeck Coefficient*, is defined as the negative-thermovoltage $(-V_{\text{Th}})$ generated per unit temperature difference (ΔT),

$$S = -\frac{V_{\text{Th}}}{\Delta T} \tag{5.3}$$

Therefore, from the knowledge of the temperature gradient between the source and drain
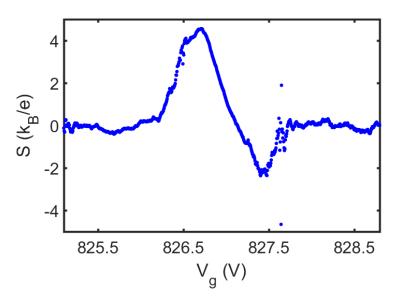
Fig. 5.14: Gate voltage dependence of the thermopower Thermopower S of the QD junction is plotted with the gate voltage, measured at a bath temperature $T_b = 70~mK$. It is extracted from the thermovoltage data, normalized with the temperature difference $\Delta T = 92~mK$ between the source and drain lead, determined by the fitting of thermocurrent data with linear response theory as described before.

one can extract the thermopower of the QD junction, using the measured thermovoltage. By fitting the measured thermocurrent data with linear response theory, we extracted the temperature of the two sides and hence ΔT. Fig. 5.14 shows the plot of thermopower in the QD junction as a function of the gate voltage.

According to Eq. (1.60) (Fig. 1.11) for a QD with an estimated charging energy $E_c \approx 200$ meV, one should expect a huge thermopower signal, with an amplitude of $> 1000~k_B/e$. But in experiment we have measured an amplitude of $S_{max} \sim 4k_B/e$, this indicates that there are co-tunneling involved in the transport. From the thermocurrent vs V_g curve (Fig. 5.12) we obtain that the crossover from sequential to co-tunneling regime occurs at a cross-over energy $\Delta_c \approx 4k_B T$, where the thermocurrent starts to reduce from its maximum value due to the presence of co-tunneling processes. The expected maximum value of the thermopower in the co-tunneling regime is (using the Eq. (1.59)) $|S_{max}| = \Delta_c/eT = 4k_B/e$. Therefore, the measured amplitude of the thermo-power signal matches very well with the expected value in the co-tunneling regime.

5.4 Exp 3: Thermopower of a Kondo-correlated QD

In this section we will describe thermoelectric transport measurements in a *Kondo correlated QD* junction. The thermopower of a weakly coupled *QD* in the sequential tunneling regime exhibits a periodic sawtooth line-shape with a period of electronic charge *e* [7]. The effect of co-tunneling reduces the amplitude of the thermopower as soon as one goes away from the charge degeneracy, but the period sill remains *e* [9]. We found a distinct feature of the thermovoltage of a Kondo-correlated *QD* that, in contrast to the sequential and co-tunneling regime, the thermovoltage line-shape exhibits a 2e periodicity. Further, the signal changes sign as the temperature is increased, in agreement with theory [58].

5.4.1 Charge transport

The conductance of the *QD* junction is measured as a function of the bias and gate voltage using a Lock-in amplifier as described before. Fig. 5.15 (a) shows the map of the conductance of the *QD* junction. We observed three charge states within the accessible gate voltage range of $\sim \pm 5$ V, which corresponds to a single *QD* coupled to the leads. One can notice the conductance-ridge at zero bias for the alternating Coulomb-diamonds, this is the well known signature for the charge conductance of a Kondo spin-correlated *QD* junction.

The Kondo-resonance in the conductance of a *QD* junction appears when the dot is oddly occupied, so that it acts as a magnetic impurity in the system. Therefore from the position of the Kondo-ridge in the conductance map we can identify the even and odd charge states of the dot. The odd sectors of the Coulomb-blockade map are situated at $V_g < -4$ V and $V_g = -1.2$ to 3.5 V, while the even sectors are at $V_g = -3.8$ to -1 V and $V_g > 4$ V. A better resolved conductance map near $V_g = -4$ V is shown in Fig. 5.15 (b). The structure of the Coulomb-diamond and the zero bias conductance-ridge is clearly visible in this map. The conductance near charge-degeneracy point at $V_g = 3$ V appears very unstable, this can be due to the electrostatic-switches by the nearby particles.

In the gate voltage range $V_g = 0.5$ to 1 V, i.e., at the middle of the blockaded region of the strongly coupled Kondo-dot, we observed a much weaker conductance response. We attribute this to another *QD*, coupled to the leads in parallel. We refer this as the weakly coupled dot.

Here we are interested in the thermoelectric-characterization of the Kondo-coupled dot, therefore we can use the current response of weakly coupled dot as a tool for measuring the temperature of the leads of the *QD* junction (in the absence of a reliable thermometer), as described in the preceding section.
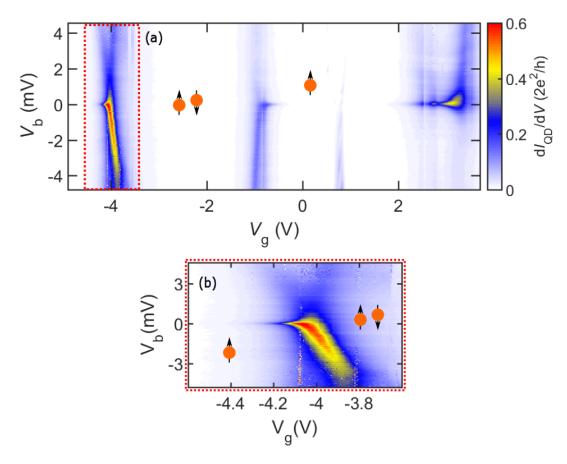
Fig. 5.15: Conductance map of the Kondo-correlated QD (a) Conductance map plot of the Kondo-correlated QD junction in the $V_b - V_g$ plane. The odd sector of the diamond can be easily identified from the position of the conductance ridge, as $V_g < -4\,V$ and $V_g = -1.2$ to $3.5\,V$. The even sector of the diamonds are situated at $V_g = -3.8$ to $-1\,V$ and $V_g > 4\,V$. The even and odd regions are indicated by the cartoon of two opposite spin electron and a single electron, respectively. (b) A resolved conductance map for the degeneracy point near $V_g = -4\,V$.

The parameters of the Kondo-coupled QD are extracted from the conductance map. From the two slopes of the diamond we get the capacitive asymmetry between the source and drain $C_d/C_s = 0.35$, the gate coupling factor $\alpha < 1\,\%$ and the charging energy of the dot $U = 2E_c \approx 58\,meV$. Such a small gate coupling factor compared to the previous experiments, could be due to the screening effects of the strongly coupled lead to the QD. The relative contrast in the conductance map of the two Coulomb-edges (Fig. 5.15 (b)) indicate a strong asymmetry in the tunnel coupling of the QD to the leads. Therefore we can consider the total tunnel rate $\Gamma = \Gamma^l + \Gamma^r$ to be governed by the more strongly coupled lead. The tunnel coupling Γ can be extracted from the width of the conductance peak at the Coulomb-edge corresponding to the more strongly coupled lead. This is done by fitting the conductance

peak with a Lorentzian function, the estimated value of total tunnel coupling is $\hbar\Gamma \approx 2.6$ *meV*, which is equivalent to a thermal energy at $T \approx 3$ K.

Characterization of Kondo-effect: The Kondo spin-singlet between the unpaired electron in the dot and the conduction electrons in the lead forms below the characteristic Kondo temperature (T_K) [33]. We characterize the Kondo effect in the *QD* junction in two different ways, first, by measuring the Kondo-resonance peak as a function of temperature and second, by measuring the splitting of the Kondo-resonance with the application of a magnetic field [159]. The Kondo-resonance is very sensitive to the temperature, it decreases with
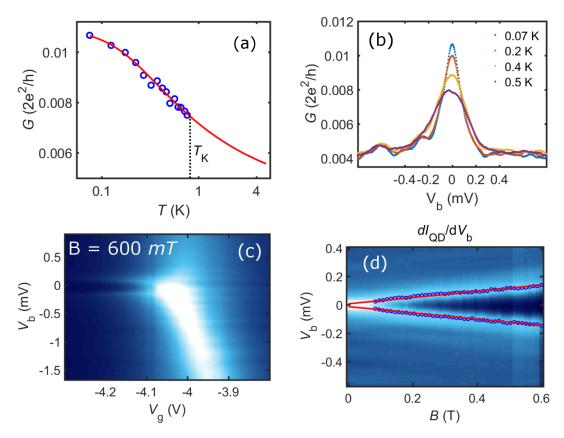
Fig. 5.16: Characterization of Kondo effect (a) The Kondo-conductance peak with temperature at a fixed gate voltage $V_g = -0.295\ V$, $|\Delta V_g| = 0.575\ V$ away from the nearest degeneracy point in Fig. 5.15. Red curve is the fit of the data with the *NRG* theory given by Eq. (5.4), using T_K and Γ^l/Γ^r as fitting parameters and a constant finite-bias background conductance $G_c = 0.004(2e^2/h)$ (as seen in (b)). The extracted Kondo temperature at this gate voltage is $T_K = 0.819\ K$. (b) Bias trace of the conductance at different temperatures. Finite-bias conductance gives the value of G_c. (c) Splitting of the Kondo-peak in the presence of a constant magnetic field B = 600 mT, (d) Map of the Kondo-peak conductance with bias and magnetic field, Kondo-peak splits at a critical magnetic field and splitting increases with magnetic field.

increasing temperature. The value of the conductance at the resonance-peak reduces with

temperature. One can extract the Kondo-temperature by fitting the temperature dependence of the conductance at the Kondo-resonance with the empirical formula given in Eq. (1.32) based on the *NRG* theory [35]:

$$G(T) = G_1 \left(\frac{T^2}{T_k^2} \left(2^{1/s} - 1 \right) + 1 \right)^{-s} + G_c \qquad (5.4)$$

where $G_1 = \frac{2e^2}{h} \frac{4\Gamma^l \Gamma^r}{(\Gamma^l + \Gamma^r)^2}$ is the saturated value of the Kondo-conductance peak in the low temperature regime. In the case of a symmetric coupling of the *QD* to the leads $\Gamma^l = \Gamma^r$, therefore $G_1 = 2e^2/h = G_0$, the quantum of conductance. But for an asymmetric tunnel coupling only a fraction of the G_0 is achieved in the zero temperature limit, since the Kondo-resonance develops only with the strongly coupled lead while other lead acts as a probe. G_c is the background conductance at a finite bias due to the direct tunneling or conduction through a highly resistive shunt across the *QD* junction. Here, $s = 0.22$ for spin-1/2 Kondo-effect.

The Kondo-temperature is defined as the temperature at which the Kondo-conductance peak value is reduced to 50 % of the conductance peak at the lowest temperature [43]. Using the above formula, $G(T_k) = G_1/2 + G_c$. Fig. 5.16(a) shows the evolution of the Kondo-conductance peak with temperature at a fixed gate voltage $V_g = -0.295$ V (on the scale of Fig. 5.15). The red solid-curve shows the fitting of the data with Eq. (5.4), using T_K and Γ^l/Γ^r as the fitting parameters and a constant background conductance at finite bias, $G_c = 0.004(2e^2/h)$. From the fitting we found an estimate for the Kondo temperature of the *QD* junction at the same gate position as $T_K = 0.819$ K and a tunnel coupling asymmetry $\Gamma^l/\Gamma^r = 0.002$, indicating a strongly asymmetric coupling between the *QD* and the leads.

Another, but less precise way to determine the Kondo temperature is by perturbing the Kondo state with the application of a magnetic field. When the applied magnetic field can provide a sufficient Zeeman-splitting energy to split the electronic level, the degeneracy of the level is lifted. The asymmetry between the two spin states start to suppress the Kondo-correlation. As a result the Kondo-resonance peak splits with increasing magnetic field. A large splitting of the Kondo peak at a fixed magnetic field $B = 600$ mT is shown in Fig. 5.16 (c). The splitting develops beyond a critical magnetic field B_c so that $g\mu_B B_c = 0.5 k_B T_K$, where μ_B is the Bohr magneton and g is the Landé g-factor (note that this scale T_K differ by a numerical prefactor from the Kondo scale determined above using the temperature dependence of the zero-bias conductance). We measured the conductance of the *QD* junction as a function of the bias and the magnetic field at a fixed gate voltage. The conductance of the *QD* junction at a constant gate voltage, with varying magnetic field and bias is plotted in Fig. 5.16 (d). The splitting of the Kondo resonance peak is resolved at a magnetic field $B_c \approx 60 mT$. In addition, since splitting of the level is proportional to the applied bias at large

bias, it can be fitted with a linear equation, $eV_b = g\mu_B B$. The fitted red lines in Fig. 5.16 (d) give an estimate of the Landé g-factor. $g = 3.6$, that is somewhat larger than what is usually found in gold nanoparticles. Using the measured critical field that is necessary to split the Kondo resonance, we deduce from this procedure an approximate estimate of the Kondo temperature $T_K \approx 300$ mK, that is of the same magnitude but somewhat smaller than the Kondo scale extracted from the temperature dependence.

5.4.2 Thermoelectric transport

We now move to the thermoelectric characterization of the Kondo-coupled *QD*. We have performed thermoelectric experiments by providing three different constant heating power to the source island, leading to three device temperatures, labeled $T_{\text{low}} < T_{\text{mid}} < T_{\text{high}}$. The thermal experimental conditions of the three measurements (as shown in Fig. 5.19) are summarized in Table 5.3.

Table 5.3: Heating conditions and bound estimates on the device temperatures for the measurements in Fig. 5.19

Exp	$T_{cryostat}$ (K)	$\dot{Q}_H$ (nW)	T_{source} (K)
T_{low}	0.075	0.001	≤ 0.4
T_{mid}	0.075	2.7	~ 1.5
T_{high}	4.2	2.7	~ 4.4

Estimate of the device temperatures

The related experimental source temperatures and thermal gradients under which the thermoelectric measurements have been carried out cannot be controlled independently in the experiment, as they depend on the thermalization process of the device under the applied heating. In particular, the temperatures of the source island, are not precisely known.

Here we nevertheless propose a realistic modeling of the thermal balances and the ensuing values of the three above-discussed temperatures. The comparison of the amplitude of the thermopower data to calculations, as discussed in the next section, can be used to estimate the temperature gradients ΔT occurring in each of the three data sets. A comprehensive thermal analysis common to all three temperatures is quite involved because the hierarchy of the dominant heat transport mechanisms out of a nanodevice such as ours changes dramatically in the 0.1 to 5 K range. The different channels entering the heat balance are summarized in Fig. 5.17. In the steady state, the (experimentally known) heat load $\dot{Q}_H$ to the source is compensated by the heat flowing out, either mainly through the electron or the
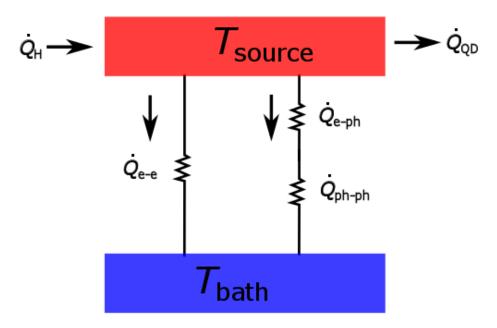
Fig. 5.17: Thermocurrent in the Kondo-correlated QD   Schematics summarizing the thermal balance of the source island. The heating power $\dot{Q}_H$ is known and the heat flow $\dot{Q}_{QD}$ across the quantum dot junction is negligible. The two competing heat drain mechanisms are electronic conduction ($\dot{Q}_{e-e}$)and by phonons. In the latter case, the thermal bottleneck can be either the electron-phonon coupling ($\dot{Q}_{e-ph}$) or the boundary resistance between the source island and the substrate ($\dot{Q}_{ph-ph}$).

phonon channel. The electron heat channel involves electronic conduction through the four aluminum leads (the heat conduction through the QD is negligible). At temperatures below 200 mK, this power $\dot{Q}_{e-e}$ is exponentially suppressed owing to the superconducting gap in Al, and becomes rapidly negligible. Yet, already above 300 mK, $\dot{Q}_{e-e}$ starts dominating the power exchanged by electron-phonon coupling $\dot{Q}_{e-ph}$ and tends to a Wiedemann-Franz type behavior $\dot{Q}_{e-e} = (L_0/2R_N^{lead}) \times (T_{source}^2 - T_{bath}^2)$. Here, one can assume to a good approximation $L_0 = 2.4 \times 10^{-8}$ WΩK^2. R_N^{lead} represents the effective normal state resistance of the leads up to some region which can be considered a thermal reservoir at T_{bath}. This resistance is however difficult to quantify. In order to put some numbers, let us assume that the 4 Al wires in parallel lead to an effective $R_N^{lead} \approx 10\Omega$.

     The power exchanged via the phonon heat channel is generally modeled by $\dot{Q}_{e-ph} = \Sigma \mathscr{V} \left(T_{source}^5 - T_{bath}^5\right)$, with the interaction volume $\mathscr{V}$ given by the geometrical volume of the source island, and the electron-phonon interaction constant in gold $\Sigma = 2.4 \times 10^9$ W.m^{-3}.K^{-5}. This coupling increases extremely fast ($\propto T^5$) as temperature is increased, such that above a few Kelvin, the electron and phonon temperatures are no longer distinct in a given experimental volume. The bottleneck for the phononic heat drain is then rather at the boundary between the phonons in the source and the substrate. This so-called Kapitza resistance, associated to impedance mismatch of the respective phonon species, leads to a thermal power

flow frequently modeled by $\dot{Q}_{\mathrm{ph-ph}} = \kappa A \left(T_{source}^4 - T_{bath}^4 \right)$, involving the interface area A (geometrical surface imprint of the source island on the substrate) and the Kapitza coefficient κ. This coefficient depends both on the materials involved and the interface quality; let us take a value measured for the Cu-SiO2 interface, $\kappa = 45 \text{ pW}\mu\text{m}^{-2}\text{K}^4$.

At the lowest experimental temperature T_{low}, which we anticipate to be of about 300 mK from the qualitative comparison of the thermovoltage data with theory, $\dot{Q}_{\mathrm{e-ph}}$ is clearly contributing significantly to the heat evacuation from the source. Nevertheless, $\dot{Q}_{\mathrm{e-e}}$ is definitely also contributing but the extent of the latter is difficult to quantify: the electronic thermal conductance of the superconducting leads allows thermal leaks into the aluminum leads, from which heat is drained to the phonons. This can in some cases be described by an effective e-ph interaction volume $\mathcal{V}^* > \mathcal{V}$. By keeping only the e-ph contribution in the heat balance equation, one finds $T_{source} = 460$ mK. This is evidently an upper bound. With a three times larger effective interaction volume due to the heat leakage to the leads, T_{source} is reduced to about 350 mK, which is consistent with the estimation of T_{low}.

At the intermediate experimental temperature T_{mid}, which we anticipate to be of about 1 K from the qualitative comparison of the thermovoltage data with theory, superconductivity in the aluminum must be weakened to the point that we can neglect it (superconductors are only thermal insulators well below their T_c). In this temperature regime one finds $\dot{Q}_{\mathrm{e-ph}}$ and $\dot{Q}_{\mathrm{e-e}}$ to be quite comparable assuming the above numerical estimates. We thus solve $\dot{Q}_{\mathrm{H}} = \dot{Q}_{\mathrm{e-e}} + \dot{Q}_{\mathrm{e-ph}}$, which leads to $T_{\mathrm{mid}} = 1.5$ K.

The highest experimental temperature T_{high} can be anticipated to be only slightly larger than 4.2 K, both from the qualitative comparison of the thermovoltage data with theory and because sizeable thermal gradients with respect to $T_{bath} = 4.2$ K are now very difficult to realize. At these temperatures, the interface resistance-limited phonon heat flow is the main heat drain mechanism, we thus write $\dot{Q}_{\mathrm{H}} = \dot{Q}_{\mathrm{ph-ph}}$. As expected, this highly simplified modeling leads to $T_{\mathrm{high}} = 4.4$ K, that is, 0.2 K above the bath temperature.

Thermovoltage

The thermovoltage of the *QD* junction, at these three different constant heating conditions, are measured using the same method as described in the sec. 5.3.3. The measurement circuit is same as shown in Fig. 5.11. Fig. 5.18 shows the plot of the measured thermocurrent of the device as a function the applied bias and gate voltage, in the presence of a constant temperature difference at the source temperature T_{mid}. One interesting feature of the current map can be noticed in this plot that, unlike the thermocurrent of the weakly coupled *QD* in Sec. 5.3.3 (Fig. 5.13), the positive current part of the Coulomb-diamond (red) enters inside the negative bias region and pierces the negative current part into two. For the consecutive
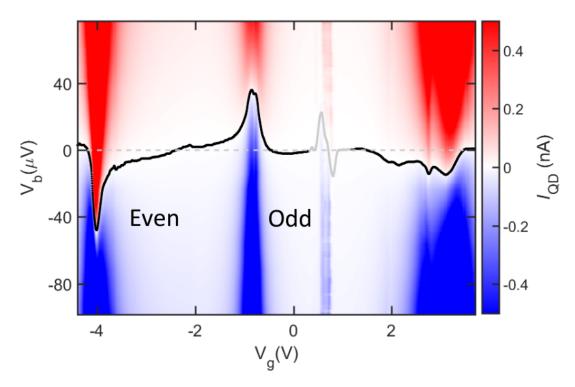
Fig. 5.18: Thermocurrent in the Kondo-correlated QD Current map for small applied biases in the presence of a temperature gradient at intermediate temperature $T_{\mathrm{mid}} = 1.5$ K. The black line follows the points of vanishing current; it is thus equal to $-V_{\mathrm{Th}}$. The thermoresponse at about $V_g = 0.7$ V, associated with the second, weakly coupled quantum dot, is grayed out for better readability.

degeneracy points the opposite effect is found, i.e., negative current part of the Coulomb-diamond pierces the positive current region. This feature qualitatively differs from the line-shape of the thermovoltage signal of the weakly-coupled *QD*. The black dotted line in Fig. 5.18 gives the zero-current line trace of the current map, which shows the gate-voltage dependence of the negative-thermovoltage of the Kondo-correlated *QD* junction. As discussed above, the gate voltage region, $V_g = 0.5$ to 1 V, associated to the weakly coupled *QD* is grayed out for better readability of the Kondo-feature. The measured thermovoltage changes sign completely between two consecutive degeneracy points, with a same sign for every second degeneracy point. This results a $2e$ periodic thermovoltage signal, twice the period of the thermovoltage in a weakly coupled *QD*.

Thermopower

The thermopower of the Kondo-coupled *QD* junction is obtained by normalizing the measured thermovoltage with the applied temperature difference between the source and drain (Eq.

(5.3)). The proximized *SNS* junction on the source could be in principle used to measure the temperature of the lead, but it was not available for this device due to the loss of one micro-bonding connection during cool-down. However, the proximity *SNS* junction thermometer operates only at a temperature <1 *K*. Therefore in any case the *SNS* thermometer is not useful in this experiment for high temperature measurements. We have used the above estimated device temperature and the corresponding temperature difference to extract the thermopower.

Temperature dependence of the Kondo-correlated thermopower

The 2*e* periodicity of the thermopower signal gives an indication for the presence of the Kondo-resonance in the spectral-density for oddly occupied states of the dot and its asymmetry around the Fermi-energy within the energy-range of $k_B T$, but it can not give a clear information whether the *QD* is in pure Kondo-regime or in the mixed-valance regime. An almost similar behavior was observed in a *QD* in the mixed-valance regime [161]. Therefore, a 2*e* periodic thermopower signal is not a foolproof evidence of Kondo effect in a *QD*. To understand this better we have extended our study of thermopower in the Kondo-correlated *QD* junction by measuring the distinct gate voltage dependent thermopower signal at different device temperatures. Fig. 5.19 shows the gate-evolution of the thermopower of the Kondo-correlated *QD* at the above discussed three different device temperatures, $T_{\text{low}} = 300$ mK (blue), $T_{\text{mid}} = 1.5$ K (orange) and $T_{\text{high}} = 4.4$ K (red). The degeneracy point near gate voltage $V_g \approx 3$ *V* is not shown here, due to its unstable nature it is not possible to do a quantitative analysis in this region. A comparison of the data with the theoretical calculation based on Eq. (1.66) (performed by Theo Costi) is also presented.

One can easily identify a clear sign change of the thermopower between the three temperatures, in the oddly occupied diamonds, e.g. at $V_g = -0.5$ *V* and $V_g = -4.24$ *V*, indicated by the arrow-heads, while in the *even* region there is no sign change. This is in agreement with the theory curves, where it is shown segment wise, due to the limitation of the single-orbital model.

The above observed sign change of the thermopower in the Kondo regime can be interpreted in the following way: at very low temperature $T \ll T_K$, the Kondo resonance is nicely developed and the Kondo-peak is situated slightly above the Fermi-energy (E_F), as a result the slope of the spectral function (within the energy-range $k_B T$ w.r.t E_F) is negative and hence the thermopower is positive (using Eq. (1.66)), e.g. for the device temperature T_{low}. Now, as one increases the temperature, e.g. to T_{mid}, the Kondo-peak starts to get reduced. Therefore the slope of the spectral-function is also reduced and so the thermopower. At very high temperature $T_{\text{high}} > \hbar\Gamma/10k_B$, the Kondo resonance vanishes completely and the
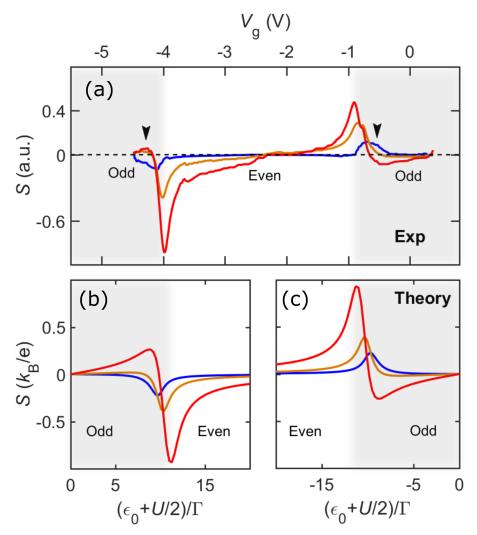
Fig. 5.19: Temperature dependence of the Kondo-correlated Thermopower (adapted from Dutta et al. [160]) (a) Experimental thermopower $S = -V_{\text{Th}}/\Delta T$ at the three experimental device temperatures $T_{\text{low}} = 300$ mK $= 0.01\Gamma$ (blue), $T_{\text{mid}} = 1.5$ K $= 0.05\Gamma$ (orange), and $T_{\text{high}} = 4.4$ K $= 0.14\Gamma$ (red). The arrows highlight the level depths in the Kondo regime near which the thermopower changes sign at a temperature $T1 \approx \Gamma/(10k_{\text{B}})$. (b,c) Corresponding *NRG* calculation using experimental parameters $U = 58$ meV, $\Gamma = 2.6$ meV and for the same set of temperatures T/Γ (with the same color code). The calculation assumes a single orbital level, predicting therefore correctly $S = 0$ in the center of an oddly occupied Coulomb diamond ($\varepsilon_0 + U/2 = 0$). For the sake of comparison with the experimental data, the calculations at negative $\varepsilon_0 + U/2$ are placed to the right-hand panel. Neglecting higher orbital levels in the *NRG* calculation does not allow to map the complete transition region in the center of the even diamond so that the theoretical comparison is done using two disjointed panels.

spectral weight shifts towards the closest resonance level. As a result the slope of the spectral function changes sign and hence the thermopower.

Our observation thus confirms the theoretical predictions for the sign-change of thermopower in the Kondo-regime [35, 58] and establishes that the Kondo-resonance peak is not exactly situated at the Fermi energy, but it can be shifted by of the order of $k_B T_K$.

5.5   Conclusions

In conclusion, in this chapter about the experiments with QD junctions in different coupling regime, we have presented the measurement of thermal balance and heat flow through a QD junction. We introduced a new way of measuring thermovoltage, that is much more reliable to achieve the open-circuit condition, the main requirement for thermovoltage measurement by definition. The measurement of thermopower gives a good idea about the spectral function of a QD junction, especially for the Kondo-correlated QD, which confirmed that the Kondo-resonance in our system not always pinned to the Fermi-level but can be slightly off by the presence of asymmetry in level position. Our measurement of thermopower of the Kondo-correlated QD with temperature, confirms the theoretical prediction for the sign change of the thermopower above a characteristics temperature $T_1 \approx \hbar\Gamma/10k_B$ [58]. The physical meaning of this energy scale T_1 is not totally clear to us, neither it is to its author, Theo Costi (private communication). Efforts for a more quantitative understanding are on the way.

Conclusions

In this thesis we have studied the thermal and thermoelectric transport in an isolated nano-structure starting from a sub-micron metallic island down to few-atomic sized quantum dot. The transport is strongly modified by the Coulomb-interactions and the quantum coherence.

The presence of Coulomb interactions in the isolated metallic island in an *SET* introduces a charging energy gap in the transport processes. This charging energy gap acts as a filter to admit only the high energy electrons which could pay the required charging energy. Therefore, the successfully transported electrons carry a heat more than what one naively expects in a normal situation. This causes a violation of the Wiedemann-Franz law as one go away from the charge degeneracy point. As a consequence we measured a non-linear heat flow through the *SET* in the Coulomb-blockade region.

We have presented the measurement of heat flow through a single *QD* level. This acts as a heat valve between two heat reservoirs operated by the gate voltage. At zero bias on the *QD* junction, we found the thermalizaion of the hot source to the drain by the heat-flow through the *QD* level. The 'zero-bias' line of this experiment is essentially equivalent to the experiment of thermal conductance measurement in an *SET*. Here we extended our study to the finite bias regime for a *QD* junction. Indeed, at finite bias the source is overheated by the Joule heating produced by the tunneling electrons. This experiment gives us a way to measure the dissipation due to the tunneling of electron. The Joule heating compensates the cooling of the source through the *QD* at a finite bias and we measured a temperature equal to the steady state gate-closed value.

The measurement of thermopower requires the measurement of the thermovoltage in the open-circuit condition. Experimentally achieving such a perfect open circuit condition is very difficult due to the finite impedance of a voltmeter. We have presented a new way of measuring the thermovoltage in a close to open-circuit condition, by measuring the current through the highly resistive junction. The measurement of thermopower in the weakly coupled *QD* junction matches very well with the previous theoretical and experimental studies, that the signal exhibits an *e* periodicity in the gate-induced charge and the presence

of significant co-tunneling reduces the amplitude of the thermopower signal in the Coulomb-blockade region.

The thermoelectric transport is modified a lot in the presence of spin-correlation. The spin-correlation between the oddly occupied electrons in the *QD* and the conduction electrons gives rise to the Kondo-resonance peak in the density of states of the *QD*. The previous studies of the Kondo-effect based on the measurement of electrical conductance could only measure the amplitude of the Kondo-resonance but they could not give a precise position of the Kondo-resonance peak. Therefore, one common concept exists that the Kondo-resonance is always pinned to the Fermi level of the leads. We have presented the measurement of the thermopower of Kondo correlated *QD* junction. The 2*e* periodic behavior of the measured thermopower signal, compared to *e* period in a weakly coupled dot, already hints about the position of the Kondo-resonance slightly off from the Fermi level. Our further study of temperature dependence of the Kondo-correlated thermopower confirms it.

We have faced some difficulties in the thermal transport experiment with the *QD* junctions. In this thesis we were not able to probe a *pure thermal transport* (i.e. transport processes driven by thermal gradient only) through a single *QD* level. The difficulties appeared in making the *drain* of *QD* junction fully floating. This could be due to a significant gate-leakage on the drain side. The chances of gate-leakage can be feasible, as we placed the full device on top of the gate, in order to achieve an on chip rf filtering. A small gate-leakage to the drain due to it huge overlap with the gate may not be negligible. One could probably improve this by redefining the gate so that it has very small overlap with the leads of the device.

There are few interesting experiments that can be done as an perspective of these studies, such as:

The *QD* junction can be operated as a heat engin. Since the *QD* junctions integrated with properly optimized *SNS* thermometer and heater are now easily accessible, one can use these *QD* junction as a heat engine by combining the heat and charge transport measurements. Due to the selective particle exchange between the two heat reservoirs through the resonant level of the *QD*, the efficiency of the *QD* heat engine is expected to be very high, close to the fundamental thermodynamic limits.

The *QD* junction can be used as a refrigerator. Choosing a proper coupling strength and tuning of the *QD* level properly with respect to the Fermi level of the leads, one can use it to filtered out the high energy electrons from one lead to the other, thereby achieving a refrigeration of the same.

Publications

- B. Dutta, J. T. Peltonen, D. S. Antonenko, M. Meschke, M. A. Skvortsov, B. Kubala, J. König, C. B. Winkelmann, H. Courtois, J. P. Pekola, *Thermal Conductance of a Single-Electron Transistor*, Phys. Rev. Lett. **119**, 077701 (2017), Editors' Suggestion Featured in Physics Synopsis: Transistor Breaks Law of Thermal Conductivity

- B. Dutta, D. Majidi, A. G. Corral, P. A. Erdman, S. Florens, T. A. Costi, H. Courtois, C. B. Winkelmann, *Direct Probe of the Seebeck Coefficient in a Kondo-Correlated Single-Quantum-Dot Transistor*, Nano Lett., **2019**, 19 (1), 506–511.

- B. Dutta et al. *Energetics with a Single-Quantum-Dot Transistor*, in preparation.

- P. A. Erdman, J. T. Peltonen, B. Bhandari, B. Dutta, H. Courtois, R. Fazio, F. Taddei, J. P. Pekola, *Non-Linear Thermovoltage in a Single-Electron Transistor*, arXiv.1812.06514.

References

[1] G. Benenti, G. Casati, K. Saito, and R. Whitney, "Fundamental aspects of steady-state conversion of heat to work at the nanoscale," *Physics Reports*, vol. 694, pp. 1 – 124, 2017.

[2] G. J. Snyder and E. S. Toberer, "Complex thermoelectric materials," *Nature Materials*, vol. 7, pp. 105 EP –, Feb 2008.

[3] C. J. Vineis, A. Shakouri, A. Majumdar, and M. G. Kanatzidis, "Nanostructured thermoelectrics: Big efficiency gains from small features," *Advanced Materials*, vol. 22, pp. 3970–3980, Jul 2010.

[4] A. I. Hochbaum, R. Chen, R. D. Delgado, W. Liang, E. C. Garnett, M. Najarian, A. Majumdar, and P. Yang, "Enhanced thermoelectric performance of rough silicon nanowires," *Nature*, vol. 451, pp. 163 EP –, Jan 2008.

[5] M. Dresselhaus, G. Chen, M. Tang, R. Yang, H. Lee, D. Wang, Z. Ren, J. Fleurial, and P. Gogna, "New directions for low-dimensional thermoelectric materials," *Advanced Materials*, vol. 19, no. 8, pp. 1043–1053.

[6] D. V. Averin and K. K. Likharev, "Coulomb blockade of single-electron tunneling, and coherent oscillations in small tunnel junctions," *Journal of Low Temperature Physics*, vol. 62, pp. 345–373, Feb 1986.

[7] C. W. J. Beenakker and A. A. M. Staring, "Theory of the thermopower of a quantum dot," *Phys. Rev. B*, vol. 46, pp. 9667–9676, Oct 1992.

[8] D. Boese and R. Fazio, "Thermoelectric effects in kondo-correlated quantum dots," *EPL (Europhysics Letters)*, vol. 56, no. 4, p. 576, 2001.

[9] M. Turek and K. A. Matveev, "Cotunneling thermopower of single electron transistors," *Phys. Rev. B*, vol. 65, p. 115332, Mar 2002.

[10] B. Kubala and J. König, "Quantum-fluctuation effects on the thermopower of a single-electron transistor," *Phys. Rev. B*, vol. 73, p. 195316, May 2006.

[11] M. Tsaousidou and G. P. Triberis, "Thermal conductance of a weakly coupled quantum dot," *AIP Conference Proceedings*, vol. 893, no. 1, pp. 801–802, 2007.

[12] X. Zianni, "Coulomb oscillations in the electron thermal conductance of a dot in the linear regime," *Phys. Rev. B*, vol. 75, p. 045344, Jan 2007.

[13] B. Kubala, J. König, and J. Pekola, "Violation of the wiedemann-franz law in a single-electron transistor," *Phys. Rev. Lett.*, vol. 100, p. 066801, Feb 2008.

[14] Y. I. Rodionov, I. S. Burmistrov, and N. M. Chtchelkatchev, "Relaxation dynamics of the electron distribution in the coulomb-blockade problem," *Phys. Rev. B*, vol. 82, p. 155317, Oct 2010.

[15] B. Sothmann, R. Sánchez, and A. N. Jordan, "Thermoelectric energy harvesting with quantum dots," *Nanotechnology*, vol. 26, no. 3, p. 032001, 2015.

[16] L. D. Hicks, T. C. Harman, and M. S. Dresselhaus, "Use of quantum-well superlattices to obtain a high figure of merit from nonconventional thermoelectric materials," *Applied Physics Letters*, vol. 63, no. 23, pp. 3230–3232, 1993.

[17] M. Josefsson, A. Svilans, A. M. Burke, E. A. Hoffmann, S. Fahlvik, C. Thelander, M. Leijnse, and H. Linke, "A quantum-dot heat engine operated close to thermodynamic efficiency limits," *arXiv preprint arXiv:1710.00742*, 2017.

[18] G.-L. Ingold and Y. V. Nazarov, "Charge tunneling rates in ultrasmall junctions," in *Single charge tunneling*, pp. 21–107, Springer, 1992.

[19] K. K. Likharev, "Correlated discrete transfer of single electrons in ultrasmall tunnel junctions," *IBM Journal of Research and Development*, vol. 32, no. 1, pp. 144–158, 1988.

[20] D. Averin, "Kk likharev in mesoscopic phenomena in solids, edited by bl altshuler, pa lee, and ra webb," *Modem Problems in Condensed Matter Sciences*, 1991.

[21] C. W. J. Beenakker, "Theory of coulomb-blockade oscillations in the conductance of a quantum dot," *Phys. Rev. B*, vol. 44, pp. 1646–1656, Jul 1991.

[22] I. Kulik and R. Shekhter, "Kinetic phenomena and charge-discreteness effects in granulated media," *Zhur. Eksper. Teoret. Fiziki*, vol. 68, no. 2, pp. 623–640, 1975.

[23] J. M. Thijssen and H. S. J. Van der Zant, "Charge transport and single-electron effects in nanoscale systems," *physica status solidi (b)*, vol. 245, no. 8, pp. 1455–1470.

[24] L. P. Kouwenhoven, C. M. Marcus, P. L. McEuen, S. Tarucha, R. M. Westervelt, and N. S. Wingreen, "Electron transport in quantum dots," in *Mesoscopic electron transport*, pp. 105–214, Springer, 1997.

[25] E. Bonet, M. M. Deshmukh, and D. C. Ralph, "Solving rate equations for electron tunneling via discrete quantum states," *Phys. Rev. B*, vol. 65, p. 045317, Jan 2002.

[26] H. Grabert and M. H. Devoret, *Single charge tunneling: Coulomb blockade phenomena in nanostructures*, vol. 294. Springer Science & Business Media, 2013.

[27] S. De Franceschi, S. Sasaki, J. M. Elzerman, W. G. van der Wiel, S. Tarucha, and L. P. Kouwenhoven, "Electron cotunneling in a semiconductor quantum dot," *Phys. Rev. Lett.*, vol. 86, pp. 878–881, Jan 2001.

[28] A. E. Hanna, M. T. Tuominen, and M. Tinkham, "Observation of elastic macroscopic quantum tunneling of the charge variable," *Phys. Rev. Lett.*, vol. 68, pp. 3228–3231, May 1992.

[29] T. M. Eiles, G. Zimmerli, H. D. Jensen, and J. M. Martinis, "Thermal enhancement of cotunneling in ultra-small tunnel junctions," *Phys. Rev. Lett.*, vol. 69, pp. 148–151, Jul 1992.

[30] L. J. Geerligs, D. V. Averin, and J. E. Mooij, "Observation of macroscopic quantum tunneling through the coulomb energy barrier," *Phys. Rev. Lett.*, vol. 65, pp. 3037–3040, Dec 1990.

[31] W. de Haas, J. de Boer, and G. van dën Berg, "The electrical resistance of gold, copper and lead at low temperatures," *Physica*, vol. 1, no. 7, pp. 1115 – 1124, 1934.

[32] M. P. Sarachik, E. Corenzwit, and L. D. Longinotti, "Resistivity of mo-nb and mo-re alloys containing 1pp. A1041–A1045, Aug 1964.

[33] J. Kondo, "Resistance minimum in dilute magnetic alloys," *Progress of Theoretical Physics*, vol. 32, no. 1, pp. 37–49, 1964.

[34] K. G. Wilson, "The renormalization group: Critical phenomena and the kondo problem," *Rev. Mod. Phys.*, vol. 47, pp. 773–840, Oct 1975.

[35] T. A. Costi, A. C. Hewson, and V. Zlatic, "Transport coefficients of the anderson model via the numerical renormalization group," *Journal of Physics: Condensed Matter*, vol. 6, no. 13, p. 2519, 1994.

[36] T. A. Costi and A. C. Hewson, "Transport coefficients of the anderson model," *Journal of Physics: Condensed Matter*, vol. 5, no. 30, p. L361, 1993.

[37] D. Goldhaber-Gordon, H. Shtrikman, D. Mahalu, D. Abusch-Magder, U. Meirav, and M. A. Kastner, "Kondo effect in a single-electron transistor," *Nature*, vol. 391, pp. 156 EP –, Jan 1998.

[38] J. Appelbaum, "$s - d$ exchange model of zero-bias tunneling anomalies," *Phys. Rev. Lett.*, vol. 17, pp. 91–95, Jul 1966.

[39] A. F. G. Wyatt, "Anomalous densities of states in normal tantalum and niobium," *Phys. Rev. Lett.*, vol. 13, pp. 401–404, Sep 1964.

[40] P. W. Anderson, "Localized magnetic states in metals," *Phys. Rev.*, vol. 124, pp. 41–53, Oct 1961.

[41] J. R. Schrieffer and P. A. Wolff, "Relation between the anderson and kondo hamiltonians," *Phys. Rev.*, vol. 149, pp. 491–492, Sep 1966.

[42] M. Pustilnik and L. Glazman, "Kondo effect in quantum dots," *Journal of Physics: Condensed Matter*, vol. 16, no. 16, p. R513, 2004.

[43] D. Goldhaber-Gordon, J. Göres, M. A. Kastner, H. Shtrikman, D. Mahalu, and U. Meirav, "From the kondo regime to the mixed-valence regime in a single-electron transistor," *Phys. Rev. Lett.*, vol. 81, pp. 5225–5228, Dec 1998.

[44] L. Onsager, "Reciprocal relations in irreversible processes. *i.*," *Phys. Rev.*, vol. 37, pp. 405–426, Feb 1931.

[45] H. B. Callen, "The application of onsager's reciprocal relations to thermoelectric, thermomagnetic, and galvanomagnetic effects," *Phys. Rev.*, vol. 73, pp. 1349–1358, Jun 1948.

[46] H. B. Callen, "Thermodynamics and an introduction to thermostatistics," 1998.

[47] N. W. Ashcroft and N. D. Mermin, "Solid state physics (holt, rinehart and winston, new york, 1976)," *Google Scholar*, vol. 403, 2005.

[48] C. Kittel, P. McEuen, and P. McEuen, *Introduction to solid state physics*, vol. 8. Wiley New York, 1996.

[49] S. Lee, K. Hippalgaonkar, F. Yang, J. Hong, C. Ko, J. Suh, K. Liu, K. Wang, J. J. Urban, X. Zhang, C. Dames, S. A. Hartnoll, O. Delaire, and J. Wu, "Anomalously low electronic thermal conductivity in metallic vanadium dioxide," *Science*, vol. 355, no. 6323, pp. 371–374, 2017.

[50] J. M. Ziman, *Electrons and phonons: the theory of transport phenomena in solids*. Oxford university press, 2001.

[51] F. Curzon and B. Ahlborn, "Efficiency of a carnot engine at maximum power output," *American Journal of Physics*, vol. 43, no. 1, pp. 22–24, 1975.

[52] L.-D. Zhao, S.-H. Lo, Y. Zhang, H. Sun, G. Tan, C. Uher, C. Wolverton, V. P. Dravid, and M. G. Kanatzidis, "Ultralow thermal conductivity and high thermoelectric figure of merit in snse crystals," *Nature*, vol. 508, pp. 373 EP –, Apr 2014.

[53] A. A. M. Staring, L. W. Molenkamp, B. W. Alphenaar, H. van Houten, O. J. A. Buyk, M. A. A. Mabesoone, C. W. J. Beenakker, and C. T. Foxon, "Coulomb-blockade oscillations in the thermopower of a quantum dot," *EPL (Europhysics Letters)*, vol. 22, no. 1, p. 57, 1993.

[54] L. Molenkamp, A. A. M. Staring, B. W. Alphenaar, H. van Houten, and C. W. J. Beenakker, "Sawtooth-like thermopower oscillations of a quantum dot in the coulomb blockade regime," *Semiconductor Science and Technology*, vol. 9, no. 5S, p. 903, 1994.

[55] A. S. Dzurak, C. G. Smith, C. H. W. Barnes, M. Pepper, L. Martín-Moreno, C. T. Liang, D. A. Ritchie, and G. A. C. Jones, "Thermoelectric signature of the excitation spectrum of a quantum dot," *Phys. Rev. B*, vol. 55, pp. R10197–R10200, Apr 1997.

[56] R. Scheibner, E. G. Novik, T. Borzenko, M. König, D. Reuter, A. D. Wieck, H. Buhmann, and L. W. Molenkamp, "Sequential and cotunneling behavior in the temperature-dependent thermopower of few-electron quantum dots," *Phys. Rev. B*, vol. 75, p. 041301, Jan 2007.

[57] S. F. Svensson, A. I. Persson, E. A. Hoffmann, N. Nakpathomkun, H. A. Nilsson, H. Q. Xu, L. Samuelson, and H. Linke, "Lineshape of the thermopower of quantum dots," *New Journal of Physics*, vol. 14, no. 3, p. 033041, 2012.

[58] T. A. Costi and V. Zlatić, "Thermoelectric transport through strongly correlated quantum dots," *Phys. Rev. B*, vol. 81, p. 235127, Jun 2010.

[59] Y. Kawamura, K. Toyoda, and S. Namba, "Deep uv submicron lithography by using a pulsed high-power excimer laser," *Journal of Applied Physics*, vol. 53, no. 9, pp. 6489–6490, 1982.

[60] C. Vieu, F. Carcenac, A. Pépin, Y. Chen, M. Mejias, A. Lebib, L. Manin-Ferlazzo, L. Couraud, and H. Launois, "Electron beam lithography: resolution limits and applications," *Applied Surface Science*, vol. 164, no. 1, pp. 111 – 117, 2000.

[61] A. A. Tseng, K. Chen, C. D. Chen, and K. J. Ma, "Electron beam lithography in nanoscale fabrication: recent development," *IEEE Transactions on Electronics Packaging Manufacturing*, vol. 26, pp. 141–149, April 2003.

[62] F. Giazotto, T. T. Heikkilä, A. Luukanen, A. M. Savin, and J. P. Pekola, "Opportunities for mesoscopics in thermometry and refrigeration: Physics and applications," *Rev. Mod. Phys.*, vol. 78, pp. 217–274, Mar 2006.

[63] H. Courtois, S. Rajauria, P. Gandit, and et al., "Inherent thermometry in a hybrid superconducting tunnel junction," *J Low Temp Phys*, vol. 153, pp. 325 – 338, Dec 2008.

[64] P. Koppinen, T. Kühn, and I. Maasilta, "Effects of charging energy on SINIS tunnel junction thermometry," *J Low Temp Phys*, vol. 154, pp. 179 – 189, Mar 2009.

[65] J. P. Pekola, V. F. Maisi, S. Kafanov, N. Chekurov, A. Kemppinen, Y. A. Pashkin, O.-P. Saira, M. Möttönen, and J. S. Tsai, "Environment-assisted tunneling as an origin of the dynes density of states," *Phys. Rev. Lett.*, vol. 105, p. 026803, Jul 2010.

[66] D. Van Zanten, *Quantum dynamics revealed in weakly coupled quantum dot - superconductor turnstiles*. Theses, Université Grenoble Alpes, June 2015.

[67] F. Lecocq, I. M. Pop, Z. Peng, I. Matei, T. Crozes, T. Fournier, C. Naud, W. Guichard, and O. Buisson, "Junction fabrication by shadow evaporation without a suspended bridge," *Nanotechnology*, vol. 22, no. 31, p. 315302, 2011.

[68] E. Philofsky, "Intermetallic formation in gold-aluminum systems," *Solid-State Electronics*, vol. 13, no. 10, pp. 1391–1394, 1970.

[69] G. Clatterbaugh, J. Weiner, and H. Charles, "Gold-aluminum intermetallics: Ball bond shear testing and thin film reaction couples," *IEEE transactions on components, hybrids, and manufacturing technology*, vol. 7, no. 4, pp. 349–356, 1984.

[70] R. C. Blish, S. Li, H. Kinoshita, S. Morgan, and A. F. Myers, "Gold–aluminum intermetallic formation kinetics," *IEEE Transactions on Device and Materials Reliability*, vol. 7, no. 1, pp. 51–63, 2007.

[71] P. S. Ho and T. Kwok, "Electromigration in metals," *Reports on Progress in Physics*, vol. 52, no. 3, p. 301, 1989.

[72] H. Park, A. K. L. Lim, A. P. Alivisatos, J. Park, and P. L. McEuen, "Fabrication of metallic electrodes with nanometer separation by electromigration," *Applied Physics Letters*, vol. 75, no. 2, pp. 301–303, 1999.

[73] H. Park, J. Park, A. K. L. Lim, E. H. Anderson, A. P. Alivisatos, and P. L. McEuen, "Nanomechanical oscillations in a single-c60 transistor," *Nature*, vol. 407, pp. 57 EP –, Sep 2000.

[74] C. B. Winkelmann, N. Roch, W. Wernsdorfer, V. Bouchiat, and F. Balestro, "Super-conductivity in a single-c60 transistor," *Nature Physics*, vol. 5, pp. 876 EP –, Oct 2009.

[75] L. H. Yu and D. Natelson, "The kondo effect in c60 single-molecule transistors," *Nano Letters*, vol. 4, no. 1, pp. 79–83, 2004.

[76] N. Roch, S. Florens, V. Bouchiat, W. Wernsdorfer, and F. Balestro, "Quantum phase transition in a single-molecule quantum dot," *Nature*, vol. 453, pp. 633 EP –, May 2008.

[77] D. R. Strachan, D. E. Smith, D. E. Johnston, T.-H. Park, M. J. Therien, D. A. Bonnell, and A. T. Johnson, "Controlled fabrication of nanogaps in ambient environment for molecular electronics," *Applied Physics Letters*, vol. 86, no. 4, p. 043109, 2005.

[78] Z. M. Wu, M. Steinacher, R. Huber, M. Calame, S. J. van der Molen, and C. Schö-nenberger, "Feedback controlled electromigration in four-terminal nanojunctions," *Applied Physics Letters*, vol. 91, no. 5, p. 053118, 2007.

[79] M. Ben Haddada, J. Blanchard, S. Casale, J.-M. Krafft, A. Vallée, C. Méthivier, and S. Boujday, "Optimizing the immobilization of gold nanoparticles on functionalized silicon surfaces: amine- vs thiol-terminated silane," *Gold Bulletin*, vol. 46, pp. 335–341, Dec 2013.

[80] L. Bernard, M. Calame, S. J. van der Molen, J. Liao, and C. Schönenberger, "Controlled formation of metallic nanowires via au nanoparticle ac trapping," *Nanotechnology*, vol. 18, no. 23, p. 235202, 2007.

[81] S. I. Khondaker, K. Luo, and Z. Yao, "The fabrication of single-electron transistors using dielectrophoretic trapping of individual gold nanoparticles," *Nanotechnology*, vol. 21, no. 9, p. 095204, 2010.

[82] W. Liu, C. Wang, H. Ding, J. Shao, and Y. Ding, "Ac electric field induced dielectrophoretic assembly behavior of gold nanoparticles in a wide frequency range," *Applied Surface Science*, vol. 370, pp. 184 – 192, 2016.

[83] S. Kumar, S.-H. Yoon, and G.-H. Kim, "Bridging the nanogap electrodes with gold nanoparticles using dielectrophoresis technique," *Current Applied Physics*, vol. 9, no. 1, pp. 101 – 103, 2009.

[84] M. L. Li, S. L. Leung, Y. L. Qu, Z. L. Dong, and W. J. Li, "Dielectrophoretic assembly of 2 nm gold particles for nano-sensing applications," in *2010 IEEE 5th International Conference on Nano/Micro Engineered and Molecular Systems*, pp. 932–936, 2010.

[85] L. Bernard, *EXPANDING THE HORIZON VIA MOLECULAR ELECTRONICS OF NANOPARTICLE ASSEMBLIES*. Theses, University of Basel, Sept. 2006.

[86] K. I. Bolotin, F. Kuemmeth, A. N. Pasupathy, and D. C. Ralph, "Metal-nanoparticle single-electron transistors fabricated using electromigration," *Applied Physics Letters*, vol. 84, no. 16, pp. 3154–3156, 2004.

[87] F. Kuemmeth, *Quantum dynamics revealed in weakly coupled quantum dot - superconductor turnstiles*. Theses, Cornell University, Jan. 2008.

[88] G. C. O'Neil, D. R. Schmidt, N. A. Miller, J. N. Ullom, K. D. Iwrin, A. Williams, G. B. Arnold, and S. T. Ruggiero, "Progress in density of states measurements of al lightly doped with mn," *Journal of Low Temperature Physics*, vol. 151, pp. 70–75, Apr 2008.

[89] H. Jung, Y. Kim, K. Jung, H. Im, Y. A. Pashkin, O. Astafiev, Y. Nakamura, H. Lee, Y. Miyamoto, and J. S. Tsai, "Potential barrier modification and interface states formation in metal-oxide-metal tunnel junctions," *Phys. Rev. B*, vol. 80, p. 125413, Sep 2009.

[90] D. C. Ralph, C. T. Black, and M. Tinkham, "Spectroscopic measurements of discrete electronic states in single metal particles," *Phys. Rev. Lett.*, vol. 74, pp. 3241–3244, Apr 1995.

[91] R. C. Dynes, V. Narayanamurti, and J. P. Garno, "Direct measurement of quasiparticle-lifetime broadening in a strong-coupled superconductor," *Phys. Rev. Lett.*, vol. 41, pp. 1509–1512, Nov 1978.

[92] R. C. Dynes, J. P. Garno, G. B. Hertel, and T. P. Orlando, "Tunneling study of superconductivity near the metal-insulator transition," *Phys. Rev. Lett.*, vol. 53, pp. 2437–2440, Dec 1984.

[93] T. M. Eiles, J. M. Martinis, and M. H. Devoret, "Even-odd asymmetry of a superconductor revealed by the coulomb blockade of andreev reflection," *Phys. Rev. Lett.*, vol. 70, pp. 1862–1865, Mar 1993.

[94] H. Pothier, S. Guéron, D. Esteve, and M. H. Devoret, "Flux-modulated andreev current caused by electronic interference," *Phys. Rev. Lett.*, vol. 73, pp. 2488–2491, Oct 1994.

[95] J. M. Hergenrother, M. T. Tuominen, and M. Tinkham, "Charge transport by andreev reflection through a mesoscopic superconducting island," *Phys. Rev. Lett.*, vol. 72, pp. 1742–1745, Mar 1994.

[96] S. Rajauria, P. Gandit, T. Fournier, F. W. J. Hekking, B. Pannetier, and H. Courtois, "Andreev current-induced dissipation in a hybrid superconducting tunnel junction," *Phys. Rev. Lett.*, vol. 100, p. 207002, May 2008.

[97] M. Nahum, T. M. Eiles, and J. M. Martinis, "Electronic microrefrigerator based on a normal-insulator-superconductor tunnel junction," *Applied Physics Letters*, vol. 65, no. 24, pp. 3123–3125, 1994.

[98] A. V. Feshchenko, L. Casparis, I. M. Khaymovich, D. Maradan, O.-P. Saira, M. Palma, M. Meschke, J. P. Pekola, and D. M. Zumbühl, "Tunnel-junction thermometry down to millikelvin temperatures," *Phys. Rev. Applied*, vol. 4, p. 034001, Sep 2015.

[99] M. Nahum and J. M. Martinis, "Ultrasensitive-hot-electron microbolometer," *Applied Physics Letters*, vol. 63, no. 22, pp. 3075–3077, 1993.

[100] D. V. Anghel, A. Luukanen, and J. P. Pekola, "Performance of cryogenic microbolometers and calorimeters with on-chip coolers," *Applied Physics Letters*, vol. 78, no. 4, pp. 556–558, 2001.

[101] H. Pothier, S. Guéron, N. O. Birge, D. Esteve, and M. H. Devoret, "Energy distribution function of quasiparticles in mesoscopic wires," *Phys. Rev. Lett.*, vol. 79, pp. 3490–3493, Nov 1997.

[102] S. Rajauria, *Electronic refrigeration using superconducting tunnel junctions*. Theses, Université Joseph-Fourier - Grenoble I, Nov. 2008.

[103] B. Dutta, J. T. Peltonen, D. S. Antonenko, M. Meschke, M. A. Skvortsov, B. Kubala, J. König, C. B. Winkelmann, H. Courtois, and J. P. Pekola, "Thermal conductance of a single-electron transistor," *Phys. Rev. Lett.*, vol. 119, p. 077701, Aug 2017.

[104] A. Zaikin and G. Zharkov, "Theory of wide dirty SNS junctions," vol. 7, no. 3, pp. 184–185, 1981.

[105] P. Dubos, H. Courtois, B. Pannetier, F. K. Wilhelm, A. D. Zaikin, and G. Schön, "Josephson critical current in a long mesoscopic S-N-S junction," *Phys. Rev. B*, vol. 63, p. 064502, Jan 2001.

[106] H. Courtois, P. Gandit, D. Mailly, and B. Pannetier, "Long-range coherence in a mesoscopic metal near a superconducting interface," *Phys. Rev. Lett.*, vol. 76, pp. 130–133, Jan 1996.

[107] H. Courtois, P. Gandit, and B. Pannetier, "Proximity-induced superconductivity in a narrow metallic wire," *Phys. Rev. B*, vol. 52, pp. 1162–1166, Jul 1995.

[108] B. Pannetier and H. Courtois, "Andreev reflection and proximity effect," *Journal of Low Temperature Physics*, vol. 118, pp. 599–615, Mar 2000.

[109] J. Warlaumont, J. C. Brown, and R. A. Buhrman, "Response times and low-voltage behavior of SNS microbridges," *Applied Physics Letters*, vol. 34, no. 6, pp. 415–418, 1979.

[110] R. B. van Dover, A. de Lozanne, and M. R. Beasley, "Superconductor-normal-superconductor microbridges: Fabrication, electrical behavior, and modeling," *Journal of Applied Physics*, vol. 52, no. 12, pp. 7327–7343, 1981.

[111] A. Volkov, R. Seviour, and V. Pavlovskii, "Proximity-induced transport in hybrid mesoscopic normal–superconducting metal structures," *Superlattices and Microstructures*, vol. 25, no. 5, pp. 647 – 657, 1999.

[112] W. Belzig, F. K. Wilhelm, C. Bruder, G. Schön, and A. D. Zaikin, "Quasiclassical green's function approach to mesoscopic superconductivity," *Superlattices and Microstructures*, vol. 25, no. 5, pp. 1251 – 1288, 1999.

[113] D. A. Ivanov, R. von Roten, and G. Blatter, "Minigap in a long disordered SNS junction: Analytical results," *Phys. Rev. B*, vol. 66, p. 052507, Aug 2002.

[114] F. Zhou, P. Charlat, B. Spivak, and B. Pannetier, "Density of states in superconductor-normal metal-superconductor junctions," *Journal of Low Temperature Physics*, vol. 110, pp. 841–850, Feb 1998.

[115] M. Vinet, C. Chapelier, and F. Lefloch, "Spatially resolved spectroscopy on superconducting proximity nanostructures," *Phys. Rev. B*, vol. 63, p. 165420, Apr 2001.

[116] N. Moussy, H. Courtois, and B. Pannetier, "Local spectroscopy of a proximity superconductor at very low temperature," *EPL (Europhysics Letters)*, vol. 55, no. 6, p. 861, 2001.

[117] H. le Sueur, P. Joyez, H. Pothier, C. Urbina, and D. Esteve, "Phase controlled superconducting proximity effect probed by tunneling spectroscopy," *Phys. Rev. Lett.*, vol. 100, p. 197002, May 2008.

[118] S. Guéron, H. Pothier, N. O. Birge, D. Esteve, and M. H. Devoret, "Superconducting proximity effect probed on a mesoscopic length scale," *Phys. Rev. Lett.*, vol. 77, pp. 3025–3028, Sep 1996.

[119] B. D. Josephson, "Supercurrents through barriers," *Advances in Physics*, vol. 14, no. 56, pp. 419–451, 1965.

[120] T. T. Heikkilä, J. Särkkä, and F. K. Wilhelm, "Supercurrent-carrying density of states in diffusive mesoscopic Josephson weak links," *Phys. Rev. B*, vol. 66, p. 184513, Nov 2002.

[121] J. C. Hammer, J. C. Cuevas, F. S. Bergeret, and W. Belzig, "Density of states and supercurrent in diffusive SNS junctions: Roles of nonideal interfaces and spin-flip scattering," *Phys. Rev. B*, vol. 76, p. 064514, Aug 2007.

[122] H. Courtois, M. Meschke, J. T. Peltonen, and J. P. Pekola, "Origin of hysteresis in a proximity Josephson junction," *Phys. Rev. Lett.*, vol. 101, p. 067002, Aug 2008.

[123] G. E. Blonder, M. Tinkham, and T. M. Klapwijk, "Transition from metallic to tunneling regimes in superconducting microconstrictions: Excess current, charge imbalance, and supercurrent conversion," *Phys. Rev. B*, vol. 25, pp. 4515–4532, Apr 1982.

[124] P. G. DE GENNES, "Boundary effects in superconductors," *Rev. Mod. Phys.*, vol. 36, pp. 225–237, Jan 1964.

[125] P. G. de Gennes and D. Saint-James, "Elementary excitations in the vicinity of a normal metal-superconducting metal contact," *Physics Letters*, vol. 4, pp. 151–152, Mar. 1963.

[126] A. F. Andreev *Sov. Phys. JETP 19, 1228*, vol. 19, p. 1228, 1964.

[127] P. Dubos, H. Courtois, O. Buisson, and B. Pannetier, "Coherent low-energy charge transport in a diffusive s-n-s junction," *Phys. Rev. Lett.*, vol. 87, p. 206801, Oct 2001.

[128] K. Likharev, "Dynamics of Josephson junctions and circuits (gordon and breach, philadelphia, 1986)," *Google Scholar*.

[129] F. K. Wilhelm, A. D. Zaikin, and G. Schön, "Supercurrent in a mesoscopic proximity wire," *Journal of Low Temperature Physics*, vol. 106, pp. 305–310, Feb 1997.

[130] T. A. Fulton and L. N. Dunkleberger, "Origin of hysteresis in the i-v curves of point-contact junctions," *Journal of Applied Physics*, vol. 45, no. 5, pp. 2283–2285, 1974.

[131] W. J. Skocpol, M. R. Beasley, and M. Tinkham, "Self-heating hotspots in superconducting thin-film microbridges," *Journal of Applied Physics*, vol. 45, no. 9, pp. 4054–4066, 1974.

[132] M. Tinkham, J. U. Free, C. N. Lau, and N. Markovic, "Hysteretic $I - V$ curves of superconducting nanowires," *Phys. Rev. B*, vol. 68, p. 134515, Oct 2003.

[133] Y. Song, "Origin of "capacitance" in superconducting microbridges," *Journal of Applied Physics*, vol. 47, no. 6, pp. 2651–2655, 1976.

[134] L. Angers, F. Chiodi, G. Montambaux, M. Ferrier, S. Guéron, H. Bouchiat, and J. C. Cuevas, "Proximity dc squids in the long-junction limit," *Phys. Rev. B*, vol. 77, p. 165408, Apr 2008.

[135] W. Stewart, "Current-voltage characteristics of josephson junctions," *Applied Physics Letters*, vol. 12, no. 8, pp. 277–280, 1968.

[136] D. McCumber, "Effect of ac impedance on dc voltage-current characteristics of superconductor weak-link junctions," *Journal of Applied Physics*, vol. 39, no. 7, pp. 3113–3118, 1968.

[137] J. J. A. Baselmans, A. F. Morpurgo, B. J. van Wees, and T. M. Klapwijk, "Reversing the direction of the supercurrent in a controllable Josephson junction," *Nature*, vol. 397, pp. 43 EP –, Jan 1999.

[138] F. K. Wilhelm, G. Schön, and A. D. Zaikin, "Mesoscopic superconducting–normal metal–superconducting transistor," *Phys. Rev. Lett.*, vol. 81, pp. 1682–1685, Aug 1998.

[139] J. Kutchinsky, R. Taboryski, C. B. Sørensen, J. B. Hansen, and P. E. Lindelof, "Observation of supercurrent enhancement in SNS junctions by nonequilibrium injection into supercurrent carrying bound andreev states," *Phys. Rev. Lett.*, vol. 83, pp. 4856–4859, Dec 1999.

[140] H. J. Fink, "Supercurrents through superconducting-normal-superconducting proximity layers. i. analytic solution," *Phys. Rev. B*, vol. 14, pp. 1028–1038, Aug 1976.

[141] K. D. Usadel, "Generalized diffusion equation for superconducting alloys," *Phys. Rev. Lett.*, vol. 25, pp. 507–509, Aug 1970.

[142] K. Likharev, "The relation js (ϕ) for SNS bridges of variable thickness," *Sov. Tech. Phys. Lett*, vol. 2, pp. 12–4, 1976.

[143] M. Meschke, "Nanosized electronic cooler combined with superconducting proximity effect thermometry," *Journal of Low Temperature Physics*, vol. 175, no. 5-6, pp. 838–849, 2014.

[144] M. Zgirski, M. Foltyn, A. Savin, M. Meschke, and J. Pekola, "Nanosecond thermometry with Josephson junction," *arXiv preprint arXiv:1704.04762*, 2017.

[145] L. B. Wang, O.-P. Saira, and J. P. Pekola, "Fast thermometry with a proximity Josephson junction," *Applied Physics Letters*, vol. 112, no. 1, p. 013105, 2018.

[146] J. V. Koski, J. T. Peltonen, M. Meschke, and J. P. Pekola, "Laterally proximized aluminum tunnel junctions," *Applied Physics Letters*, vol. 98, no. 20, p. 203501, 2011.

[147] K. L. Viisanen and J. P. Pekola, "Anomalous electronic heat capacity of copper nanowires at sub-kelvin temperatures," *Phys. Rev. B*, vol. 97, p. 115422, Mar 2018.

[148] M. Meschke, W. Guichard, and J. P. Pekola, "Single-mode heat conduction by photons," *Nature*, vol. 444, p. 187, 11 2006.

[149] H. Courtois, H. Q. Nguyen, C. B. Winkelmann, and J. P. Pekola, "High-performance electronic cooling with superconducting tunnel junctions," *Comptes Rendus Physique*, vol. 17, no. 10, pp. 1139 – 1145, 2016.

[150] H. Q. Nguyen, M. Meschke, H. Courtois, and J. P. Pekola, "Sub-50-mk electronic cooling with large-area superconducting tunnel junctions," *Phys. Rev. Applied*, vol. 2, p. 054001, Nov 2014.

[151] H. Q. Nguyen, T. Aref, V. J. Kauppila, M. Meschke, C. B. Winkelmann, H. Courtois, and J. P. Pekola, "Trapping hot quasi-particles in a high-power superconducting electronic cooler," *New Journal of Physics*, vol. 15, no. 8, p. 085013, 2013.

[152] S. Rajauria, L. M. A. Pascal, P. Gandit, F. W. J. Hekking, B. Pannetier, and H. Courtois, "Efficiency of quasiparticle evacuation in superconducting devices," *Phys. Rev. B*, vol. 85, p. 020505, Jan 2012.

[153] S. Rajauria, H. Courtois, and B. Pannetier, "Quasiparticle-diffusion-based heating in superconductor tunneling microcoolers," *Phys. Rev. B*, vol. 80, p. 214521, Dec 2009.

[154] J. T. Peltonen, P. Virtanen, M. Meschke, J. V. Koski, T. T. Heikkilä, and J. P. Pekola, "Thermal conductance by the inverse proximity effect in a superconductor," *Phys. Rev. Lett.*, vol. 105, p. 097004, Aug 2010.

[155] D. M. T. van Zanten, F. Balestro, H. Courtois, and C. B. Winkelmann, "Probing hybridization of a single energy level coupled to superconducting leads," *Phys. Rev. B*, vol. 92, p. 184501, Nov 2015.

[156] X. Zianni, "Thermoelectric efficiency of a quantum dot in the single-electron transistor configuration," *Journal of Electronic Materials*, vol. 39, pp. 1996–2001, Sep 2010.

[157] H. L. Edwards, Q. Niu, and A. L. de Lozanne, "A quantum-dot refrigerator," *Applied Physics Letters*, vol. 63, no. 13, pp. 1815–1817, 1993.

[158] J. R. Prance, C. G. Smith, J. P. Griffiths, S. J. Chorley, D. Anderson, G. A. C. Jones, I. Farrer, and D. A. Ritchie, "Electronic refrigeration of a two-dimensional electron gas," *Phys. Rev. Lett.*, vol. 102, p. 146602, Apr 2009.

[159] M. Grobis, I. G. Rau, R. M. Potok, and D. Goldhaber-Gordon, *The Kondo Effect in Mesoscopic Quantum Dots*. American Cancer Society, 2007.

[160] B. Dutta, D. Majidi, A. García Corral, P. A. Erdman, S. Florens, T. A. Costi, H. Courtois, and C. B. Winkelmann, "Direct probe of the seebeck coefficient in a kondo-correlated single-quantum-dot transistor," *Nano Letters*, vol. 19, no. 1, pp. 506–511, 2019.

[161] R. Scheibner, H. Buhmann, D. Reuter, M. N. Kiselev, and L. W. Molenkamp, "Thermopower of a kondo spin-correlated quantum dot," *Phys. Rev. Lett.*, vol. 95, p. 176602, Oct 2005.